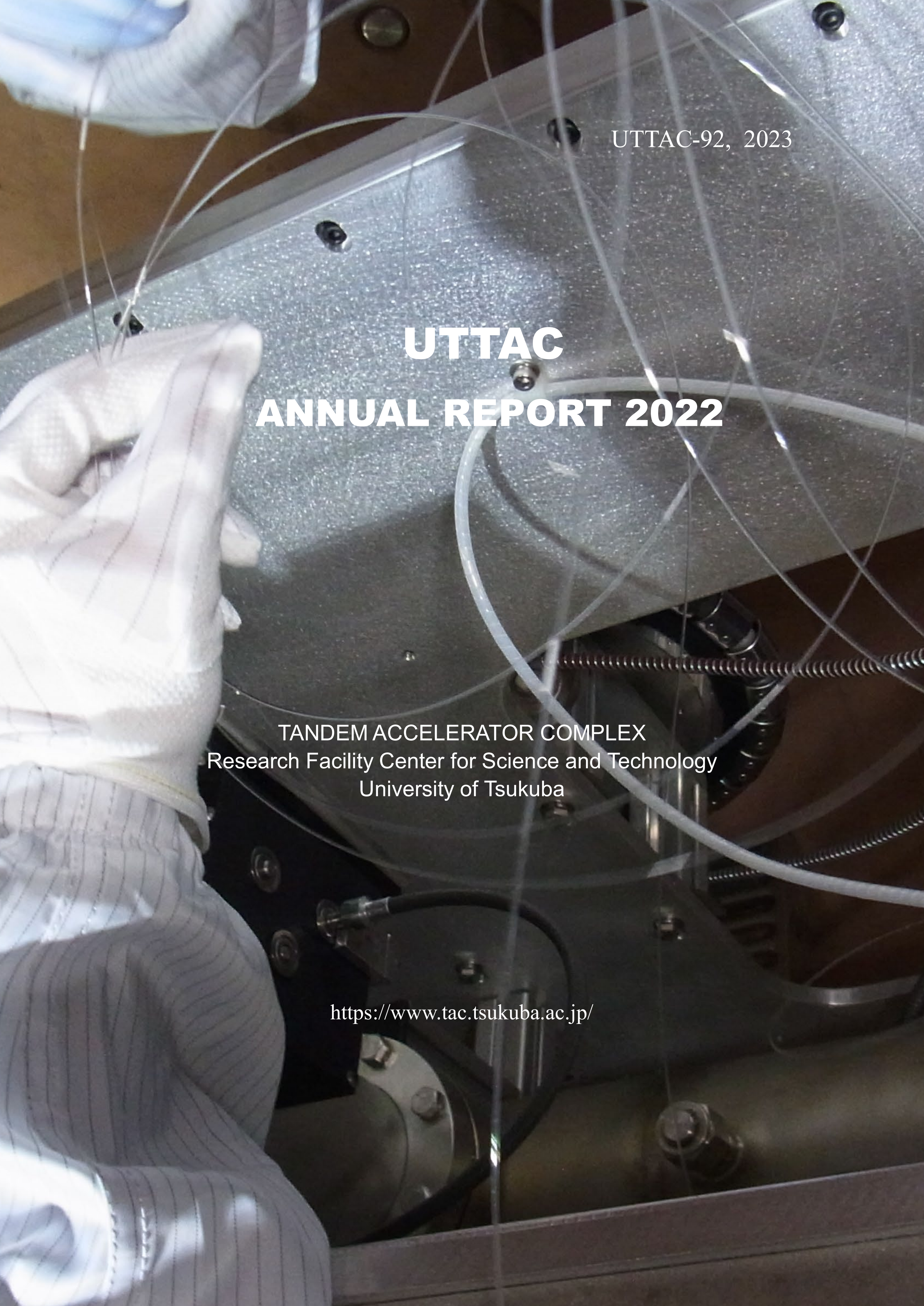

UTTAC-92, 2023

UTTAC
ANNUAL REPORT 2022

TANDEM ACCELERATOR COMPLEX
Research Facility Center for Science and Technology
University of Tsukuba

https://www.tac.tsukuba.ac.jp/

UTTAC

ANNUAL REPORT 2022

April 1, 2022 – March 31, 2023

UTTAC-92, 2023

Editors : Tetsuaki Moriguchi, Kimikazu Sasa, Yoshihiro Yamato, Masumi Matsumura, Masao Sataka, Hiroshi Naramoto, Eiji Kita, and Hiroshi Kudo (editor-in-chief)

UTTAC ANNUAL REPORT is a series of issues, which describes annual research activities at Tandem Accelerator Complex, Research Facility Center for Science and Technology, University of Tsukuba.

Tandem Accelerator Complex, Research Facility Center for Science and Technology,
University of Tsukuba
Tennodai 1-1-1, Tsukuba, Ibaraki 305-8577, Japan
annual@tac.tsukuba.ac.jp

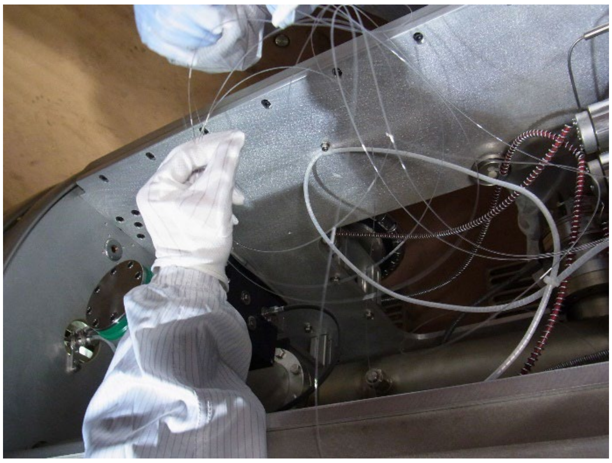

Cover: Wearing antistatic gloves, engineers of UTTAC are laying plastic optical fibers for enabling ethernet to be used on the high-voltage terminal of the 6MV tandem accelerator.

PREFACE

This annual report covers research and development (R&D) carried out at University of Tsukuba Tandem Accelerator Complex (UTTAC) during the fiscal year 2022 (1 April 2022 ~ 31 March 2023). The topics include not only accelerator-based R&D using the 6MV tandem and 1MV Tandetron accelerators, but also radioisotope-based R&D employing positron annihilation spectroscopy and Mössbauer spectroscopy. The good news in FY2022 is that high school visitors are back as the nasty coronavirus has subsided.

September 1, 2023
Editorial board

High school students are listening to an explanation of the tandem accelerator from the engineer on the left. They are looking inside the accelerator tank using the virtual reality system, putting on VR goggles.

CONTENTS

1.

ACCELERATOR OPERATION AND RELATED STUDIES

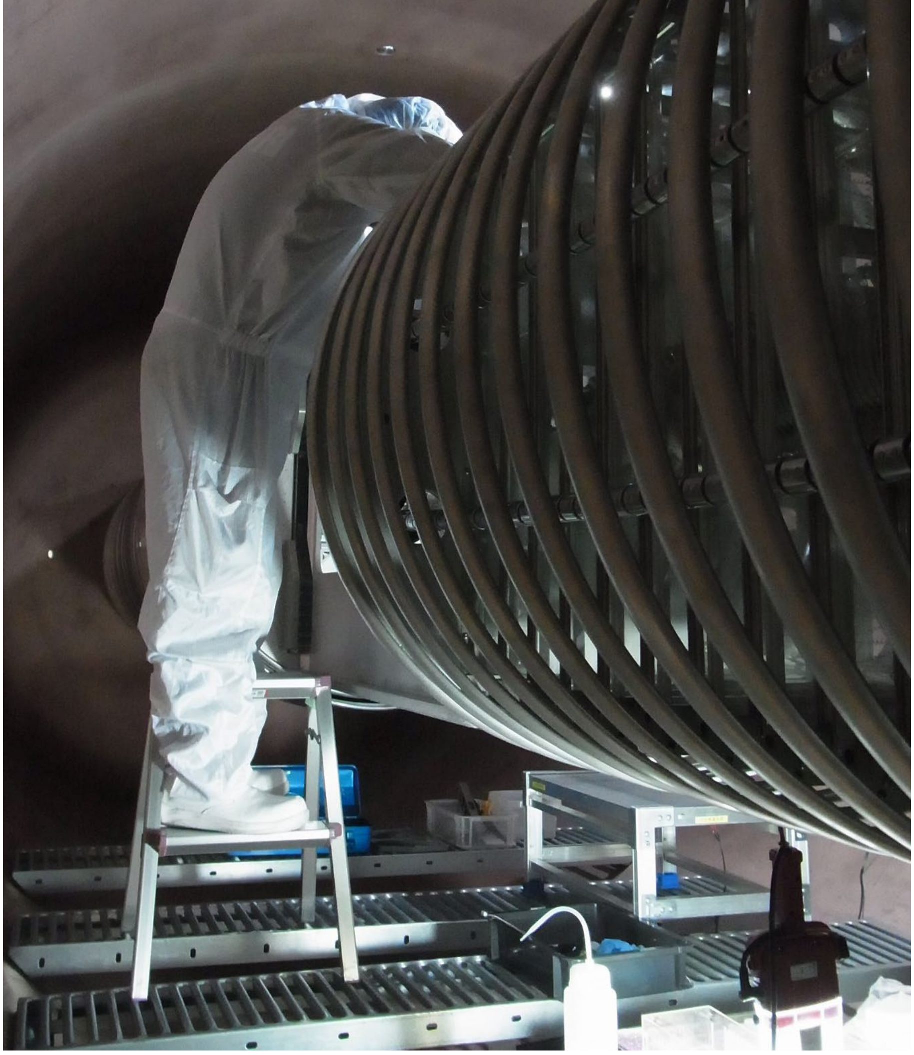

An engineer of UTTAC working for maintenance and upgrading of the 6MV tandem accelerator.

1.1 Accelerator operation 2022

K. Sasa, S. Ishii, T. Takahashi, Y. Yamato, T. Yoshida, M. Matsumura, T. Moriguchi

University of Tsukuba Tandem Accelerator Complex (UTTAC) is promoting the maintenance and operation of the tandem accelerator facility consisting of the 6MV Pelletron tandem accelerator and the 1MV Tandetron accelerator for cooperative researches both inside and outside the University of Tsukuba.

1MV Tandetron accelerator

The 1MV Tandetron accelerator with 2 negative ion sources and 4 beamlines was operated for a total of 42 days in FY2022. The operating time and the experimental beam time were 575.5 and 157.6 hours, respectively, during the total service time in FY2022. A total of 37 experiments with 137 participants were carried out using this accelerator. Figures 1 and 2 show classification of the accelerated ions and of experimental purposes, respectively. Note that for each pair of the monoatomic and diatomic beams their total acceleration time is shown in Fig. 1 since the time for the two cases was hardly distinguished. Instability of the terminal voltage has been sometimes observed for this accelerator since 2022, probably due to age-related deterioration of the voltage circuit.

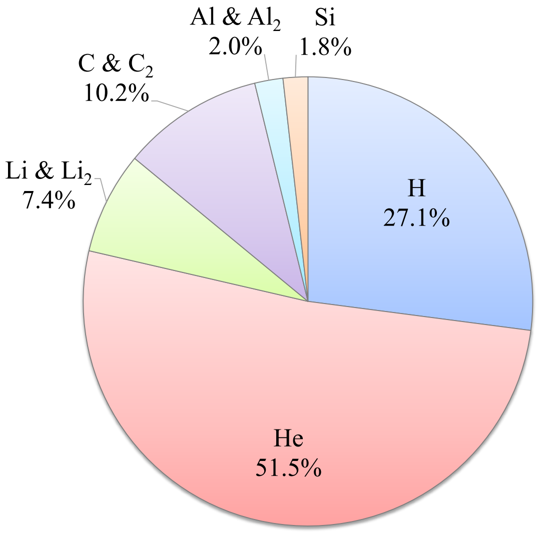

Fig. 1. Accelerated ions by the 1MV Tandetron accelerator in FY2022.

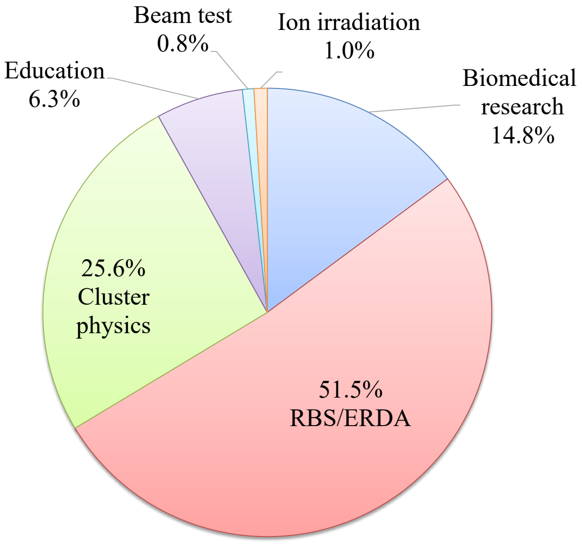

Fig. 2. Experimental purposes of the 1MV Tandetron accelerator in FY2022.

6MV Pelletron tandem accelerator

The 6MV Pelletron tandem accelerator with 5 negative ion sources and 12 beamlines was operated for a total of 103 days. Its operating time and the experimental beam time were 1,154.4 and 1,010 hours, respectively, during the total service time in FY2022. The operating time decreased by about 20% compared to the last fiscal year [1]. In FY2022, this accelerator was used for 11 research projects on campus and 7 research projects cooperating with facilities outside the campus. A total of 53 experiments with 307 participants were carried out using this accelerator. In May 2022, the terminal generator broke down, hence the acceleration tank was opened for repairs, resulting in a period of approximately one month of inactivity of this accelerator. During the scheduled maintenance in March 2023, a new vacuum gauge was installed at the terminal [2].

Figure 3 shows the beam time histogram with respect to the terminal voltage. Figures 4 and 5 show classification of the accelerated ions and of the experimental purposes, respectively. The most frequently used case was AMS for iodine-129 at the terminal voltage of 5 MV. In addition, nuclear experiments using polarized deuterons from polarized ion sources were started in FY2022.

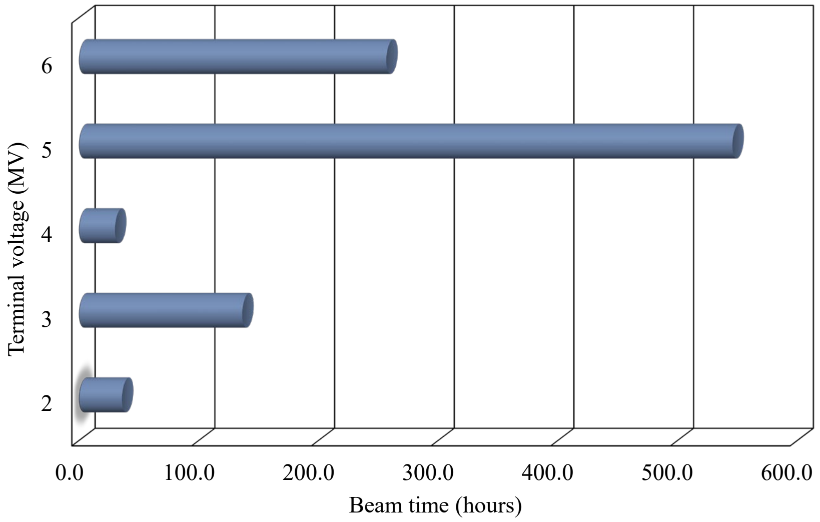

Fig. 3. Beam time histogram as a function of the terminal voltage for the 6MV Pelletron tandem accelerator in FY2022.

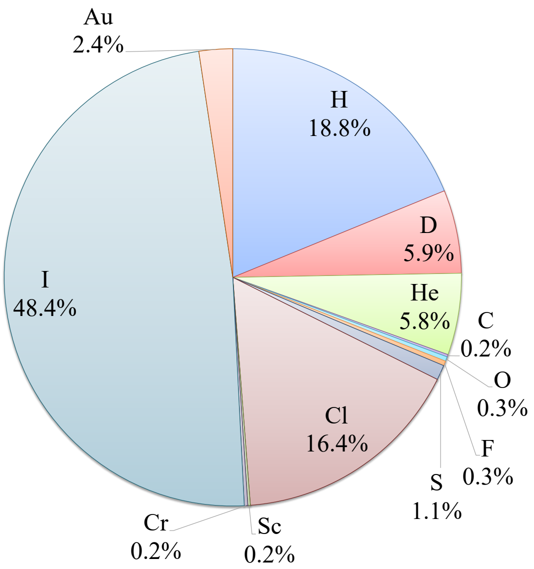

Fig. 4. Accelerated ions for the 6MV Pelletron tandem accelerator in FY2022.

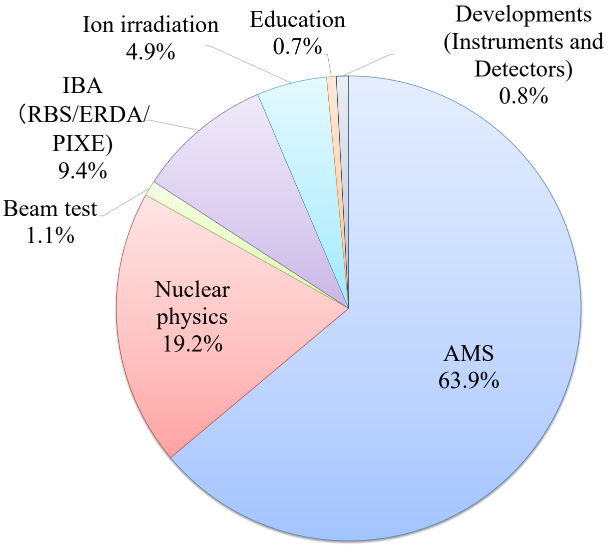

Fig. 5. Experimental purposes of the 6MV Pelletron tandem accelerator in FY2022.

References

[1] K. Sasa et al., UTTAC Annual Report 2021, UTTAC-91 (2022) 1.

[2] Y. Yamato et al., this Annual Report 6.1.

1.2 Approach to possible maximum energies of low Z ions accelerated by the 6MV tandem accelerator

M. Sataka, T. Takahashi, H. Naramoto, H. Kudo, K. Sasa

Acceleration tests of ion beams obtained from the 6MV tandem accelerator at UTTAC have been continued [1]. In this fiscal year, high-energy heavy ion beams were required for ion irradiation experiments for material science such as ion beam modification of materials [2]. At UTTAC, very weak beams of high-energy low-Z ions are indispensable for radiation resistance tests of semiconductors used in space [3].

Chromium data were newly collected, while S, Cl and Sc data were updated. We have measured beam currents of the accelerated ions as a function of the ion charge at an acceleration voltage from 3 to 6 MV. Figure 1 shows the beam current distributions of Cr ion as a function of the ion charge at the maximum terminal voltage of 6 MV. A carbon foil of ~5 μg/cm^2 thickness was used as a stripper at the 6 MV terminal.

In this accelerator control system, the minimum measurable value of the Faraday cup current is 0.1 nA, while measurement of lower current is needed for low Z ions. For this purpose, the bending magnets, lenses and steerers were preset to the estimated values, thereby leading the ion beam to the end Faraday cup with a picoammeter at the experimental apparatus. Beam operation time was not significantly different from that for high-current ions. For measurement of extremely low current, a particle detector was used instead of a picoammeter.

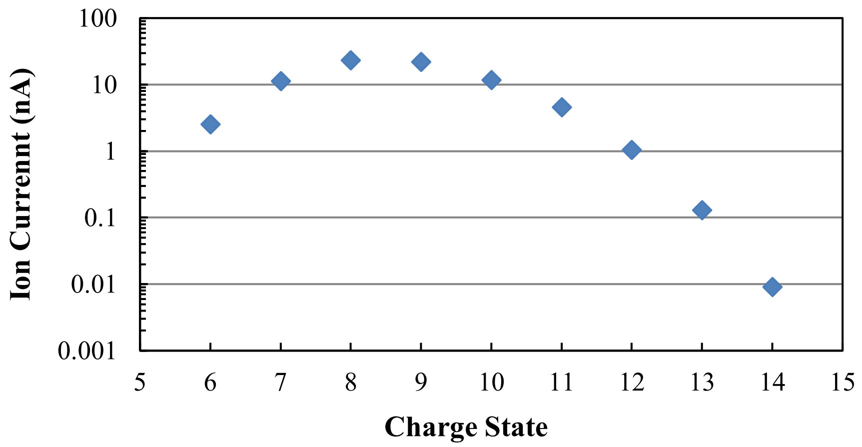

Fig. 1. Beam current distribution of Cr ion at the terminal voltage of 6 MV. A foil stripper was used at the high voltage terminal.

Table 1 shows the beam current distribution of ions which were produced from molecular ions. In this case, the accelerated ion energy cannot be determined only by the terminal voltage and the ion charge after acceleration. Table 2 shows the ion charges and maximum energies obtained for injection of negative atomic ions at the terminal voltage of 6 MV. Tables 1 and 2 show the data accumulated from 2016 to 2022.

Table 1. Beam current distributions for molecular ion injection at the terminal voltage of 6 MV, which have been accumulated since 2016. The measured beam intensity is shown by the symbols: ○: ≥ 1 nA, △: ≤1 nA. Shown in red were obtained by using foil strippers.

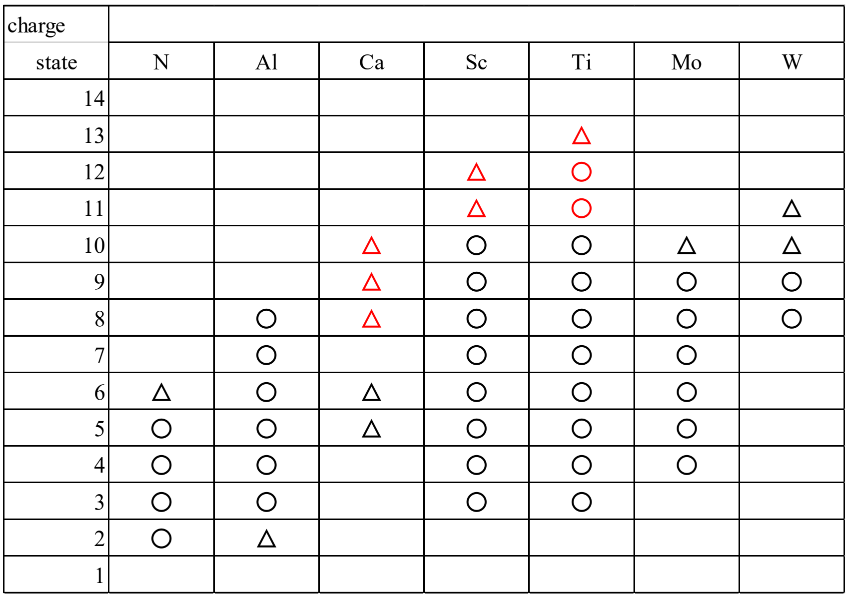

charge state	N	Al	Ca	Sc	Ti	Mo	W
14							
13					△		
12				△	○		
11				△	○		△
10			△	○	○	△	△
9			△	○	○	○	○
8		○	△	○	○	○	○
7		○		○	○	○	
6	△	○	△	○	○	○	
5	○	○	△	○	○	○	
4	○	○		○	○	○	
3	○	○		○	○		
2	○	△					
1							

Table 2. Summary of the acceleration tests from 2016 to 2021 for negative atomic ion injection at the terminal voltage of 6 MV. The measured beam intensities are shown by the symbols: ○: ≥1 nA, △: ≤1 nA. Shown in red were obtained by using foil strippers.

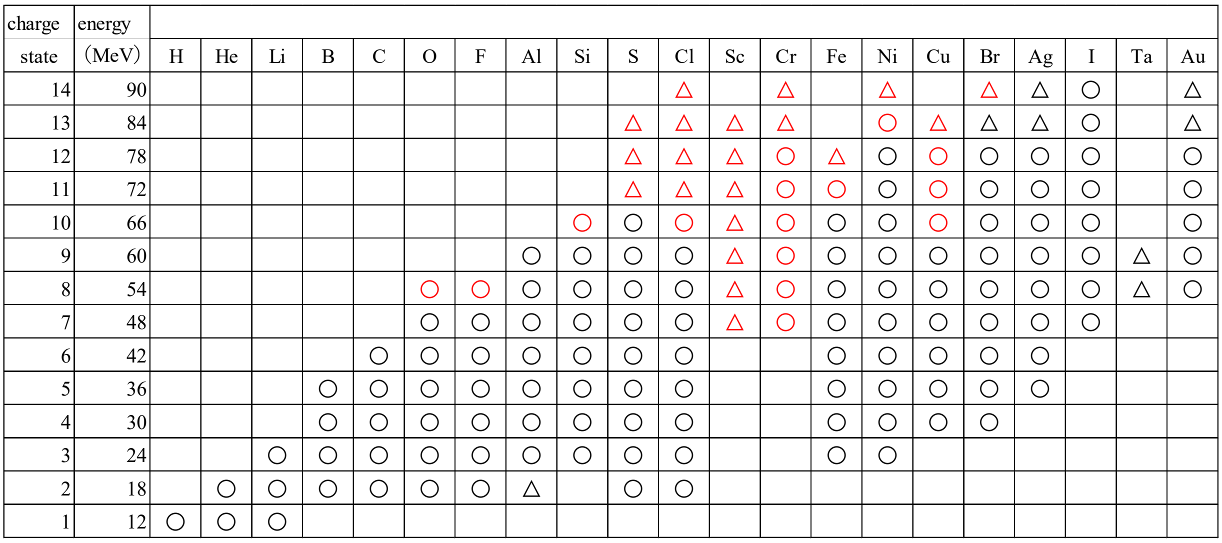

charge state	energy (MeV)	H	He	Li	B	C	O	F	Al	Si	S	Cl	Sc	Cr	Fe	Ni	Cu	Br	Ag	I	Ta	Au
14	90											△		△		△		△	△	○		△
13	84										△	△	△	△		○	△	△	△	○		△
12	78										△	△	△	○	△	○	○	○	○	○		○
11	72										△	△	△	○	○	○	○	○	○	○		○
10	66									○	○	○	△	○	○	○	○	○	○	○		○
9	60								○	○	○	○	△	○	○	○	○	○	○	○	△	○
8	54						○	○	○	○	○	○	△	○	○	○	○	○	○	○	△	○
7	48						○	○	○	○	○	○	△	○	○	○	○	○	○	○		
6	42					○	○	○	○	○	○	○			○	○	○	○	○			
5	36				○	○	○	○	○	○	○	○			○	○	○	○	○			
4	30				○	○	○	○	○	○	○	○			○	○	○	○				
3	24			○	○	○	○	○	○	○	○	○			○	○						
2	18		○	○	○	○	○	○	△		○	○										
1	12	○	○	○																		

References

[1] M. Sataka et al., UTTAC Annual Report 2021, UTTAC-91 (2022) 3 and references therein.

[2] H. Matsui et al., this Annual Report 5.3.

[3] H. Kukita et al., this Annual Report 5.2.

1.3 Production of a faint beam at the experimental room

T. Moriguchi, M. Sataka, S. Ishii, T. Takahashi, T. Yoshida, A. Yano

For research and development of detectors with ion beam irradiation, adjustment of the beam intensity is necessary to evaluate the correct performances of the detectors without radiation-induced deteriorations. So far, in the detector tests using ion beams supplied by the 6MV Pelletron tandem accelerator, the beam intensity was attenuated using elastic scattering of ions when they pass through a thin foil of gold, for example [1-4]. In this method, the beam suffers degraded beam emittance and energy struggling, hence other method to obtain a faint beam is required for detector tests. In FY2022, we attempted to produce a faint beam at the experimental room often used for nuclear experiments and detector tests.

We started by transporting 12-MeV protons of maximum intensity to the A7 course in the experimental room. At this time, the typical beam current at the Faraday-cup of the A7 course ($I_{\mathrm{A7\text{-}FC}}$) was 58 nA. Inserting an attenuator upstream of the accelerator ($\mathrm{Att_{up}}$), $I_{\mathrm{A7\text{-}FC}}$ was reduced to ~1 nA. After closing the low-energy beam slits (LE-slit) to the lower limit, indicating the 1.0-mm squared aperture, $I_{\mathrm{A7\text{-}FC}}$ was reduced to ~4 pA. To defocus the beam, we stopped the current of the quadrupole magnet in the A7 course ($\mathrm{QM_{A7}}$), which is the most downstream quadrupole magnet in the beam line. After defocusing, the beam count rates at the A7 course ($I_{\mathrm{A7\text{-}PL}}$) was ~60 kcps, which was measured by a plastic scintillation counter (PL) located at the end of the A7 course in the air. Note that such a beam current is too low to measure with a Faraday cup. Moreover, we used one of the additional attenuators ($\mathrm{Att_{down}}$), which consist of a total of 16 meshed foils installed in the foil changer unit just downstream of the accelerator. Using the $\mathrm{Att_{down}}$ of #16 as the typical case, we obtained $I_{\mathrm{A7\text{-}PL}}$~700 cps, indicating successful production of the faint beam. Table 1 is a list of the beam intensities at each process for the production of the faint beam. For the fine adjustment of $I_{\mathrm{A7\text{-}PL}}$, it is effective to tune the currents of the quadrupole magnets, with a selection of suitable $\mathrm{Att_{down}}$.

Table 1. Typical beam intensities of 12-MeV protons at each process for the production of the faint beam. $I_{\mathrm{A7\text{-}FC}}$ and $I_{\mathrm{A7\text{-}PL}}$ indicate the beam current obtained from the Faraday cup and the beam count rates obtained from the plastic scintillation counter, respectively, in the A7 course.

	Attenuation rate	$I_{\mathrm{A7\text{-}FC}}$	$I_{\mathrm{A7\text{-}PL}}$
Maximum beam intensity		58 nA	3.6×10^{11} cps*1
w/ $\mathrm{Att_{up}}$	~ 1/50	1 nA	6.3×10^{9} cps*1
w/ LE_Slit close	~ 1/250	4 pA	2.5×10^{7} cps*1
w/ $\mathrm{QM_{A7}}$ off	~ 1/400	–	60 kcps
w/ $\mathrm{Att_{down}}$	~ 1/100*2	–	700 cps

*1: Converted from the $I_{\mathrm{A7\text{-}FC}}$. *2: Depending on the selected attenuator.

Figure 1 shows the energy spectrum of protons measured by a round shaped silicon detector (ORTEC, BA-24-150-1000), whose active area and sensitive depth are 150 mm^2 and 1000 μm, respectively. The silicon detector was installed in the scattering chamber of the A7 course, and irradiated directly with 12-MeV protons ($I_{\mathrm{A7\text{-}PL}}$ ~700 cps). As shown in Fig. 1, the energy peak of protons (FWHM ~20 ch) is clearly seen without remarkable pileup, while there are low-energy events resulting from the beam irradiation. We will use the faint beams for the detector tests in the future.

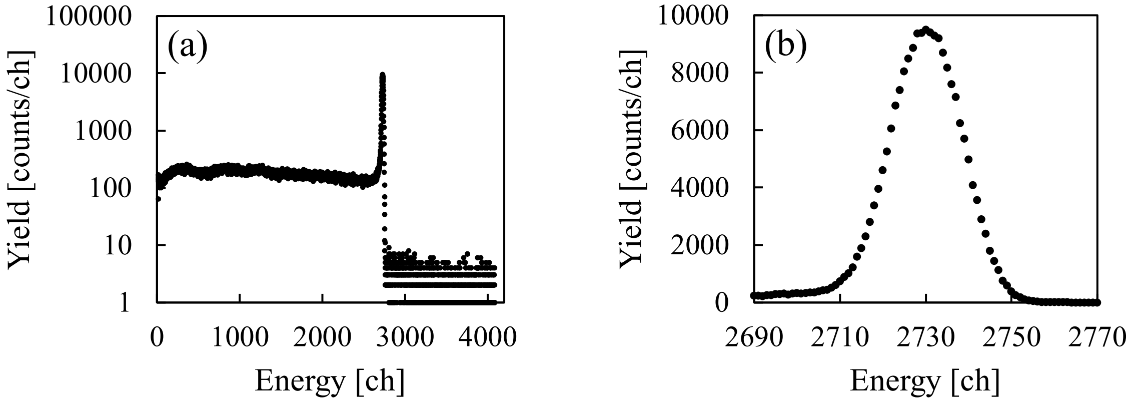

Fig. 1. (a) Typical energy spectrum for the faint beam of 12-MeV protons. (b) Enlarged peak area of the same spectrum shown in the linear scale.

References

[1] T. Yamaguchi et al., UTTAC Annual Report 2017, UTTAC-87 (2018) 9.

[2] T. Yamaguchi et al., UTTAC Annual Report 2018, UTTAC-88 (2019) 8.

[3] S. Y. Matsumoto et al., UTTAC Annual Report 2020, UTTAC-90 (2021) 12.

[4] T. Yamaguchi et al., UTTAC Annual Report 2021, UTTAC-91 (2022) 12.

1.4 Gamma-ray measurements inside the acceleration tank of the 6MV tandem electrostatic accelerator at the University of Tsukuba

H. Matsumura[1], M. Matsumura, G. Yoshida[1], T. Moriguchi, K. Sasa

The 6MV Pelletron tandem electrostatic accelerator (18SDH-2, National Electrostatics Corp.) has been installed at the University of Tsukuba Tandem Accelerator Complex (UTTAC) and has been in operation since 2016 [1]. This accelerator is used for various researches, in particular, the largest percentage of the accelerator operating time is occupied by AMS [2]. The accelerator system consists of ion sources, an accelerator tank, beamline components, which are surrounded by the concrete wall of the accelerator room. Determining which parts of the accelerator are activated will be helpful for future decommissioning of the accelerator. Because of the particularly large volumes of the acceleration tank and accelerator room concrete, decontamination will be very hard and expensive if these parts become radioactive. Therefore, there is great interest in whether they will be activated or not, hence we investigated previously the activation of the accelerator facility at UTTAC [3–5].

Among the particle beams accelerated by the tandem accelerator at UTTAC, the proton beam accelerated up to 12 MeV is most serious for activation. Strong activation is induced by nuclear reactions with primary protons at the beam loss point. In addition, the neutrons produced by the primary nuclear reactions activate the surrounding materials after thermalization. In our previous study, several strongly activated regions were observed on the beamline immediately after acceleration of the proton beam [3]. We also measured the fluence rate of thermal neutrons in the accelerator room and concluded that the accelerator room concrete is not activated even after 30 years of operation [4]. Similarly, the thermal neutron fluence rate on the surface of the acceleration tank during the operation was measured in a previous study [5]. The measured results inferred that the acceleration tank was not activated. In the present study, as further investigation, γ rays were measured inside the acceleration tank to confirm that there were no activation points.

On May 23, 2022, 26 days after the last accelerator operation (and, in particular, 45 days after the activatable 12-MeV proton beam operation), γ rays were measured in the acceleration tank using a NaI scintillation survey meter (manufacturer: Aloka, model: TCS-161, and detector crystal: 1-inch NaI(Tl) scintillator) and a $LaBr_3$ scintillation spectrometer (TechnoAP, TS-100, and 1-inch $LaBr_3$(Ce) scintillator). First, a radiation survey in the entire acceleration tank was performed using the NaI scintillation survey meter. Gamma radiation dose levels for all objects were at the background level, and no activation was observed anywhere. Next, γ-ray spectra were obtained using the $LaBr_3$ scintillation spectrometer for more precise evaluation at the three typical locations (Locations A, B, and C) shown in Fig. 1, where the beam loss was likely to occur. The measurement time was 5 minutes. Photos of Locations A, B, and C are shown in Fig. 2. A background spectrum was also obtained on the bottom of the acceleration tank at Location D, shown in Fig. 1, upstream of the beam line, where activation cannot occur due to the low beam energy. The measurement time at Location D was 5 minutes, same as for Locations A, B, and C. A photo of the

---

[1] High Energy Accelerator Research Organization (KEK)

background measurement at Location D is shown in Fig. 2.

Figure 3 shows comparison of the γ-ray spectra measured at Locations A, B, and C with the background γ-ray spectrum obtained at Location D. As shown in Fig. 4, all γ-ray spectra agree with the background spectrum. The peak counts for ^{54}Mn, ^{56}Co, ^{58}Co, and ^{60}Co, which are possible nuclides, were analyzed, and the results were within the errors. As expected from the results of the previous study, the absence of activation of the acceleration tank was confirmed in the present investigation. The results of this series of activation investigations performed at UTTAC will be helpful for the future decommissioning of this facility.

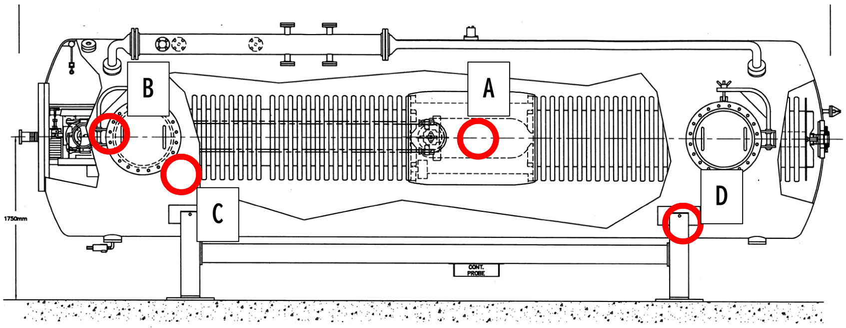

Fig. 1. Locations A, B, C, and D. A: near the stripper foil, B: upstream of the outlet duct, C: downstream frame, and D: upstream tank bottom.

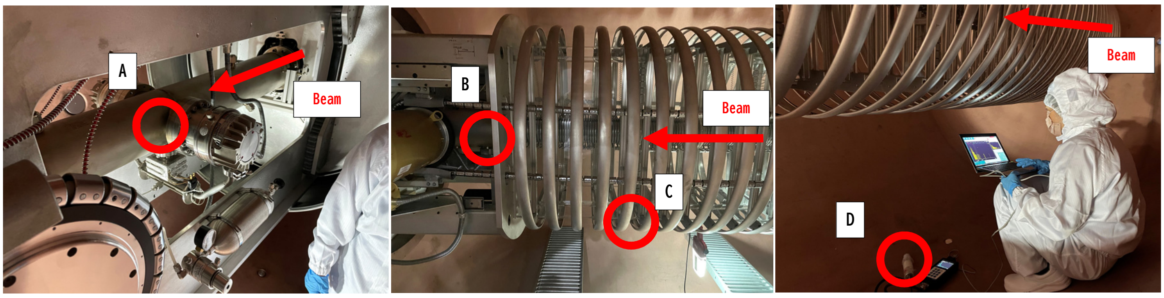

Fig. 2. Locations A, B, C, and D where γ-ray spectra were measured with the LaBr₃ scintillation spectrometer.

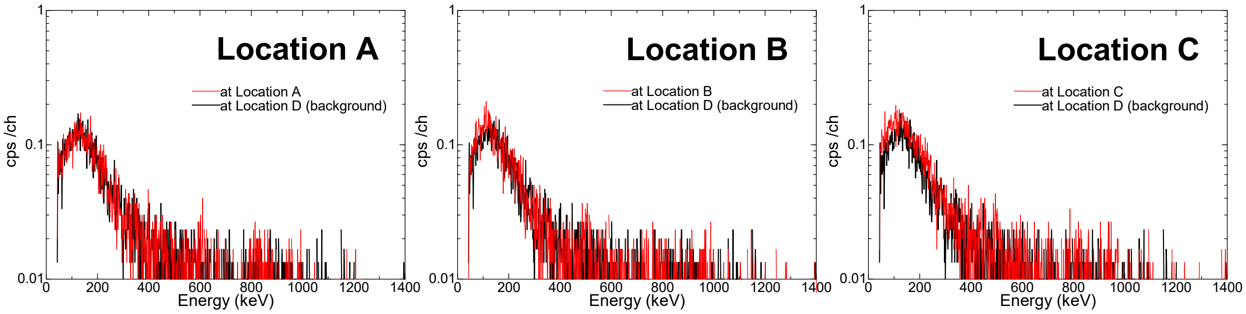

Fig. 3. Comparison of the γ-ray spectra measured at Locations A, B, and C (red) with the background (black).

References

[1] K. Sasa et al., UTTAC Annual Report 2016, UTTAC-86 (2017) 1.

[2] K. Sasa et al., UTTAC Annual Report 2021, UTTAC-91 (2022) 1.

[3] G. Yoshida et al., Radiation Safety Management 20 (2021) 1.

[4] H. Matsumura et al., Radiation Protection 40 (2020) 667.

[5] H. Nakamura et al., Environmental Radiochemical Analysis VI (2019) 152.

2.

NUCLEAR AND COLLISION-BASED RESEARCH

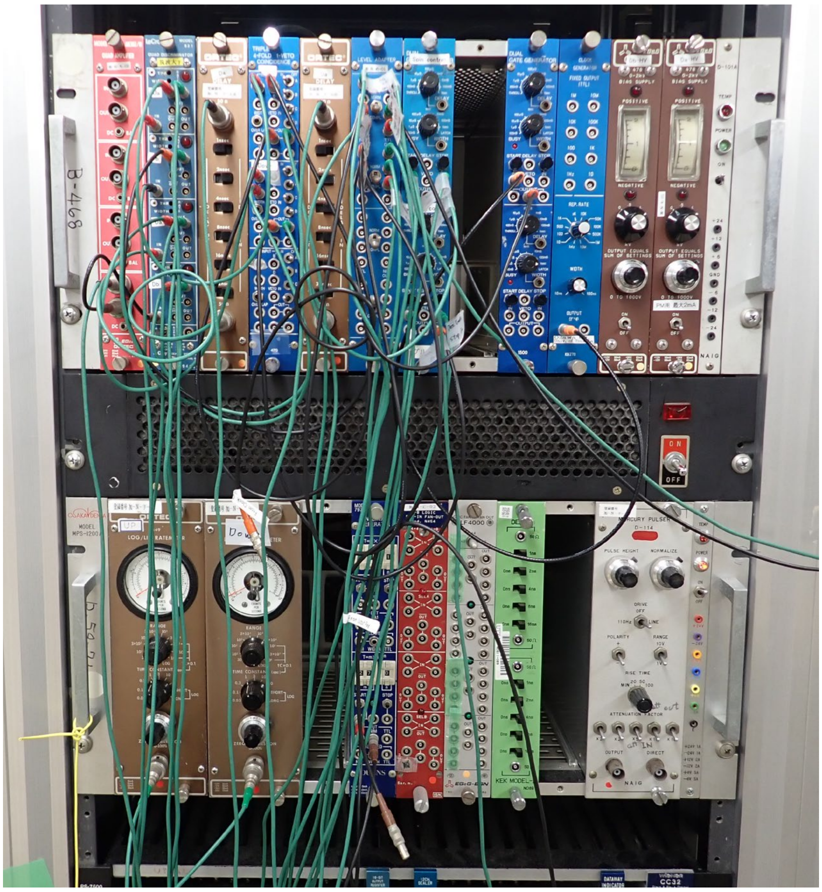

Measuring the nuclear magnetic moment of unstable nuclei.
——— *Report 2.1*

2.1 Search for magnetic moment of ^{30}P

A. Ozawa, T. Moriguchi, Y. Yamato, A. Yano, Y. Seki

Nuclear magnetic moment (μ) is very sensitive to nuclear structure. It gives detailed information about the single particle nature and its shell structure. Thus, it is important to measure μ also for unstable nuclei. Among the nuclei, odd-odd $N=Z$ nuclei are of special interest. In this case, by using the observed magnetic moment and β-decay life-time, it is possible to deduce the matrix element for spin operators for zero isospin ($T=0$). It is also interesting whether the odd-odd $N=Z$ nuclei may have the deuteron-like structure. Among the odd-odd $N=Z$ nuclei in the light mass region ($A<40$), μ of ^{30}P ($I^{\pi}=1^{+}$, $T_{1/2}=2.50$ min) is unknown. This nucleus is located in the middle of *sd* shell region. Thus, this nucleus may be deformed. In this case, single particle nature is not anticipated. Therefore, to investigate the nuclear structure of ^{30}P, it is important to measure μ for ^{30}P.

Until now, we succeeded in the production of ^{30}P by using two primary beams; one is by using polarized proton beams with Si target (^{30}Si(p,n)^{30}P reaction) and the other is by using polarized deuteron beams with Si target (^{29}Si(d,n)^{30}P reaction). Typical β-ray time spectrum for measurements using polarized proton beams (12 MeV) with Si (n-type, low-impedance) is shown in Fig. 1 (a). On the other hand, typical β-ray time spectrum for measurements using polarized deuteron beams (6 MeV) with Si (p-type, high-impedance) is shown in Fig. 1 (b). In both of the figures, a large amount of ^{30}P can be recognized. However, as the background, a large amount of ^{29}P ($I^{\pi}=1/2^{+}$, $T_{1/2}=4.14$ s) is also seen. Since μ of ^{29}P is known, we can check the polarization degree corresponding to the above conditions. Typically, the observed polarization of ^{29}P is roughly 1% for the polarized proton beams ($E_{\mathrm{p}}=12$ MeV) and roughly 5% for the polarized deuteron beams ($E_{\mathrm{d}}=6$ MeV) with the Si target. Since the atomic number of ^{29}P and ^{30}P is the same ($Z=15$) and the mass number is very close, it is expected that location of ^{30}P after the reaction is the same as that of ^{29}P in Si. Thus, it is expected that ^{30}P is also polarized with the polarized proton and deuteron beams. On the other hand, compared with ^{29}P, a large amount of polarization is not anticipated in ^{30}P since its life time is very long (2.50 ms) and the relaxation time of polarization in Si is only 22(2) s, that was determined for ^{29}P [1]. The spin of ^{30}P (1^{+}) may induce electric quadrupole interaction in the Si target, which may destroy the nuclear polarization of ^{30}P faster than that of ^{29}P.

The beam energy is a parameter of importance to produce the nuclear polarization. In the (p,n) reaction, the proton beam energy corresponds to the states in the produced nucleus. In some cases, very large energy dependence of polarization is observed [2]. Thus, it is important to change the beam energy. In FY2022, we searched μ of ^{30}P by using the polarized proton beams ($E_{\mathrm{p}}=7$, 7.5, 8, 8.5, 9 and 10 MeV) and the polarized deuteron beams ($E_{\mathrm{d}}=6$, 8, 10 and 12 MeV). We searched μ of ^{30}P from 0.2 to 0.9 n.m.. Within this range, μ of deuteron ($\mu=0.857$ n.m.), typical prediction by the shell model ($\mu=0.70\sim0.83$ n.m. [3]) and the prediction by three-body model calculations ($\mu=0.318$ n.m. [4]) are included. In measurements in FY2022, we could not observe significant effect for ^{30}P. We will continue the measurements by changing the energy of the primary beams.

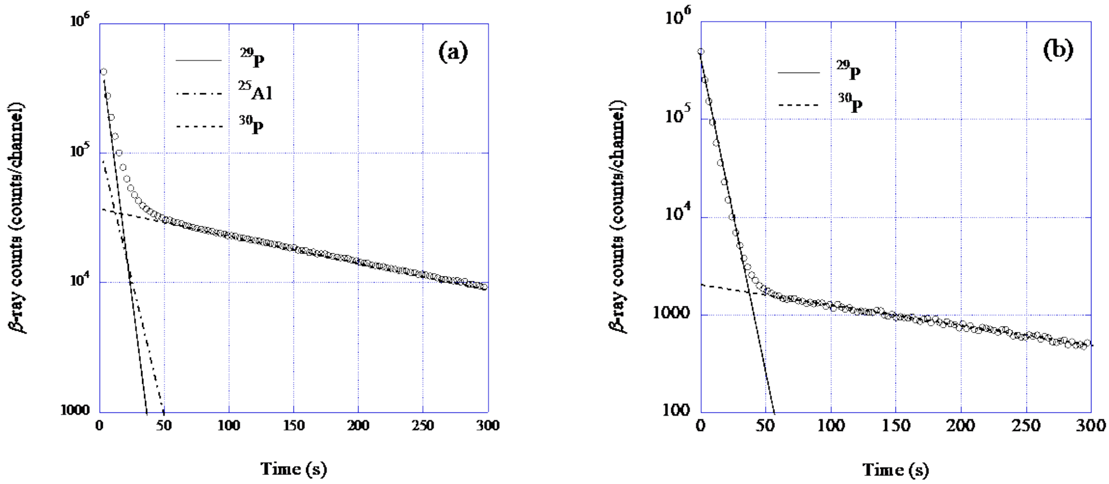

Fig. 1. (a) Typical time spectrum of β-rays for Si (n-type, low-impedance) irradiated by a polarized 12-MeV proton beam. The solid and broken lines correspond to the decay for ^{29}P and ^{30}P, respectively. The dashed line corresponds to the decay for ^{25}Al ($T_{1/2}$=7.18 s), that is produced by ^{28}Si(p,α)^{25}Al reaction. (b) Typical time spectrum of β-rays for Si (p-type, high-impedance) irradiated by a polarized 6-MeV deuteron beam. The solid and broken lines correspond to the decay for ^{29}P and ^{30}P, respectively.

References

[1] T. Minamisono et al., Phys. Rev. C 14 (1976) 376.
[2] T. Minamisono et al., Phys. Rev. C 14 (1976) 2335.
[3] P. W. M. Glaudemans et al., Annals of Phys. 63 (1971) 134.
[4] Y. Tanimura et al., Prog. Theor. Exp. Phys. (2014) 053D02.

2.2 Nuclear data of ^{32}S(α, p)^{35}Cl observed at 0° by the experimental setup for T-ERDA

H. Kudo, H. Naramoto, M. Sataka, S. Ishii, K. Sasa, S. Tomita

As a by-product of hydrogen analysis of PPS, polyphenylene sulfide $(C_6H_4S)_n$, by transmission ERDA [1], the ^{32}S(α, p)^{35}Cl reaction at 0° has been observed. The PPS sample of 1.35 μm thickness was underlaid with a Ni foil of 20 μm thickness to prevent the incident 8 MeV ^{4}He^{2+} from entering the particle detector. In the measured ERDA spectrum, shown in Fig. 1, we see three sharp peaks indicated by p_0, p_1, and p_2, the latter two of which are superimposed on the tail of the large peak of recoil hydrogen at 4.2 MeV. From the energy shift of the prominent p_0 peak measured for the Ni foil of 25 μm thickness, we found that the peak is due to protons emitted from the PPS film. Indeed, the protons result from the ^{32}S(α, p_0)^{35}Cl reaction with the Q value equal to -1.866 MeV [2], where the subscript of p_0 represents the p-emission with the nuclear transition to the ground level of ^{35}Cl.

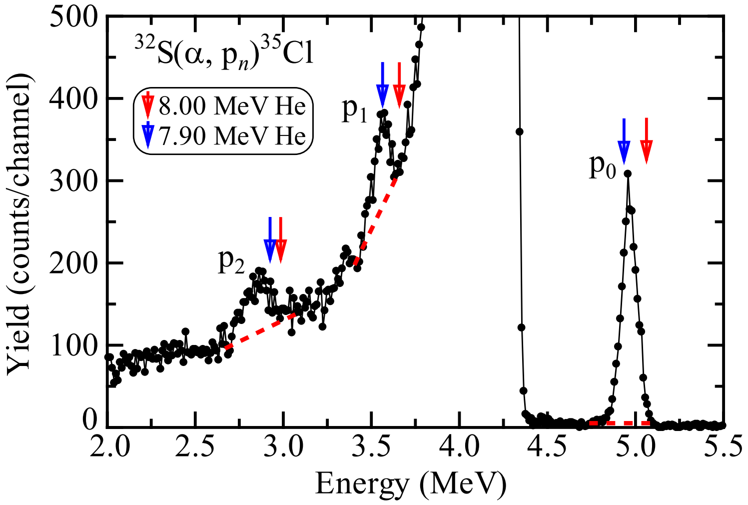

Fig. 1. Energy spectrum of protons escaped from PPS/Ni(20) in the 0° direction. The calculated peak energies due to the nuclear reaction at the PPS surface (8.00 MeV He) and backsurface (7.90 MeV He) are shown by the red and blue arrows, respectively. The red dashed lines indicate the assumed baselines of the three peaks.

On the PPS surface, the reaction induced by 8.00 MeV ^{4}He produces 5.83 MeV protons in the 0° direction, which is concluded from the conservation of momentum and energy including the Q value. On the PPS backsurface, 7.90 MeV He produces 5.74 MeV protons in the 0° direction. The energies of these protons after escaping from the backsurface of Ni(20), which were calculated using the SRIM code, are indicated by red and blue arrows in Fig. 1. The corresponding energies for protons of p_1 and p_2 which result from transitions to the first (1.22 MeV) and the second (1.76 MeV) excited levels of ^{35}Cl, respectively, are also indicated in Fig. 1. The peaks for p_n ($n \geq 3$) were hardly recognized in the present experiments. We see in Fig. 1 that the observed peaks of p_0, p_1, and p_2 are produced mainly from the nuclear reaction near the backsurface of PPS, i.e., by 7.90 MeV He. This is consistent with the observations by Soltani-Farshi and coworkers, in which the differential cross section of the ^{32}S(α, p_0)^{35}Cl reaction for 7.90 MeV He is larger than for 8.00 MeV He in the 60–167° angular range of observation [3].

From the present experimental data, the differential cross section of the $^{32}\mathrm{S}(\alpha,\mathrm{p}_n)^{35}\mathrm{Cl}$ reaction at 0° for $n = 0, 1, 2$ can be determined. To do this, it is necessary to investigate whether the amount of S in the PPS film changes under the He^{2+} irradiation. Actually, the p_0 peak remained unchanged for incident He^{2+} charges of 4 μC and for additional 4 μC afterwards, indicating a fixed amount of S during the measurements.

The reaction yield Y_n, equal to the area under the p_n peak, can be obtained by assuming the baselines shown in red dashed lines. Y_n is related to the differential cross section $\mathrm{d}\sigma_n/\mathrm{d}\Omega$ by

$$Y_n = N_{\mathrm{He}} N_{\mathrm{S}} \frac{\mathrm{d}\sigma_n}{\mathrm{d}\Omega} \times \Delta\Omega \,, \tag{1}$$

where N_{He} is the number of incident He^{2+}, N_{S} is the area density of S in the PPS film viewed along the beam axis, and $\Delta\Omega = 0.01367\,\mathrm{sr.}$ is the solid angle of acceptance, which corresponds to the angular range of 0 to the detector's acceptance angle of 3.78°. In the present case, $N_{\mathrm{He}} = 2.483 \times 10^{13}$ and $N_{\mathrm{S}} = 1.102 \times 10^{18}$ cm^{-2} for PPS of 1.35 μm thickness. The results obtained from Eq. (1) are summarized in Table 1.

Table 1. Differential cross sections of the $^{32}\mathrm{S}(\alpha,\mathrm{p}_n)^{35}\mathrm{Cl}$ reaction at a recoil angle of 0°, determined for the He energy range of 7.90–8.00 MeV.

p_n	Y_n (counts)	$\mathrm{d}\sigma_n/\mathrm{d}\Omega$ (mb/sr)
p_0	2875	7.69 ± 0.14
p_1	827	2.21 ± 0.13
p_2	716	1.92 ± 0.12

Notably, the value of 7.69 ± 0.14 mb/sr for p_0 is in the same range of 5–10 mb/sr as for the reported differential cross sections [3]. The present data at a recoil angle of 0° provide additional knowledge about the $^{32}\mathrm{S}(\alpha,\mathrm{p}_n)^{35}\mathrm{Cl}$ reaction.

References

[1] H. Kudo et al., J. Phys.: Condens. Matter 34 (2022) 435902.

[2] P. Mohr, Eur. Phys. J. A 5 (2015) 56.

[3] M. Soltani-Farshi et al., Nucl. Instrum. Meth. Phys. Res. B 113 (1996) 399.

2.3 Cluster effects on convoy electron yield of fast H_2^+ at 292 keV/u

S. Hatada, G. Kawasaki, M. Hiraga, Y. Shiina[1], S. Ishii, T. Takahashi, K. Sasa, S. Tomita

When fast molecular ions are incident on a material, the constituent atoms of the molecular ion impinge on a narrow range of the material simultaneously. In this case, the interatomic distances of the impinging atoms may be considered to be shorter than the impact parameter for the collective electron excitation in the material. Therefore, the response of electrons by molecular ion injection should differ from that by single-atomic ion injection. Such phenomenon is known as the cluster effect. In fact, the electronic energy loss of a fast atomic ion injected as a constituent of a molecular ion is distinct from that of a single atomic ion. This difference is due to the interference of the collective electron response caused by the individual constituent atoms of the incident molecular ion [1].

A cluster effect resulting from the electron response of the material has been reported previously, indicating a significant reduction in the secondary electron yield [2] and a substantial enhancement in the convoy electron yield for C_2^+ at 42 keV/u and 292 keV/u [3, 4]. This effect is believed to stem from the difference in the transport processes of scattered electrons in the material. Understanding this cluster effect could provide valuable insight into the radiation damage of biomolecules such as DNA molecules, as scattered electrons and other radicals generated by the penetration of fast-charged particles can cause radiation damage. To examine the dependence on the effective charge of the projectile ion, we measured the cluster effect of convoy electron yield for H_2^+ at 292 keV/u.

A series of experiments has been conducted using the 1MV Tandetron accelerator at UTTAC. The H_2^+ ions were accelerated and transported to the experimental chamber, where they penetrated thin carbon foils provided by ACF-Metals, The Arizona Carbon Foil Co., Inc. The nominal thicknesses of the foils used in the experiments are 11.2, 19.3, and 59.8 μg/cm^2. A 45° parallel-plate electrostatic spectrometer of double deflection type with a 3% energy resolution was used to analyze the energies of electrons emitted in the beam direction. The electrons were counted by a Channeltron detector whose anode potential was carefully set to +100V to obtain the maximal detection efficiency. To cancel out geomagnetism, a triaxial square Helmholtz coil surrounded the experimental chamber. The energy spectra were accurately normalized with the number of signals of backscattered ions from the bulk Au target, which was periodically inserted on the beamline.

Figure 1 shows energy spectra of the secondary electrons emitted from the carbon foil of 11.2 μg/cm^2, resulting from penetration of 292 keV/u H^+ and H_2^+ ions. The convoy electrons can be recognized at approximately 150 eV, hence the convoy electron yield is obtained by the area under the convoy peak. It should be noted that no essential difference is perceived between the convoy electron yields per atom induced by H^+ and H_2^+. Figure 2 shows dependence of the ratio of the convoy electron yield per constituent H atoms on the carbon foil thickness, together with the previous data for C^+ and C_2^+. Again for H^+ and H_2^+, there is only a minor difference between the convoy electron yields for the foil thicknesses of 19.3 or 59.8

---

[1] Rikkyo University

μg/cm^2, in contrast to the case of C$^+$ and C$_2^+$. As the target becomes sufficiently thick, multiple collisions with the target atoms primarily determine the interatomic distances between the injected atoms. According to the TRIM simulation of atomic ion injection, the interatomic distance for H$_2^+$ is shorter than that of C$_2^+$. These results indicate importance of the effective charge of the constituent atom in considering the cluster effect on the convoy electron yield.

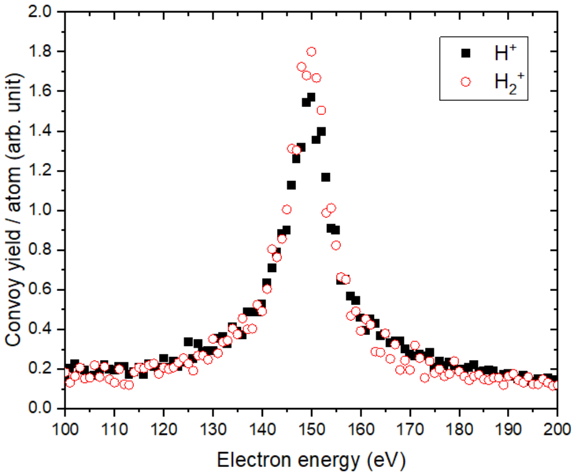

Fig. 1. Energy spectra of zero-degree electrons emitted from a carbon foil of 11.2 μg/cm^2 in thickness.

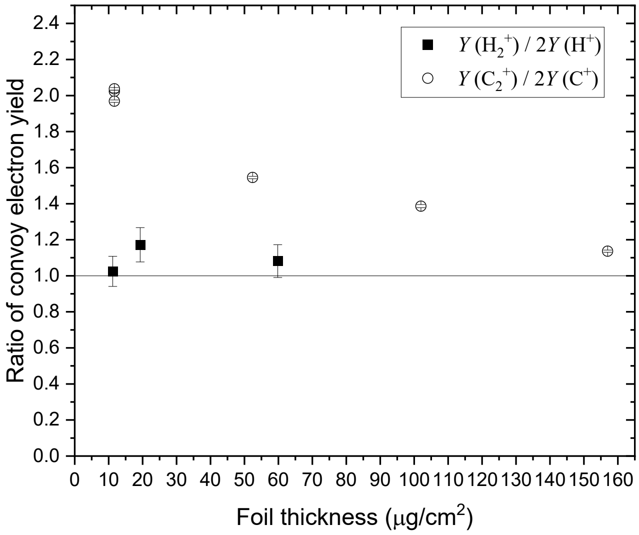

Fig. 2. Dependence of the ratio of the convoy electron yield per constituent atom on the carbon foil thickness. The incident energy of the dimer and monomer ions of H and C is 292 keV/u.

References

[1] W. Brandt et al., Phys. Rev. Lett. 33 (1974) 1325.
[2] H. Arai et al., J. Phys. Soc. Jpn. 78 (2009) 104301.
[3] S. Tomita et al., Phys. Rev. A 73 (2006) 060901.
[4] Y. Shiina et al., Nucl. Instr. Meth. Phys. Res. B 460 (2019) 30.

2.4 Improvement of PIXE system using superconducting tunnel junction X-ray detectors

S. Shiki[1], S. Tomita, S. Ishii, S. Hatada, K. Sasa

Superconducting tunnel junction (STJ) detector is promising for soft X-ray spectroscopy due to its high sensitivity, high energy resolution, and high counting rate [1]. Particle Induced X-ray emission equipped with SuperConducting tunnel junction detector array (SC-PIXE) will expand the energy coverage of PIXE down to the soft X-ray region where light elements are visible. The detection of Al-K line was reported with an energy resolution of 50 eV full width at half maximum (FWHM) using the SC-PIXE [2]. However, it was difficult to observe light elements having K-lines at energies less than 1 keV, because the pulse height spectrum was polluted by the events caused by scattered protons in the sample. Therefore, thin samples are used to reduce scattered protons.

The SC-PIXE system is placed in the μ-PIXE beam line at UTTAC [3]. The details of the experiment are as follows. The STJ spectrometer consists of a helium three cryostat, an STJ detector array of 512 pixels, 16-channel charge sensitive amplifies, and multichannel analyzer having 16-inputs. The temperature of the cold stage was approximately 320 mK. The beam current of 4 MeV H^+ was 1–10 nA. The distance from the beam spot to an STJ detector is approximately 100 mm. The sample is 7.5 μm thick polyimide.

Figure 1 shows a pulse height spectrum of an STJ pixel. The spectrum shows a clear peak at a pulse height of ~143 channel. This peak is due to the C-Kα line. The energy resolution is 21 eV in FWHM, which is better than that of silicon drift detectors.

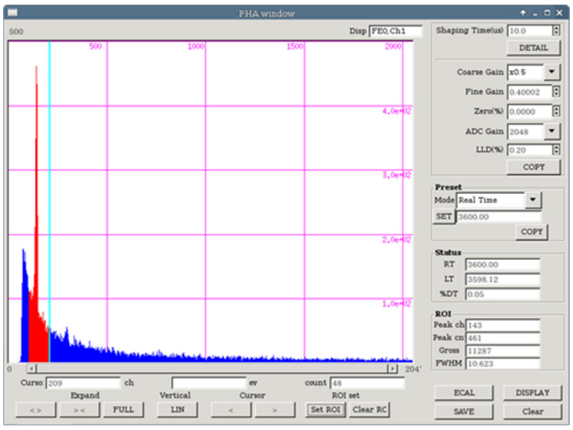

Disp FE0,Ch1

Shaping Time(us) 10.0

Coarse Gain x0.5

Fine Gain 0.40002

Zero(%) 0.0000

ADC Gain 2048

LLD(%) 0.20

Preset

Mode Real Time

SET 3600.00

Status

RT 3600.00

LT 3598.12

%DT 0.05

ROI

Peak ch 143

Peak cn 461

Gross 11287

FWHM 10.623

Curso 209 ch

ev

count 48

Fig. 1. Pulse height spectrum of an STJ pixel. The sample is 7.5 μm thick polyimide. The main peak is due to the C-Kα line.

References

[1] S. Shiki et al., J. Low Temp. Phys. 167 (2012) 748.
[2] S. Shiki et al., UTTAC Annual Report 2021, UTTAC-91 (2022) 16.
[3] A. Yamazaki et al., Nucl. Instr. Meth. Phys. Res. B 404 (2017) 92.

---

[1] National Institute of Advanced Industrial Science and Technology (AIST)

3.

ACCELERATOR MASS SPECTROMETRY

Processing of seawater samples for I-129 measurement. The seawater data is complementary with the data of the lake sediments.

––– *Report 3.2*

3.1 Status report of the Tsukuba 6MV multi-nuclide AMS system in FY2022

K. Sasa, T. Takahashi, M. Matsumura, A. Sakaguchi, T. Matsunaka[1]

The Tsukuba 6MV multi-nuclide AMS system was operated for a total of 40 days and 645.4 hours in FY 2022. Figure 1 shows monthly-measured rare nuclides from April 2022 to March 2023. We measured 579 samples in total dealing with rare radionuclides such as ^{36}Cl and ^{129}I, as shown in Table 1.

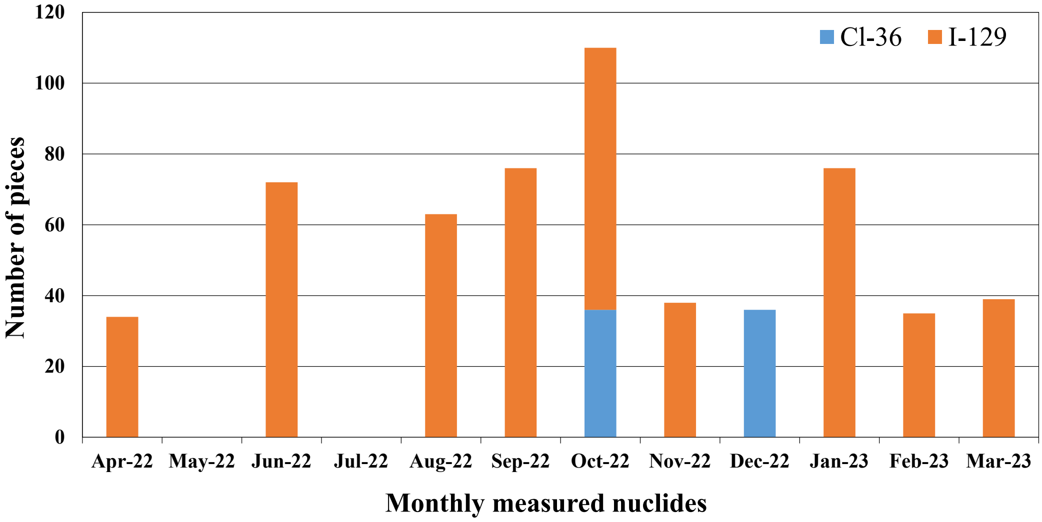

Fig. 1. Monthly-measured nuclides from April 2022 to March 2023.

Table 1. Number of measured ^{36}Cl and ^{129}I samples in FY2022.

Item	Reagent & Blank samples	Standard samples	Analyzed samples	Total
Cl-36	11	16	45	72
I-129	51	50	406	507
Sub total	62	66	451	579

^{36}Cl-AMS

^{36}Cl-AMS has been performed under the beam condition of ^{36}Cl^{7+} with 48.0 MeV using a carbon foil stripper at the terminal voltage of 6 MV. The background ratios of ^{36}Cl/Cl ~ 3×10^{-15} were achieved with AgCl blank samples. In FY2022, ^{36}Cl-AMS was mainly applied for tracing anthropogenic ^{36}Cl in an ice core from the H15 site in Dronning Maud Land, East Antarctica. We have been able to obtain a detailed record of the variability of ^{36}Cl produced by nuclear bomb tests [1].

^{129}I-AMS

^{129}I-AMS has been performed under the beam condition of ^{129}I^{5+} with 30.0 MeV using an Ar gas stripper

---

[1] Kanazawa University

at the terminal voltage of 5 MV. The background ratios of ^{129}I/I ~ 2 × 10^{-14} were achieved with AgI blank samples prepared from "Old iodine" (Deepwater Chemicals). Anthropogenic radioactive ^{129}I is used as an environmental isotope tracer. In FY2022, ^{129}I-AMS was mainly applied to ^{129}I tracer studies for soil and river samples related to the Fukushima Daiichi Nuclear Power Plant (FDNPP) accident and ocean circulation studies in the Southern Ocean [2].

In 2023, ALPS-treated water stored at the FDNPP is to be discharged into the sea surrounding the plant. We have started to check ^{129}I concentrations in sea water, relating to ALPS-treated water around the FDNPP. The purpose of this study is to clarify the temporal changes in the concentration of ^{129}I in seawater and sediments that could be caused by the discharge of ALPS-treated water to the sea, and to evaluate the impact.

Measurement history

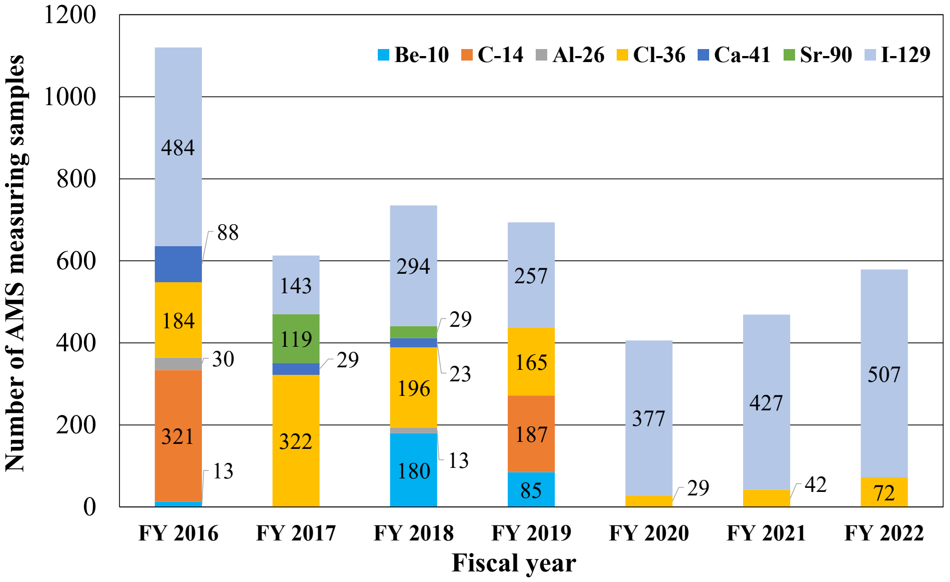

Fig. 2. Cumulative number of measured samples for AMS since 2016.

Figure 2 shows the cumulative number of measured samples since the AMS system started operation. A total of 4,616 samples was measured from FY2016 to 2022. AMS of the radioactive halogens ^{36}Cl and ^{129}I has been the main focus at the Tsukuba 6MV multi-nuclide AMS system since FY2020. Currently, AMS developments are underway for ^{135}Cs (a half-life of 2.3 million years) and ^{210}Pb (a half-life of 22.2 years) as new nuclides. We developed the rubidium (Rb) sputtering negative ion source by replacing Cs of the S-5 ion source (MCG-SNICS) with Rb [3]. Sample chemistries and additives are being developed for the ^{135}Cs and ^{210}Pb samples to be loaded in the Rb negative ion source.

References

[1] K. Horiuchi et al., this Annual Report 3.2.
[2] T. Matsunaka et al., this Annual Report 3.3.
[3] D. Shiine et al., UTTAC Annual Report 2021, UTTAC-91 (2022) 23.

3.2 Anthropogenic I-129 depositions at the Noto Peninsula since 1950

T. Matsunaka[1], S. Ochiai[1], M. Matsumura, T. Takahashi, A. Sakaguchi, K. Sueki, K. Sasa

The investigation of water dynamics change in the Sea of Japan caused by the recent global warming is essential for forecasting the response of ocean circulation to climate change. Anthropogenic ^{129}I ($T_{1/2}$: 15.7 million years) produced from thermal neutron fission, is dominated by release from nuclear fuel reprocessing plants in Europe and supplied at the Sea of Japan via atmospheric deposition, surface runoff, and oceanic current. The long-lived ^{129}I is expected as an oceanic tracer of surface and vertical circulations in the Sea of Japan. This study aimed to illuminate the historical change of ^{129}I deposition around the Sea of Japan since 1950 through the analysis of ^{129}I in lake sediments from the Noto Peninsula facing the Sea of Japan.

Lacustrine sediment core collected in 2011 from the Noto Peninsula, divided into 1 cm pieces, was used for the analysis of ^{210}Pb, ^{137}Cs, and ^{129}I. Homogenized dried sediments (dry weight: about 1.5 g) were sealed in plastic containers, and ^{210}Pb and ^{137}Cs were measured using a Ge semiconductor detector at Low Level Radioactivity Laboratory (LLRL), Kanazawa University. Extraction and purification of ^{129}I in the sediments by thermal hydrolysis and solvent extraction were carried out at LLRL. After isotope dilution by adding 1 mg of ^{127}I carrier (Deepwater iodine, ^{129}I/^{127}I: $\sim 1\times10^{-14}$) to an alkaline solution with trapped combustion gas produced from the sediment (0.5 g), iodine was purified by solvent extraction and back extraction and AgI targets were prepared by adding $AgNO_3$. The AgI precipitate was then washed with NH_4OH and ultra-pure water and dried and loaded into an Al holder with Nb powder. The ^{129}I/^{127}I ratio of the target was measured using the AMS system at the University of Tsukuba. A terminal voltage of 5 MV and a charge state of 5+ were chosen for acceleration and detection. The measured ratios were normalized against the Purdue-1 reference material, which has a ^{129}I/^{127}I ratio of 8.37×10^{-12} and is obtained from Purdue University, USA. ^{127}I in the alkaline solution was measured by ICP–MS. The original ^{129}I/^{127}I ratios and ^{129}I concentrations in the sediment were calculated using ^{127}I concentration from ICP-MS and the ^{129}I/^{127}I ratio from AMS.

Excess ^{210}Pb ($^{210}Pb_{ex}$) concentrations in the sediments range from 84.2–739 Bq kg^{-1} from the surface to a depth of 29 cm and are undetectable deeper than 29 cm. Depth profiles of $^{210}Pb_{ex}$ with mass depth (g cm^{-2}) were analyzed for sedimentation rates, i.e., 0.836 g cm^{-2} yr^{-1} (0–7.5 cm), 0.0638 g cm^{-2} yr^{-1} (7.5–15.5 cm), 0.219 g cm^{-2} yr^{-1} (15.5–24.5 cm), and 0.0332 g cm^{-2} yr^{-1} (24.5–29.0 cm) (Fig. 1). The Cs-137 concentration ranges from 8.6–71.2 Bq kg^{-1} (decay-corrected to the sampling date) from the surface to a depth of 29 cm, with a maximum at a depth of 26–27 cm formed in 1962 (Fig. 1). Deposition of ^{129}I in the lake sediments was in the range 0.004–77.8 nBq cm^{-2} yr^{-1} (^{129}I activity: 0.13–93.0 μBq kg^{-1}) and increased after 1946, with the maximum levels being recorded in 1980 and 2011 (Fig. 2). These distributions revealed an increase of atmospheric ^{129}I deposition around the Sea of Japan related to nuclear fuel reprocessing since 1950 and a nuclear accident in 2011.

---

[1] Kanazawa University

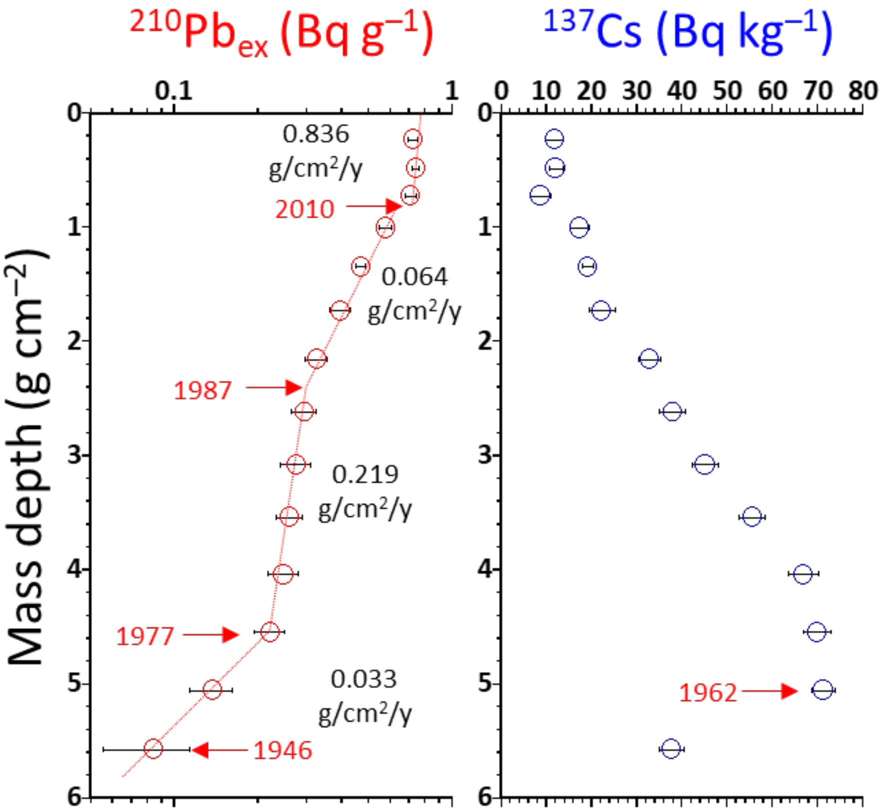

Fig. 1. Depth profiles of $^{210}Pb_{ex}$ and ^{137}Cs activity for the 63-cm-long lacustrine sediment collected from the Noto Peninsula.

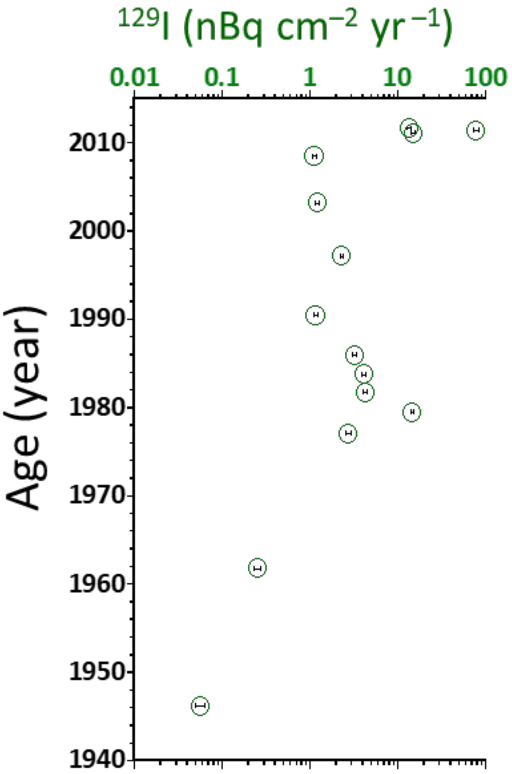

Fig. 2. Depth profiles of ^{129}I flux for the 63-cm-long lacustrine sediment collected from the Noto Peninsula.

3.3 The performance of iodine-129 AMS measurements at the University of Tsukuba (FY2022)

M. Matsumura, K. Sasa, T. Takahashi, A. Sakaguchi, T. Matsunaka[1], K. Sueki

Continuing from 2017, we have reported the performance of ^{129}I measurements by accelerator mass spectrometry (^{129}I AMS) [1, 2]. From April 2022 to March 2023, we measured 507 samples of ^{129}I by preparing the AgI targets, the details of which are shown in Fig. 1. The test samples were not only iodine-trapping-solutions, but also those chosen from natural environment such as sea, rain, river water, suspended sand, and sediments. Figure 2 shows the measured blank values of AgI precipitated from carrier-reagent.

The machine background is estimated to be on the order of 10^{-15} in terms of the ^{129}I/^{127}I ratio, which is sufficiently lower than the background level of the ratio of 2×10^{-14} for "old Iodine" provided from Deep Water company, USA. However, the measured ^{129}I/^{127}I values in blanks sometimes ranged over ten times higher than 2×10^{-14}. One of the causes for this might be the memory effect. The rise in blank values in 2018 and 2019 is most likely caused by this memory effect, however, this effect has been prevented by the improved measurement schemes since 2020. This means that we can succeed in decreasing the memory effect by improvements of the measurement method.

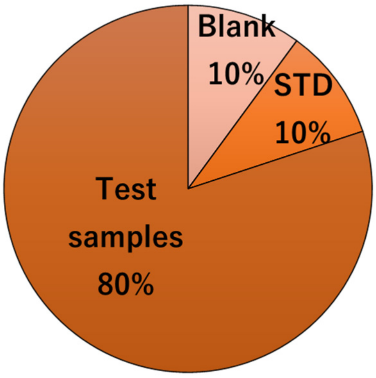

Fig. 1. Details of measured ^{129}I by the AMS system in fiscal 2022.

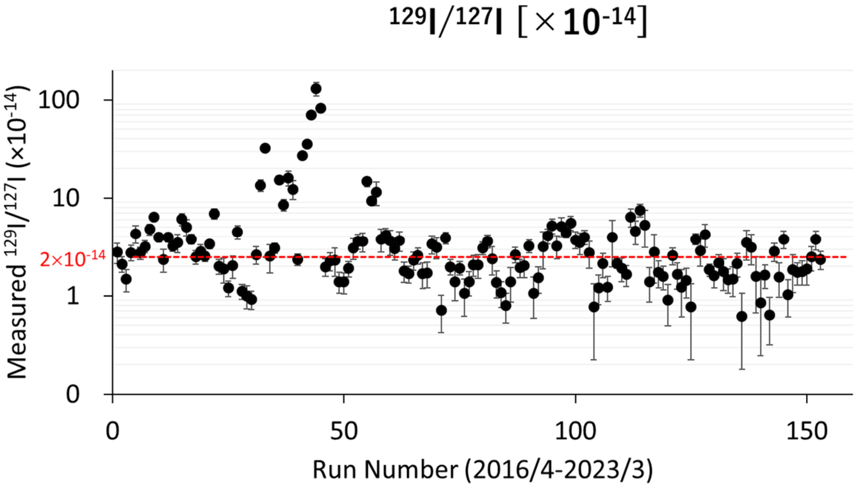

Fig. 2. ^{129}I/^{127}I ratios in blanks.

The measured ^{129}I/^{127}I values were normalized by using Standard Reference Material (SRM), Purdue-1 STD (Z94-0597) and Purdue-2 STD (Z94-0596) with an ^{129}I/^{127}I ratio of 8.378×10^{-12} and 6.540×10^{-11} [3] (the value was revised in 2014 [4]), which was provided by the Purdue Rare Isotope Measurement Laboratory (PRIME Lab) at Purdue University, USA. The routine measurement method of SRM is as follows: SRM-AgI was divided into two or three target cathodes and each target was measured four times with a measurement time of 2 min, while the measurement interval was three or four hours. The average beam currents were 1.6 μA and 1.4 μA for Purdue-1 and Purdue-2, respectively. For each run, the first

---

[1] Kanazawa University

measurement was excluded from the data file since it was treated as "sputter-cleaning". Figures 3 and 4 are typical results of Purdue-1 measurements in the same beam time. In fiscal 2022, the resulting ratios with its standard deviation (1σ) are (7.600 ± 0.459) × 10^{-12} (6.0%) and (5.927 ± 2.080) × 10^{-11} (3.5%) for Purdue-1 (run number 747) and Purdue-2 (run number 54), respectively. The ratios of (average of measurement value) / (nominal value) are 0.907 and 0.906 for Purdue-1 and Purdue-2, respectively, which are in good agreement.

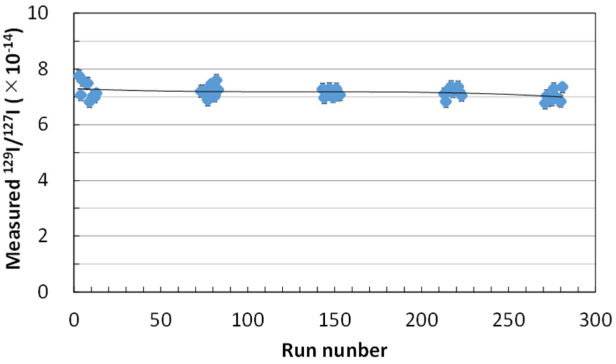

Fig. 3. Typical results of ^{129}I/^{127}I ratio measured for Purdue-1. The average ratio with the standard deviation (1σ) was (7.163 ± 0.226) × 10^{-12} (3.2%) at this beam time.

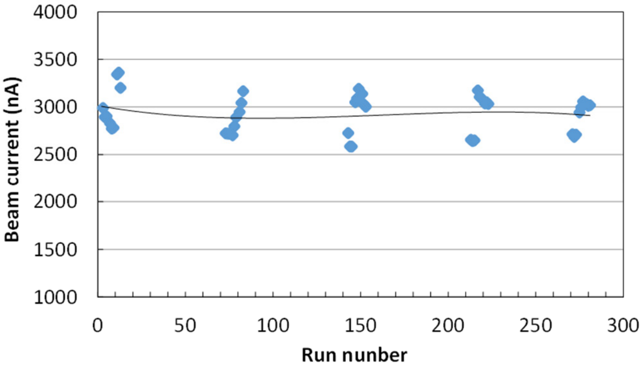

Fig. 4. Beam current during the measurements. The average beam current was 2.9 μA at this beam time.

This work was supported in part by JSPS KAKENHI Grant Numbers 22H02001 and 22H04441.

References

[1] K. Sasa et al., Nucl. Instrum. Meth. Phys. Res. B 437 (2018) 98.
[2] M. Matsumura et al., UTTAC Annual Report 2019, UTTAC-89 (2020) 16.
[3] P. Sharma et al., Nucl. Instrum. Meth. Phys. Res. B 123 (1997) 347.
[4] M. Caffee, (Purdue University), Private communication (2014).

3.4 Investigation of Iodine-129 deposition from atmosphere in the sample preparation rooms for AMS in Japan (FY2022)

M. Matsumura, K. Sasa, T. Matsunaka[1], T. Takahashi, A. Sakaguchi, K. Sueki

Through the chemical treatment of samples with high ^{129}I concentrations, the workspace used to prepare samples tends to become gradually contaminated. Such contamination may lead to overestimated ^{129}I in accelerator mass spectrometry (AMS) analyses. Environmental contamination monitoring of ^{129}I from the atmosphere in sample preparation rooms, as shown in Fig. 1, was performed at ten Japanese institutions, i.e., Japan Atomic Energy Agency (Aomori Research and Development Center), Japan Atomic Energy Agency (Tono Geoscience Center), Ehime University (Advanced Research Support Center), Fukushima University (The Institute for Environmental Radioactivity), Kanazawa University (Institute of Nature and Environmental Technology), Kumamoto University (Institute of Resource Development and Analysis), Okayama University (Neutron Therapy Research Center), Tottori University (Division of Radioisotope Science Research Initiative Center), The University of Tokyo (Micro Analysis Laboratory, Tandem accelerator), and University of Tsukuba. The sampling was carried out in July and August 2022, and February 2023. The ambient level of atmospheric ^{129}I in each room was estimated from the measured concentrations in the alkali trap solutions [1–3]. The alkaline solutions in the sampling bottles were left for two or three weeks. To check the difference in the ^{129}I contamination risks from atmosphere between inside and

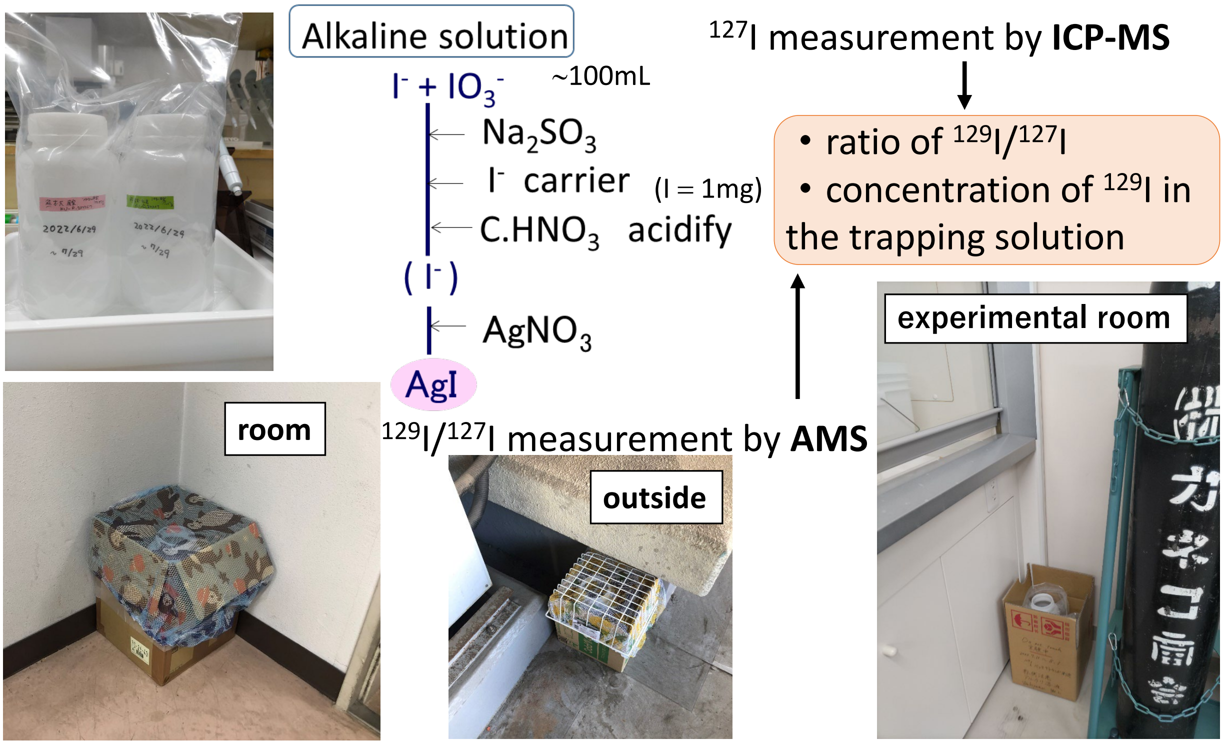

Fig. 1. Iodine sampling from atmosphere into the alkaline solution. The "room" means an area untreated chemically, while "experimental room" means such as a sample preparation room, an ICP-MS room, and an AMS-target preparation room.

---

[1] Kanazawa University

outside the facility, the sampling bottles were left at places outside the seven institutions, where the rainwater never entered the bottles. The ^{129}I contamination risk [atoms cm^{-2} day^{-1}] was estimated from ^{129}I concentration [atoms g^{-1}]. The experimental procedure was similar to the previous case [1], except that we used a different carrier reagent" Old Iodine" provided from Deep Water company, USA [2, 4], with an ^{129}I/^{127}I ratio of 2×10^{-14}.

Figure 2 shows the monitoring results of the ^{129}I contamination rates in the Japanese institutions, obtained in this manner. In most of the institutions, the amounts of ^{129}I are on the order of 10^3 or 10^4 atoms cm^{-2} day^{-1} in the rooms, which are one or two orders of magnitude lower than the environmental background level, 3×10^5 atoms cm^{-2} day^{-1}. In the two rooms of University of Tsukuba, the ^{129}I contamination rates were higher than the background level for the reason previously described [1–3]. A clear difference is not found between the ^{129}I contamination risks from atmosphere inside and outside. This suggests that the atmospheric ^{129}I level in the nine institutions (A to I) is lower than the environmental background level 3×10^5 atoms cm^{-2} day^{-1} [5], hence there is almost no ^{129}I contamination risk of the samples from atmosphere.

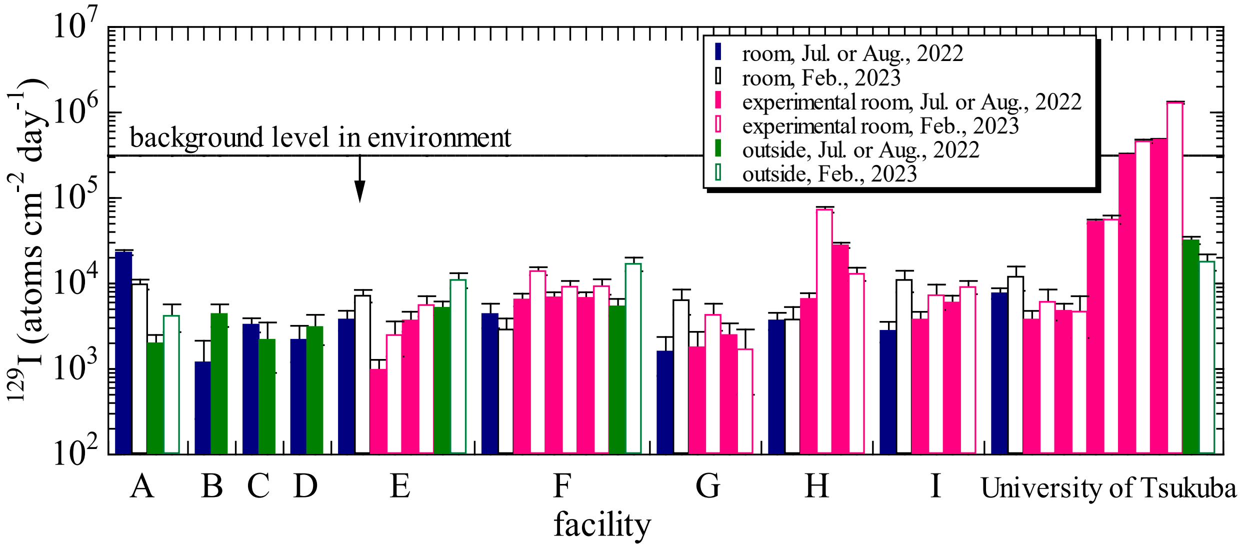

Fig. 2. Measured ^{129}I contamination rates from atmosphere at the institutions indicated anonymously by A to I, except University of Tsukuba.

This work was supported in part by JSPS KAKENHI Grant Numbers 22H04441 and 22H02001.

References

[1] M. Matsumura et al., Anal. Sci. 36 (2020) 631.

[2] M. Matsumura et al., UTTAC Annual Report 2020, UTTAC-90 (2021) 23.

[3] M. Matsumura et al., Proceedings of the 23rd Symposium on The Japanese Society of Accelerator Mass Spectrometry Research (2022) 84.

[4] M. Matsumura et al., this Annual Report 3.3.

[5] M. Matsumura et al., Geochemical Journal 52 (2018) 155.

3.5 Chlorine-36 in an ice core from the H15 site in Dronning Maud Land, East Antarctica

K. Horiuchi[1], K. Sato[1], R. Yagihashi[1], K. Sasa, M. Matsumura, T. Takahashi, H. Motoyama[2]

Chlorine-36 (^{36}Cl) is a radioisotope of chlorine with a half-life of 301 kyr. Prior to the Atomic Era, ^{36}Cl in the environment was largely produced by spallation reactions between cosmic ray particles and target atoms (i.e. cosmogenic production). However, with the advent of atomic bomb testing, anthropogenic ^{36}Cl began to be produced by thermal neutron activation of the ^{35}Cl of sea salts. In particular, extensive marine testing in the 1950s and '60s is thought to have produced a large bomb peak of ^{36}Cl reported from a dozen ice cores worldwide [1-3].

In this study, we determined ^{36}Cl concentrations in an ice core from the H15 site (69°04'10"S, 40°44'51"E) in Dronning Maud Land, East Antarctica (Fig. 1). The core is 32.01 meters long and is estimated to cover the last 80 to 90 years. The ^{36}Cl was analyzed at the University of Tsukuba Tandem Accelerator Complex (UTTAC) using a common procedure for ice core ^{36}Cl analysis [4, 5].

The ^{36}Cl concentration varies by two orders of magnitude from 1.0×10^3 to 3.0×10^5 atoms/g (Fig. 2). A distinct ^{36}Cl peak is found between ~20 and 25 m depth, reflecting a bomb peak of ^{36}Cl at this location. The maximum of the peak is between 22.5 and 23.4 m depth, corresponding to the late 1950s in the age model of the core. The nature and cause of the ^{36}Cl variations will be further investigated.

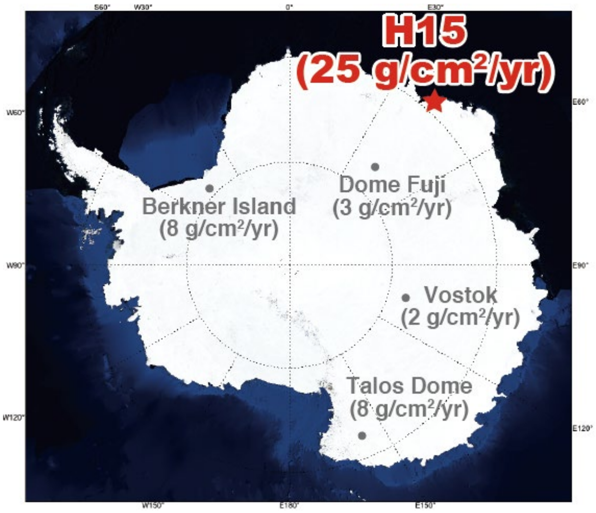

Fig. 1. Location of the core site (H15).

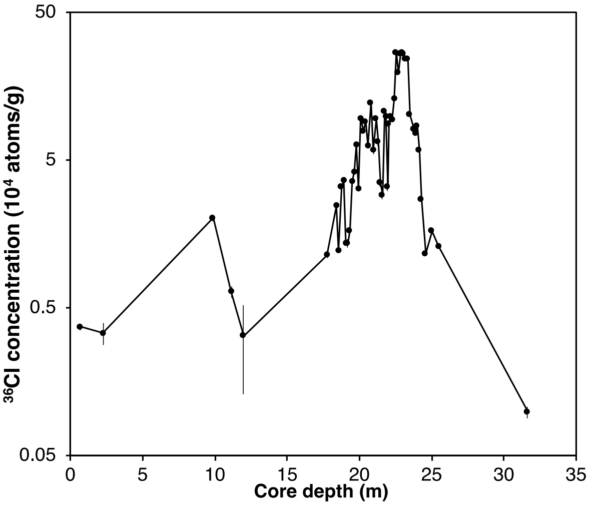

Fig. 2. Depth profile of ^{36}Cl concentrations.

References

[1] D. Elmore et al., Nature 300 (1982) 735.

[2] U. Heikkilä et al., Atmos. Chem. Phys. 9 (2009) 4145.

[3] S. Pivot et al., J. Geophys. Res.: Atmospheres 124 (2019) 10973.

[4] K. Sasa et al., Nucl. Instr. Meth. Phys. Res. B 268 (2010) 1193.

[5] K. Kanzawa et al., J. Geophys. Res.: Space Phys. 126 (2021) e2021JA029378.

---

[1] Hirosaki University

[2] National Institute of Polar Research

4.

MATERIALS RESEARCH

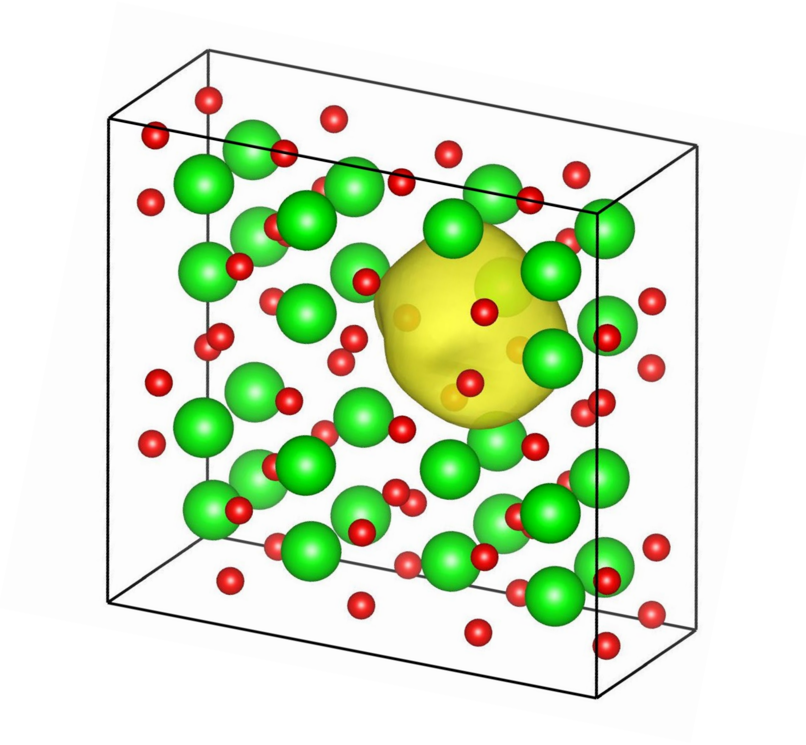

Simulated density distribution of positrons (yellow) trapped by a Zr vacancy coupled with four oxygen vacancies. Green and red circles correspond to Zr and O atoms, respectively.

––– *Report 4.1*

4.1 Impact of cation vacancies on leakage current on TiN/ZrO_2/TiN capacitors studied by positron annihilation

A. Uedono, N. Takahashi, R. Hasunuma, Y. Harashima[1], Y. Shigeta, Z. Ni[2], H. Matsui[2], A. Notake[3], A. Kubo[3], T. Moriya[4], K. Michishio[5], N. Oshima[5], S. Ishibashi[5]

High-dielectric constant (*k*) oxides such as ZrO_2 and HfO_2 have been extensively studied as an insulator for DRAM because of their high *k* value, large bandgap, kinetic stability, their device process compatibility, etc. [1]. Because these oxides are fast ion conductors, oxygen vacancies (V_Os) are easily introduced during the device process. Such defects are one of the origins causing current leakage and affect the stability of the crystal phase of high-*k* films. For high-*k* based devices, TiN is often used as the top and bottom electrodes. The capacitor with TiN electrode tends to show large leakage current, which is often attributed to the introduction of V_O due to the scavenging effect of TiN. Positron annihilation is a useful technique to detect vacancy-type defects and open spaces in solid state materials with non-destructive manner [2]. In the present study, we used monoenergetic positron beams to study the behaviors of vacancy-type defects in TiN/ZrO_2/TiN capacitors [2].

The sample structure used in the present experiments is ZrO_2(10 nm)/TiN(5 nm)/SiO_2(300 nm)/Si. TiN and ZrO_2 layers were deposited by using physical vapor deposition. SiO_2 layers were thermally grown on Si substrates. A TiN bottom electrode was deposited on SiO_2/Si through the reactive sputtering of a pure Ti target. Then, ZrO_2 layers were deposited on the TiN layers. For some samples, a 5-nm thick TiN was deposited on the sample as a top electrode. Forming gas annealing was performed at 550°C for 5 min in a N_2 atmosphere for the samples with and without the top TiN layer.

Vacancies in the ZrO_2 layers were probed using the positron annihilation technique [2]. The Doppler broadening spectra of the annihilation radiation were measured by Ge detectors as a function of the incident positron energy *E* and characterized using the *S* parameter. The lifetime spectra of positrons were also measured. The positron lifetimes in monoclinic ZrO_2 were calculated using the quantum materials simulator code [4].

Figure 1 shows current–voltage (*J*–*V*) relationships of the samples before and after post-deposition annealing. The bias voltage was applied to the top

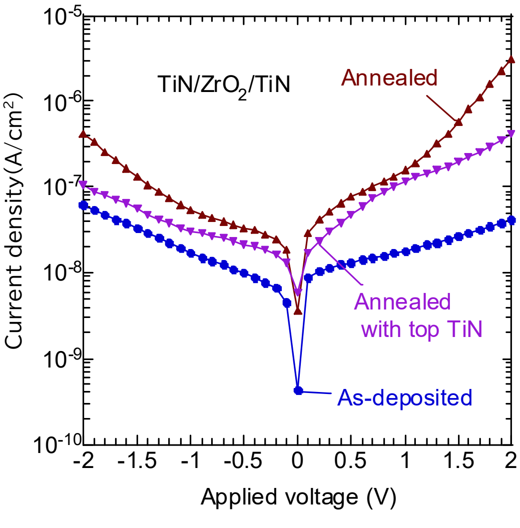

Fig. 1. *J*–*V* curves for samples before and after post-deposition annealing. Annealing was done with and without the top TiN layer.

---

[1] Nara Institute of Science and Technology
[2] Tokyo Electron Technology Solutions Ltd.
[3] Tokyo Electron Ltd., Sapporo
[4] Tokyo Electron Ltd., Tokyo
[5] National Institute of Advanced Industrial Science and Technology (AIST), Tsukuba

electrode while the bottom electrode was grounded. The current density was increased by post-deposition annealing, and this tendency was suppressed by annealing with the top TiN layer.

Figure 2 shows the *S* values as a function of *E* for the samples before and after annealing. The *S* value at *E*=1−1.5 keV can be associated with mainly the annihilation of positrons in the ZrO_2 layer. The *S* value for the annealed ZrO_2 layers was higher than that for as-deposited one, suggesting the size of vacancies increased by annealing. This tendency was suppressed by the annealing with the top TiN layer.

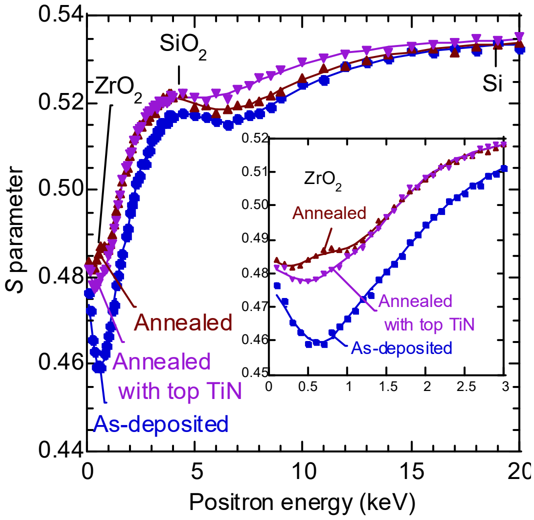

Fig. 2. *S* parameters as function of incident positron energy *E* for samples before and after post-deposition annealing. Inset shows *S*–*E* curves corresponding to subsurface region.

The mean positron lifetimes for the ZrO_2 layers for the as-deposited and annealed ZrO_2 were obtained as 300 ps and 400–430 ps, respectively. The lifetimes of positrons trapped by the vacancy clusters consisting of a Zr vacancy (V_{Zr}) and V_os [$V_{Zr}(V_O)_n$] were simulated, and they are obtained as 251, 260, 276, 294, 315, 339 ps for $V_{Zr}(V_O)_n$ (n=1–6), respectively. From a comparison between the experimentally obtained lifetimes and the ones calculated by using the computer simulation, the defect species in the as-deposited ZrO_2 layer was identified as $V_{Zr}(V_O)_4$. Figure 3 shows simulated atomic configurations of the super cell with $V_{Zr}(V_O)_4$ and (b) distribution of the positron density around the defect (shown as yellow). For the annealed samples, the observed longer positron lifetimes suggest an introduction of vacancies larger than V_{Zr}-type defects.

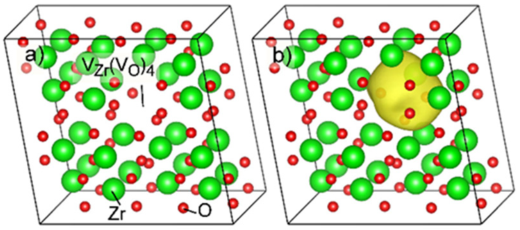

Fig. 3. (a) Atomic configuration of super cell with $V_{Zr}(V_O)_4$ and (b) distribution of the positron density around the defect. Green and red circles correspond to Zr and O atoms, respectively.

The present experiments showed that positron annihilation parameters are sensitive to vacancy-type defects in high-*k* based capacitors, and the defects that are detectable using positron annihilation are closely related to leakage current mechanisms. A monoenergetic positron beam, therefore, can provide useful information for the process parameter adjustment of memory devices.

References

[1] J. Robertson and R. M. Wallace, Mat. Sci. Eng. R 88 (2015) 1.

[2] R. Krause-Rehberg and H. S. Leipner, Springer Series in Solid-State Sciences, vol. 127, Springer-Verlag, Berlin, 1999.

[3] A. Uedono et al., Thin Solid Films 762 (2022) 139557.

[4] S. Ishibashi et al., J. Physics.: Condens. Matter 31 (2019) 475401.

4.2 Superparamagnetic relaxation of magnetic nanoparticles studied with Mössbauer spectroscopy

E. Kita, R. Onodera[1], M. Kishimoto, H. Yanagihara

Investigation of nano-particle relaxation behavior is useful for obtaining improved magnetic hyperthermia performance. Many researchers have analyzed the relaxation characteristics of super-paramagnetic nano-particles and their suspensions. AC susceptibility (ACS) measurements are commonly used to determine the frequency dependent response of magnetization including any relaxation in the frequency range of up to 1 MHz. Conventional magnetization measurements were performed using a vibrating sample magnetometer and ACS testing, covering a wide range of frequencies. Mössbauer spectroscopy (MS) of ^{57}Fe has a characteristic relaxation time of 10^{-7} s due to the lifetime of the excited state of ^{57}Fe nuclei. MS shows drastic changes in SP material spectra upon sample temperature changes.

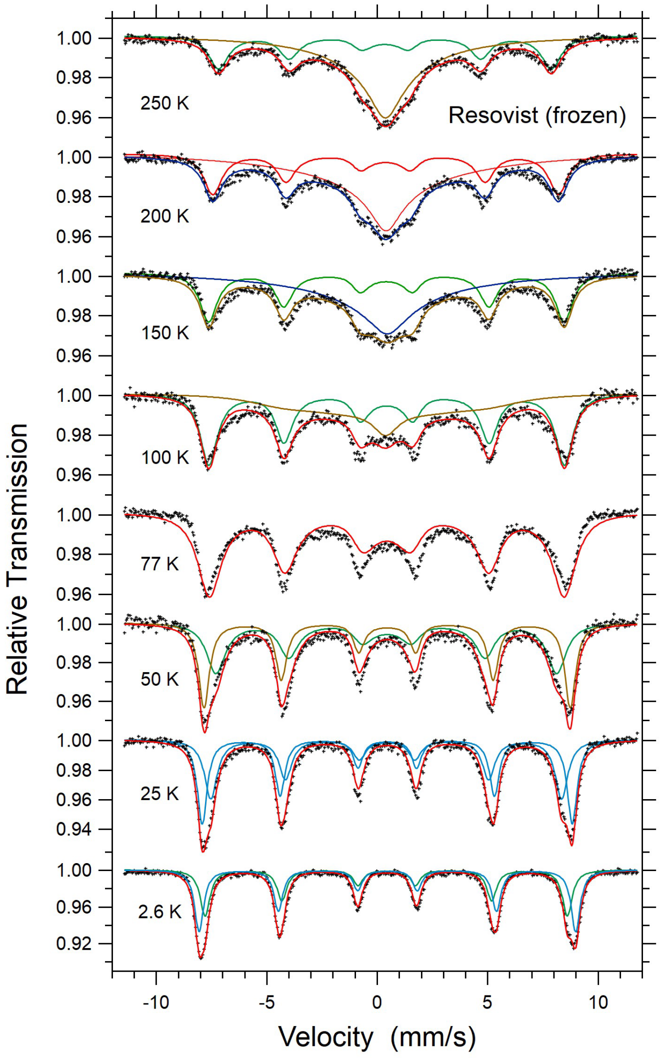

Fig. 1. Mössbauer spectra of Resovist recorded at temperatures between 2.6 K and 250 K [2].

We have reported ^{57}Fe MS measurements performed on a commercially available magnetic fluid, Resovist, which is used as a heat mediator in magnetic hyperthermia and magnetic particle imaging (MPI) and detailed conditions of MS measurements were described elsewhere [1, 2]. MS study was performed with varying sample temperatures between 2.6 and 250 K. Mössbauer spectra were analyzed with a combination of a few relaxed sub-spectra originated from the particle size distribution reported by other researchers [3]. Relaxation times (τ_{BT}) were obtained experimentally from the analysis based on the Blume-Tjon (BT) model [4] and Néel relaxation time was discussed from these data. Temperature variation of Mössbauer spectra for Resovist is shown in Fig. 1. The spectra obtained at the lowest temperature of 2.6 K were fitted with Mössbauer parameters of maghemite (γ-Fe_2O_3) and the parameters well coincide with those of maghemite [5]. For Mössbauer spectra at temperatures below 50 K, the same fitting procedure as that of 2.6 K was

---

[1] National Institute of Technology, Ibaraki College

adopted. At temperatures $T \leq 100$ K, MS shows a widely distributed magnetic sextet and small peak broadening at around zero velocity. Further increasing the temperatures increases the height of the center peak. The 1st and 6th absorption peaks of the magnetic sextet are unchanged, but the profile changes to an inward tail distribution of hyperfine field (H_{hf}). This is often characteristic of Fe atom relaxation.

Table 1. Mössbauer spectral parameters for Resovist between 150 and 250 K. The Mössbauer data were analyzed based on the Blume-Tjon two-level model for sub-spectra labeled by MR. Italic characters in the table show fixed fitting parameters. *IS** relative to α-Fe.

Temperature (K)	Sub-spectrum	H_{hf} (T)	*IS** (mm/s)	*LW* (mm/s)	R_{jump}	τ_{BT} (s)	Area ratio (%)
250	MR1	47.5	0.349	0.4	7.12	3.8×10^{-8}	21.1
	MR2	43.0	0.369	0.4	7.46	1.7×10^{-8}	15.6
	MR3	42.0	0.343	1.22	8.89	6.4×10^{-10}	63.3
200	MR1	49.1	0.383	0.5	6.48	3.0×10^{-8}	17.2
	MR2	45.2	0.358	0.5	7.34	2.2×10^{-8}	20.9
	MR3	45.0	0.396	1.31	8.79	6.1×10^{-10}	61.9
150	MR1	50.0	0.410	0.5	6.43	1.9×10^{-8}	21.7
	MR2	46.4	0.389	0.5	7.27	2.7×10^{-8}	21.9
	MR3	45.0	0.409	1.61	8.81	7.7×10^{-10}	56.4

The Mössbauer spectra recorded at 150, 200, and 250 K, show large center absorption. The fitting was performed assuming the BT model composed of three sub-spectra with two slow (MR1 and MR2) relaxation times and another fast relaxation (MR3) time. The subspectra with slow relaxation time (long time) show an ordinal magnetic sextet with broad linewidth (*LW*), where *LW* and jump rates (R_{jump}) were set to be identical assuming Fe atoms responsible for MR1 and MR2 belong to the same large particle. In contrast, the subspectrum with a fast relaxation time (short) shows a widely spread spectrum (Fig 1). Relaxation times (τ_{BT}) were deduced from the relation $\tau_{\mathrm{BT}} = 1 / (2\times10^{R_{\mathrm{jump}}})$. The relaxation times thus obtained monotonically decrease from 1.9×10^{-7} to 3×10^{-8} s for MR1 and MR2, respectively, whereas those for MR3 do not monotonically change and are scattered between $7.7 \times 10^{-10} - 3 \times 10^{-10}$ s. By fitting the central part of the spectra to the BT model relaxation sub-spectra, a short τ_{BT} and wide *LW* were obtained for a large H_{hf} around 40 T, whereas long τ_{BT} are represented by a small H_{hf} of less than 30 T. This may suggest an ambiguity in analyzing the center part. Fitting parameters are listed in Table 1. The values of isomer shifts (*IS*) suggest that Fe atoms are in the 3+ state.

The particle size distribution of Resovist has been reported previously [3]. Bimodal size distributions of 5.5 and 24 nm in mean diameter have been reported and, using $K = 10^4$ J/m^3, τ_{N} at 250 K is estimated to be 1.44×10^{-10} and 1.58×10^{-2} s for 5.5 and 24 nm, respectively.

References

[1] E. Kita et al., UTTAC Annual Report 2020, UTTAC-90 (2021) 36.

[2] E. Kita et al., to be published in IEEE Magn. Lett. 14 (2023).

[3] D. Eberbeck et al., Appl. Phys. Lett. 98 (2011) 182502.

[4] M. Blume and J. A. Tjon, Phys. Rev. 165 (1968) 446.

[5] G. M. Da Costa et al., Clays and Clay Minerals 42 (1994) 628.

4.3 Magnetic properties of hexagonal CoFe nitrides studied by Mössbauer spectroscopy

C. Kodaka, M. Kishimoto, T. Sekido, E. Kita, H. Yanagihara

Fe nitrides have been studied as magnetic materials consisting of common elements such as Fe and nitrogen. These Fe–N compounds exhibit various physical properties, such as mechanical strength and magnetism [1]. The magnetic properties of Fe–N systems, such as $Fe_{16}N_2$, Fe_4N and $Fe_{2\text{-}3}N$ have been studied well. The Fe–N compound with the lowest nitrogen concentration is $Fe_{16}N_2$, which has a body centered tetragonal (bct) structure. This compound has been extensively studied as a material with high saturation magnetization (M_s) [1], exceeding bcc-Fe, and high magnetic anisotropy at room temperature [2]. Compounds with nitrogen concentrations higher than $Fe_{16}N_2$ are Fe_4N and $Fe_{2\text{-}3}N$. $Fe_{2\text{-}3}N$ was realized in an hcp structure with high mechanical and chemical stabilities; however, for a magnetic material, their magnetic properties are not attractive. Fe-based alloy nitrides, for example $(FeNi)_4N$, have been also studied; however, the number of studies is limited because of the difficulty in their fabrication. Recently, an FeNi nitride, (FeNi)N, was utilized as a precursor of $L1_0$-FeNi ordered compounds, which show significantly high uniaxial magnetic anisotropy [3, 4] demonstrating a new application of Fe-based nitrides. Theoretical calculations have predicted that FeCo alloy nitrides have a high crystalline magnetic anisotropy [5]. To investigate magnetic property, such as magnetic transition temperatures and magnetic moments, Mössbauer spectroscopy (MS) for $(FeCo)_{2\text{-}3}N$ was performed at various temperatures [6, 7].

Three $(FeCo)_xN$ compounds with $x = 2.25$, 2.35, and 2.48 were prepared by nitriding FeCo alloy particles in an ammonia gas furnace. At first, FeCo fine hydroxide particles were produced with a co-precipitation technique using Fe and Co chlorides. A nominal atomic ratio of Fe and Co was set to 1:1. The particles were spherical, with volume-weighted average diameter of approximately 40 nm for FeCo and 70 nm for (FeCo)N. The crystal structures of the FeCo nitrides were analyzed by XRD [7]. The Rietveld analysis indicates that $(FeCo)_{2.48}N$ is in an hcp single phase, although the R factor is not sufficiently small. The other samples were assigned to be the ε-phase. Note that neither the γ phase nor any other phase appeared in this experiment.

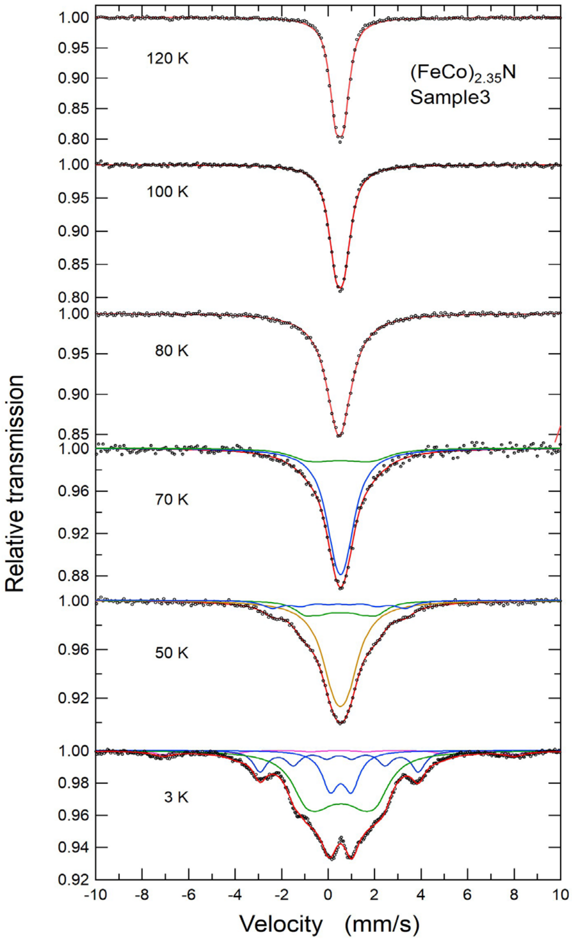

Fig. 1. Temperature dependence of Mössbauer spectra for $(FeCo)_{2.35}N$.

MS was performed between room temperature and 3 K. To achieve low sample temperatures, a closed cycle refrigerator cryostat was used. The velocity was calibrated using the α-Fe spectra at room temperature [6, 7].

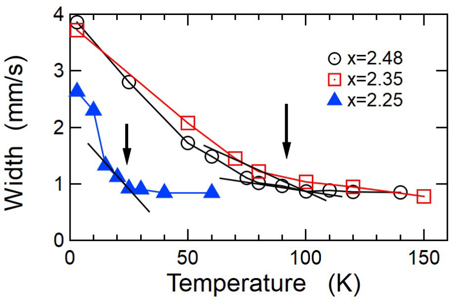

Fig. 2. Temperature dependence of the width of Mössbauer spectra for x = 2.25, 2.35 and 2.48 [7].

Figure 1 shows the temperature dependence of the Mössbauer spectra of the (FeCo)$_{2.35}$N particles. The spectra below 50 K appear to be composed of two major magnetic sextets. Above 70 K, it is not easy to separate into sextets. Therefore, the width of the spectrum is defined as the full width at half maximum in the velocity range. The widths thus obtained are plotted in Fig. 2. The widths for the samples with x = 2.48 and 2.35 decrease at approximately 90 K. However, when x = 2.25, the hyperfine field was small and decreased rapidly with increase in temperature, and the estimated magnetic transition temperature (T_C) was approximately 25 K. These coincide well with T_C determined by the magnetic measurements at 103, 95, and 23 K for x = 2.48, 2.35, and 2.25, respectively [7]. The room-temperature MS for (FeCo)$_x$N shows paramagnetic spectra, and no magnetic subspectra was observed (see Fig. 3). It is reasonable that magnetization measurements revealed almost paramagnetic states at room temperature.

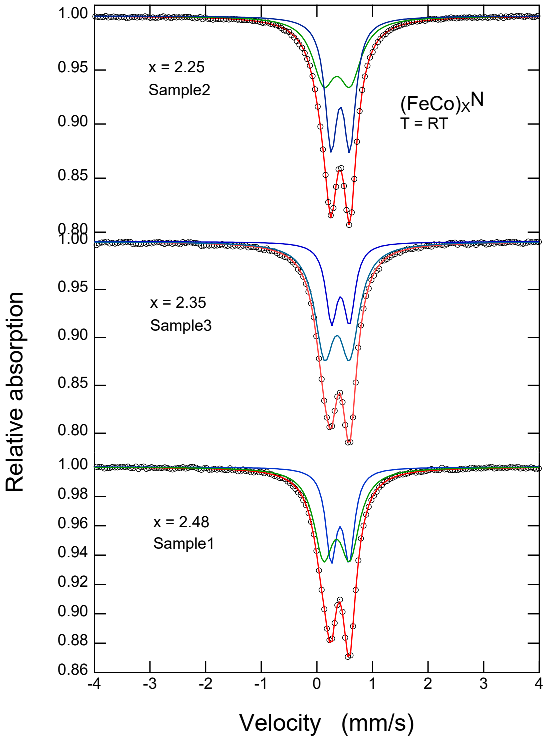

Fig. 3. Mössbauer spectra at room temperature.

From the MS and magnetization measurements, the compounds are ordinally ferromagnetic for x ≥ 2.35. However, for x = 2.25, more complex magnetic ordering is suggested by a magnetization measurement [7]. Griffith's Phase (GP) may exist, which originates from co-existence of anti-ferromagnetic and ferromagnetic couplings between magnetic atoms.

References

[1] J. M. D. Coey, P. A. I. Smith, J. Magn. Magn. Mater. 200 (1999) 405.

[2] E. Kita et al., J. Magn. Magn. Mater. 310 (2007) 2411.

[3] S. Goto et al., Sci. Reports 7 (2017) 13216.

[4] S. Goto et al., ACS Appl. NANO Mater. 2 (2019) 6909.

[5] W. Wang et al., Appl. Phys. Lett. 117 (2020) 122408.

[6] C. Kodaka et al., UTTAC Annual Report 2021, UTTAC-91 (2022) 31.

[7] C. Kodaka et al., IEEE Magn. Lett. 14 (2023) 2500105.

4.4 Transmission ERDA of ubiquitous deuterium in H-containing materials

H. Kudo, H. Naramoto, M. Sataka, S. Ishii, K. Sasa, S. Tomita

Elastic recoil detection analysis of transmission layout (T-ERDA) is useful for quantitative analysis of hydrogen in solids mainly because of its one-dimensional setup which simplifies the analysis of experimental data [1]. To investigate further applicability of T-ERDA, we have measured deuterium (D) in H-containing materials. Notably, the ratio of D to H content (so-called D/H ratio) in a solid sample seems to be a very similar fraction on the order of 10^{-4} of hydrogen wherever hydrogen is found on the earth. The D/H ratio is changeable, for example, it increases if there are natural or artificial processes at work that concentrate it, for example, distillation (because of higher boiling point of D-water than that of H-water) or electrolysis of water. The geological and cosmological importance of deuteron analysis has been understood since the early period of the related research [2].

The experimental setup is similar to that described previously [1]. By using an incident beam of 8 MeV He^{2+} from the UTTAC 6MV tandem accelerator, the measurements were carried out under the pressure of 2×10^{-5} Pa. The beam was focused typically to $\sim 0.1 \times 0.1$ mm^2 on the samples. The samples used in the present experiments are thin H-containing films of mylar (polyethylene terephthalate, $(C_{10}H_8O_4)_n$) of 2.5 μm thickness, and PPS (polyphenylene sulfide, $(C_6H_4S)_n$) of 1.35 μm thickness. These films were underlaid with a Ni foil of 20 μm thickness to prevent the incident He from entering the particle detector.

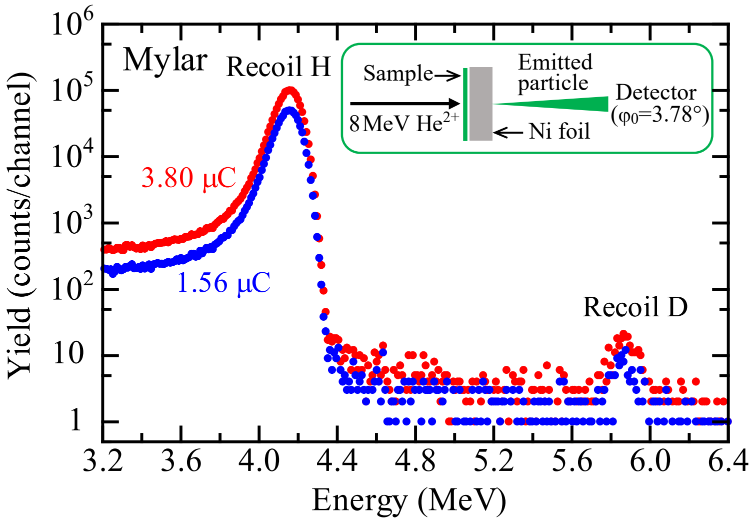

Fig. 1. T-ERDA spectra for incidence of 8 MeV He^{2+} on the mylar film of 2.5 μm thickness, which were measured for the incident charges of 1.56 and 3.80 μC. On the horizontal axis, 10.88 keV corresponds to 1 channel width. The inset schematically shows the experimental setup.

Figure 1 shows T-ERDA spectra of the mylar/Ni(20 μm) sample, measured for the incident He^{2+} charges of 1.56 and 3.80 μC. From the estimate employing the stopping powers by SRIM, the two peaks at 4.16 and 5.87 MeV are identified as recoil H and D from the mylar film, respectively. From the T-ERDA spectra, D and H yields are obtained by counting the areas under the peaks after subtracting the discernible background yield in Fig. 1. The background subtraction has been carried out by assuming the straight baseline connecting the ends of low- and high-energy tails of the peak, which are clearly recognized in every spectrum plotted in the linear scale.

Figure 2 shows the ratio of D to H yield plotted against the incident He^{2+} charge on mylar during the measurements. The ratio increases with increasing the incident charge because the radiation-induced loss of H is more than that of D. The ratio of interest in the present case R_0 is given by the ratio at zero incident charge, corresponding to the intersection point of the dashed line and the vertical axis in Fig. 2. In this manner, we have obtained $R_0 = (1.05 \pm 0.05) \times 10^{-4}$ and $(1.08 \pm 0.05) \times 10^{-4}$ for mylar and PPS, respectively.

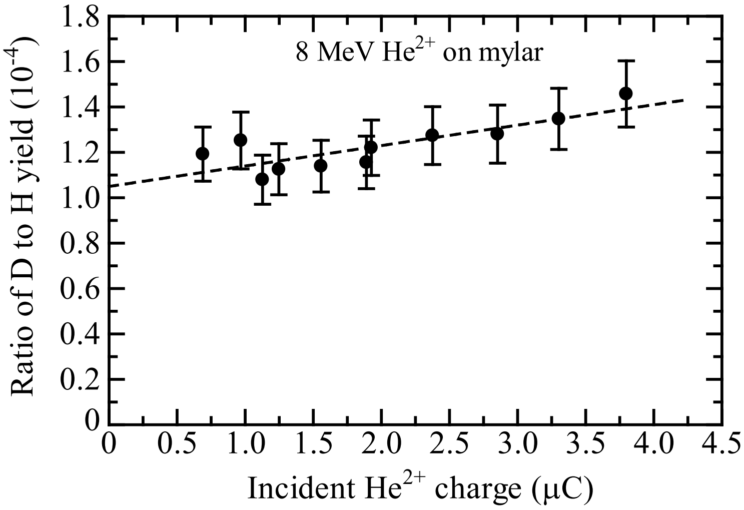

Fig. 2. Dependence of the ratio of D to H yield on the incident He^{2+} charge on mylar during the measurements. The dashed line shows the least-square linear fit to the plots. The D/H ratio of interest $R_0 = (1.05 \pm 0.05) \times 10^{-4}$ is given at zero incident charge on the dashed line.

The D/H ratio is given by

$$(\mathrm{D/H\,ratio}) = R_0 \times \frac{\sigma_\mathrm{H}}{\sigma_\mathrm{D}}\,, \tag{1}$$

where σ_H and σ_D are the recoil cross sections in the laboratory system for H and D, respectively, which are given by integrating the differential recoil cross sections $d\sigma/d\Omega$ over the solid acceptance angle of the detector. According to the existing experimental data, the most suitable values of $\sigma_\mathrm{H}/\sigma_\mathrm{D}$ are (1.48+1.66)/2=1.57 and (1.48+1.56)/2=1.52 for mylar and PPS, respectively. The values of D/H obtained from Eq. (1) are $(1.65 \pm 0.08) \times 10^{-4}$ and $(1.64 \pm 0.08) \times 10^{-4}$ for mylar and PPS, respectively. These values are only slightly higher than the Standard Mean Ocean Water (V-SMOW) value of $(1.5576 \pm 0.0010) \times 10^{-4}$ [3], indicating ubiquitous deuterium in H-containing materials. The present work demonstrates the wide applicability of T-ERDA to non-destructive analysis of trace D in solids.

References

[1] H. Kudo et al., J. Phys.: Condens. Matter 34 (2022) 435902.

[2] I. Friedman, Geochim. Cosmochim. Acta 4 (1953) 89.

[3] J. C. De Wit et al., Geostand Geoanal Res 4 (1980) 33.

4.5 Tracking ^{7}Li in all-solid-state batteries using NRA

N. Kishi, S. Kobayashi[1], Y. Sugisawa, R. Shimizu[1], T. Hitosugi[1, 2], D. Sekiba

All-solid-state Li-ion batteries, which can safely increase the capacity of Li-ion batteries, have attracted considerable attention. At present, the problem of insufficient conductivity for practical use remains. In this study, in order to elucidate the cause of this problem, we attempted to observe the behavior of ^{7}Li using ^{7}Li (p, α) ^{4}He nuclear reaction analysis (NRA).

NRA was performed using a 1.5 MeV H^+ beam from 1MV Tandetron at UTTAC. The detector was mounted at 150° with respect to the beam direction, and the sample was tilted so that α particles can be detected at 70° from the surface normal. The sample consists of stacked layers of $Li/Li_3PO_4/$ $LiCoO_2/Au$ deposited on a Si_3N_4 substrate which is a 4.0×7.6 mm^2 film with a thickness of 1 μm. The H^+ beam was incident on the substrate side. A power supply for the bias voltage and an ammeter were connected to the sample in vacuum via a feedthrough. After the as-deposited sample was charged by applying the bias voltage of 4.3 V, it was discharged by reducing the bias voltage to 3.0 V. Then, the sample was recharged by increasing the bias voltage to 4.3 V. In these processes, we observed the behavior of ^{7}Li when the battery was discharged by comparing the NRA spectra for the 4.3 V charging and the 3.0 V discharging. Similarly, the behavior of ^{7}Li was observed when the battery was recharged by comparing the NRA spectra for the 3.0 V discharging and the 4.3 V recharging.

Figure 1(a) shows the NRA spectra measured for the sample when it was charged and discharged afterwards, shown in blue and orange, respectively. Figure 1(b) shows the yield difference, i.e., the “orange – blue” yield, from which we can see the change in the ^{7}Li profile caused by discharging. Indeed, negative peaks are seen in the energy ranges indicated by a, c, and e which correspond to the layers in the sample shown in Fig. 1, while positive peaks are seen in the layers b, d, and f. Figure 2(a) shows the NRA spectra when the sample was discharged and recharged, shown in orange and green, respectively. Figure 2(b) shows the yield difference, i.e., the “green – orange” yield, from which we can see the change in the ^{7}Li profile caused by recharging. On the negative electrode side, ^{7}Li decreases in the layers a and a’, while ^{7}Li increases in the layers b and b’. This implies that ^{7}Li flows from the negative electrode into the solid electrolyte, regardless of the battery state, probably because of intrinsic migration.

In Fig. 1(b), the amount of increase in ^{7}Li in the layer d seems the same as that of decrease in the layer c, hence we may assume that ^{7}Li in the layer c moves to the layer d. Similarly, we may assume that ^{7}Li in the layer e moves to the layer f. According to the above assumption, ^{7}Li diffuses from the electrolyte to the positive electrode like billiard balls when the sample is discharged. In Fig. 2(b), ^{7}Li moves from the layer e to the layer d, and the layer d to the layer c, as if reproducing the profile seen in Fig. 1(b), thus we consider that ^{7}Li moves from the layer e to d to c. On the other hand, ^{7}Li in the layer f seems to move to the layer c, which does not seem to reproduce the profile seen in Fig. 1(b). To investigate the cause of this result, we will use a target with a deposited ^{6}Li-enriched layer in future.

---

[1] Tokyo Institute of Technology
[2] The University of Tokyo

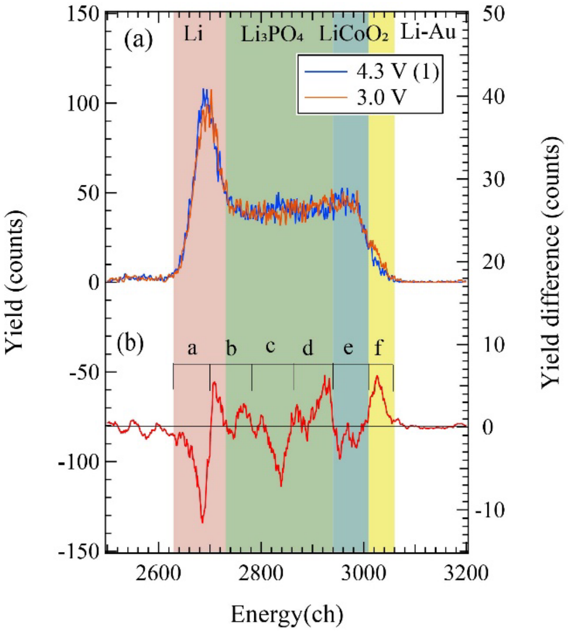

Fig. 1. (a) NRA spectra measured for the sample when it was charged and discharged afterwards, shown in blue and orange, respectively. (b) The yield difference between the two spectra.

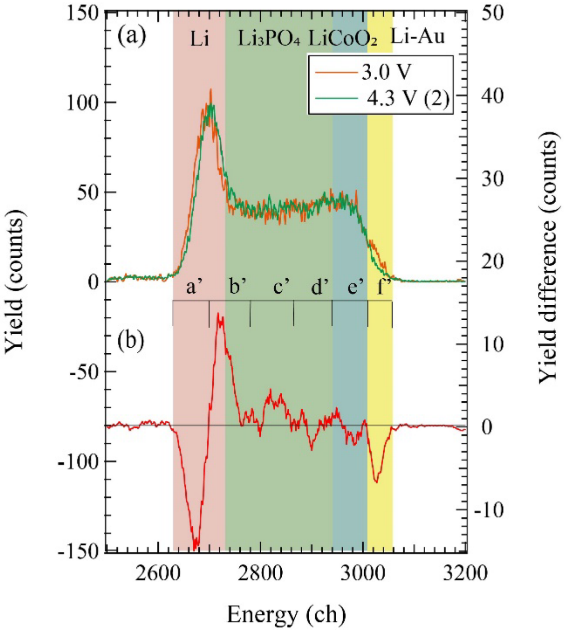

Fig. 2. (a) NRA spectra measured for the sample when it was discharged and recharged afterwards, shown in orange and green, respectively. (b) The yield difference between the two spectra.

Reference

[1] N. Kishi et al., UTTAC Annual Report 2021, UTTAC-91 (2022) 34.

4.6 Electrochemical route to quickly insulate photo-metalized YO_xH_y(111) epitaxial thin films

Y. Komatsu[1], Y. Sugisawa, N. Kishi, T. Hitosugi[2], D. Sekiba, R. Shimizu[1]

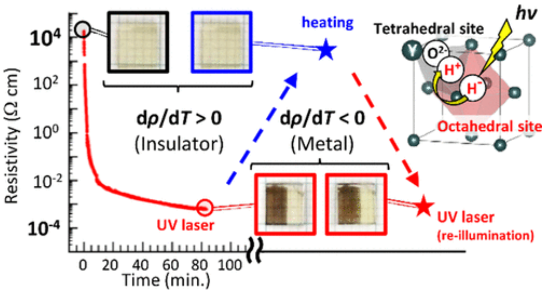

Fig. 1. Schematic illustration of photo-induced metallization in YO_xH_y (111) epitaxial thin films [2].

Yttrium oxyhydrides (YO_xH_y) have attracted considerable attention due to their photochromic properties for optoelectronics applications such as smart windows and photo sensors [1]. Recently, our group reported repeatable photo-induced metal-insulator transition in YO_xH_y (111) epitaxial thin films [2]. This photo-metalized state is retained within a few days (>10^5 sec) at room temperature (memory effect). To accelerate the recovery to the original transparent and insulating state within a few hours (~10^3 sec), the annealing is necessary at around 100°C. The mechanism of the metallization/insulation processes is correlated with the internal migration of hydrogen ions and/or atoms. Electrochemical methods provide a route to promote internal hydrogen migration. For example, the insertion/desertion of interstitial H^+ causes metal/insulator switching in WO_3 and VO_2 (electrochromism) within ten seconds [3]. Accordingly, it is expected that a similarly quick recovery to the original transparent and insulating states can be electrochemically performed in YO_xH_y.

Here, we investigated the electrochemical responses of photo-metalized YO_xH_y. We found the potential application of 0.0 V (vs. Ag/AgCl) (+0.57 V vs. reversible hydrogen electrode (RHE)) in 0.1 M NaCl solution insulates the photo-metalized YO_xH_y within ~5 sec. This speed is 4 orders of magnitude quicker than the conventional thermal relaxation processes (>10^5 sec). Surprisingly, the insulated film can be metalized again by UV laser illumination, and this photo-metallization and electrochemical insulation can be performed ten times at least. Using ion beam analyses such as nuclear reaction analysis (NRA), elastic recoil detection analysis (ERDA), and Rutherford backscattering spectroscopy, we found that photo-generated H is deserted from the film during the electrochemical insulating processes.

YO_xH_y (111) epitaxial thin films were deposited on yttria-stabilized zirconia (YSZ) (111) and CaF_2 (111) substrates using reactive magnetron sputtering. YH_y precursor films were deposited with a mixture of argon and hydrogen gas introduced into the deposition chamber, and the substrate temperature was set to 150°C. After the deposition, the as-grown film was exposed at room temperature to oxygen gas at 1 atm to fully oxidize the films. To characterize H contents in films, we performed secondary ion mass spectrometry (SIMS) and ion beam analyses. ERDA measurements were performed at UTTAC.

Figure 2 shows the results of electrochemical processes on photo-metalized YO_xH_y. While only the H_2 evolution reaction occurs under the potential application of –4 V (vs. Ag/AgCl), we observed oxidation current at ~ –0.6 V (vs. Ag/AgCl), leading to the insulation of the thin films (Fig. 2(a)). This process was

---

[1] Tokyo Institute of Technology
[2] The University of Tokyo

completed within 10 sec (Fig. 2(b)), 4 orders quicker than the conventional thermal relaxation.

These processes are repeatedly operated. Figure 2(b) shows the electrical resistance change in the steps of metallization (UV illumination) and insulation (+0.0 V application in NaCl solution). Note that the potential of +0.0 V vs. Ag/AgCl corresponds to +0.57 V (vs. RHE), which does not exceed the ideal O_2 evolution potential (+1.23 V vs. RHE). Thus, we achieved repeatable resistance switching 10 times at least.

To understand the electrochemical insulation mechanism, we evaluated the H content in the thin films. Figure 3(a) shows the depth profiles obtained by SIMS after the potential application of +0.0 V vs. Ag/AgCl, indicating that the H content in the films gradually decreases. Namely, photo-induced H^+, which generates electron carriers in the thin films, is released into the solution. Accordingly, the desertion of H^+ carrier electrons leads to transparent and insulating states. Deserted H atoms are again inserted into the YO_xH_y thin films by the negative potential application of –5.0 V (vs. Ag/AgCl). Figure 4(a) shows the result of resistance change, indicating metallization also electrochemically occurs. Using ERDA, Fig. 4(b) clarifies the existence of D in the films after the electrochemical treatment. These results indicate that the insertion/desertion of H/D plays a critical role in the drastic change in the optical and electrical properties of YO_xH_y.

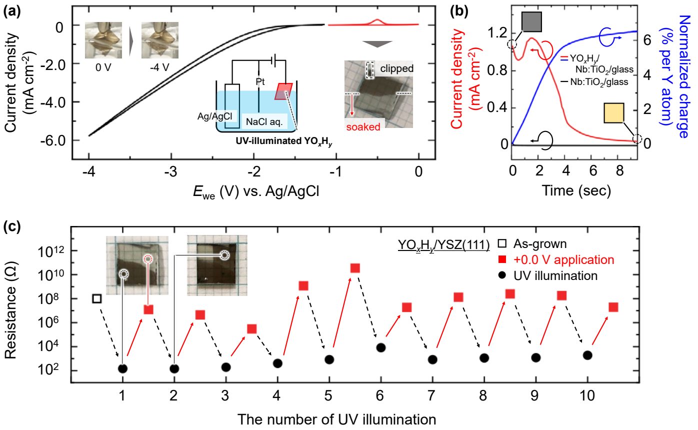

Fig. 2. (a) Cyclic voltammogram at the potential of –4 V to +0 V (vs. Ag/AgCl). (b): Temporal change of current density (red) and normalized charge per Y atom (blue) at +0.0 V (vs. Ag/AgCl). (c): Resistance change in the repeated steps of UV illumination and electrochemical insulation.

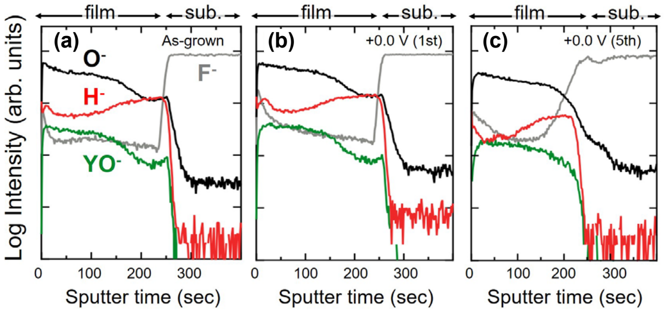

Fig. 3. Depth profiles obtained by SIMS (a: as-grown, b: 1st +0.0 V vs. Ag/AgCl application, c: 5th +0.0 V vs. Ag/AgCl application). H^- ions decreased in (c).

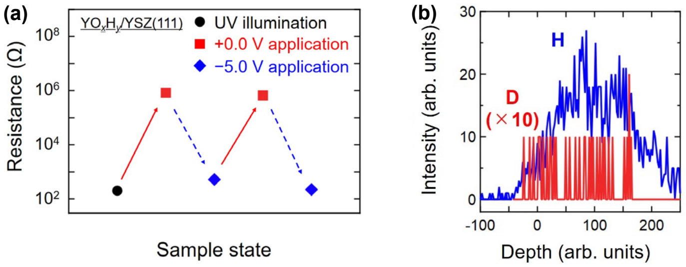

Fig. 4. (a) Resistance switching only by electrochemical processes. (b) ERDA results of $YO_xH_yD_\delta$ after negative potential application of –5.0 V vs. Ag/AgCl treated in 0.1 M NaCl in D_2O solution. D signal from the D_2O solution is observed.

References

[1] T. Mongstad et al., Sol. Energy Mater. Sol. Cells 95 (2011) 3596.
[2] Y. Komatsu et al., Chem. Mater. 34 (2022) 3616.
[3] J. Y. Zheng et al., Nanoscale 15 (2023) 63.

4.7 Study for hydrogen content for UCN storage

K. Mishima[1], S. Kawasaki[1], N. Kishi, D. Sekiba, K. Yamamoto

Ultracold neutrons (UCNs) are extremely slow neutrons with energies below ~300 neV and totally reflected on material surfaces due to their long wavelength. UCNs are very interesting probes for fundamental physics because they can be stored in a vessel and manipulated. The TRIUMF Ultra-Cold Advanced Neutron (TUCAN) collaboration aims at a precision neutron electric dipole moment (nEDM) measurement with an uncertainty of 10^{-27} $e\cdot$cm, which is an order of magnitude better than the current nEDM upper limit and enables us to test new physics [1].

For UCN transport, Nickel-phosphorus (NiP) plating, which is inexpensive and easy to process, is often used. UCN is totally reflective on the surface, but a very little, about 10^{-4}–10^{-5} per reflection, is absorbed. It is known that the absorption has a large variation depending on the fabrication process and the surface conditions [2]. This is suspected to be caused by impurities on the NiP surface, especially hydrogen, which has a large incoherent scattering cross section and causes the disappearance of UCN by up-scattering. For that investigation, we measured some NiP plated samples with Elastic Recoil Detection Analysis (ERDA) to determine the hydrogen concentration on NiP surfaces. The phosphorous concentration in NiP is also important to determine the reflection critical potential at the surface. This was determined by Rutherford Backscattering Spectrometry (RBS). The experimental setup is shown in Fig. 1. The sample was irradiated with 2.5 MeV ^{4}He^{2+} incident from the left in Fig. 1, and backscattered He for RBS and recoil H for ERDA were measured using the backward and forward detectors (SSD), respectively.

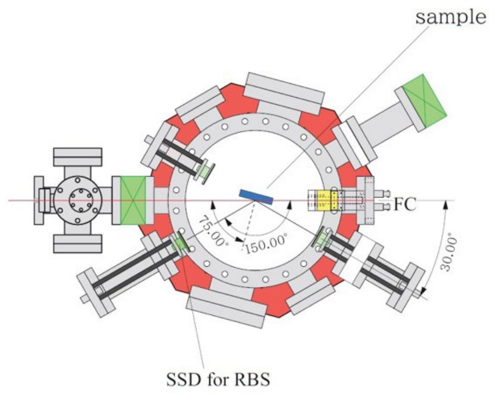

Fig. 1. The RBS and ERDA setup. The He ion beam is incident from the left.

Four NiP samples were measured in this study. Two of the samples were cut from the ϕ90 mm cylindrical UCN guide tubes actually used in the TUCAN experiment and plated with NiP on the inner surface; the NiP roughness was measured at the commonly used R_a = 50 nm and at R_a = 800 nm, which is before polishing. The other two were NiP plated on flat Al surfaces and each polished to reach R_a = 1 nm and 2 nm.

The RBS spectra are shown in Fig. 2 (left). The peak due to P is observed at 350 channel. For the UCN guide sample (50-nm R_a), the P content is estimated as 20 atom%. This corresponds to 12 weight% and is consistent with the designed value [2]. The samples on flat Als (1- and 2-nm R_a) have relatively low P content.

The ERDA spectra show hydrogen content from the surface to the effective depth of 100 nm (Fig. 2 right). Based on the yield of Ni in the RBS spectrum, the hydrogen contents were estimated to be 15–16 atom% for the UCN guide samples (50- and 800-nm R_a) and 2–3 atom% for the flat samples. These results

---

[1] High Energy Accelerator Research Organization (KEK)

are considered to be due to the moisture attached to the surface. At depths greater than 100 nm, the H contents were 1.2% for 800-nm R_a, and 0.6% for the others, indicating that the hydrogen contamination except the surface could be kept small.

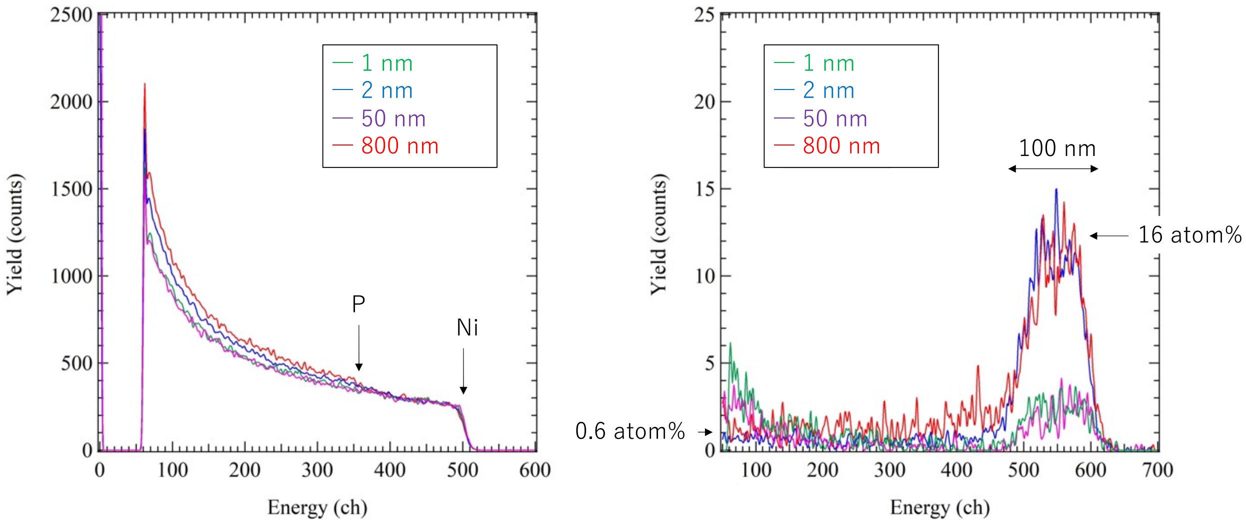

Fig. 2. The RBS (left) and ERDA (right) spectra for the NiP samples with different roughness.

References

[1] R. Matsumiya et al., Proc. 24th International Spin Symposium (SPIN2021), JPS Conf. Proc. 37 (2022) 020701.

[2] H. Akatsuka et al., Nucl. Instr. Meth. Phys. Res. A 1049 (2023) 168106.

5.

ION-BEAM IRRADIATION EFFECT

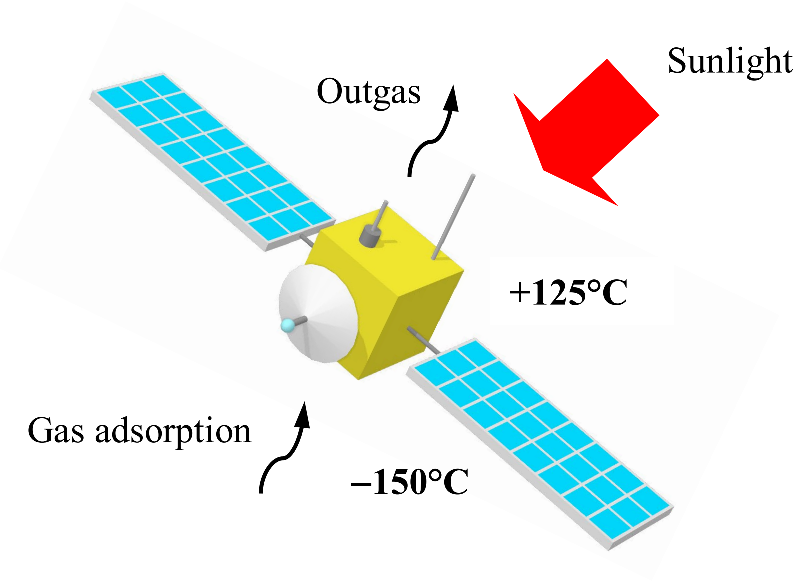

Space environment experienced by a satellite (adapted from a material in the web page of NDK, using a free-use illustration).

—— *Report 5.2*

5.1 Evaluation of LoRa$^{\text{TM}}$ transceiver and microprocessor toward space use

T. Kameda, Y. Kurihara, H. Yoshikado

When semiconductor components are used in space, the effects of space radiation must be considered for stable operation [1]. In particular, heavy ions in cosmic rays can cause SEE (Single Event Effect), which can lead to temporary malfunction (soft error) or permanent failure (hard error) of semiconductors and interfere with spacecraft operations. Therefore, a detailed investigation is required in advance [2].

We focused on LoRa$^{\text{TM}}$ modulation for space applications because of its high interference tolerance over very long distances and low current consumption. From this perspective, among the commercially available products, Murata's CMWX1ZZABZ (SX1276) the LoRa$^{\text{TM}}$ transceiver on the Arduino MKRWAN 1310 board has been chosen, and its feasibility of the space applications was investigated.

In addition, since the microcontroller device is required for data handling with the transceiver, radiation exposure tests were conducted to verify the feasibility of use in space for the STM32F401 that is an Arm-based microcontroller mounted on the Nucleo-32 development board, and the CXD5602 that is a chip mounted on the Sony board computer, SPRESENSE$^{\text{TM}}$.

The test samples of de-capped STM32F401, CMWX1ZZABZ, and CXD5602 were irradiated with 48 MeV F^{7+} and 48 MeV Cl^{7+} from the 6MV tandem accelerator at UTTAC. The arrangement of each device is shown in Fig. 1. The number 0, 1, and 2 in Fig. 1 show STM32F401 on the Nucleo-32 development board, CMWX1ZZABZ on the Arduino MKRWAN 1310, and CXD5602 on the SPRESENSE, respectively. We observed the incidence of (i) bit flips associated with soft errors for microprocessors, (ii) the data changes between transmission and reception and the mode changes for LoRa$^{\text{TM}}$ transceivers, and (iii) the increase in power consumption associated with hard errors to determine the occurrence of SEU (Single Event Upset) and SEL (Single Event Latch-up) during irradiation with changing the number of particles.

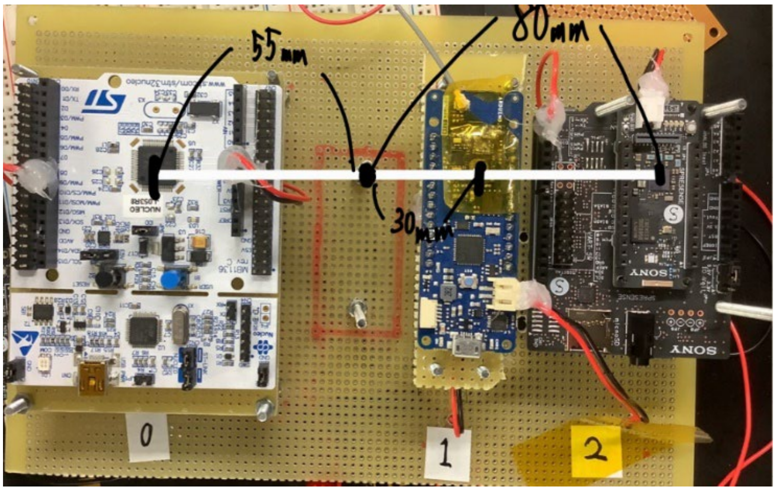

Fig. 1. Specimen configuration for the irradiation tests.

The bit flips of the memory in the microprocessors are monitored as follows: the 96 KB SRAM of the STM32F401 and the 1.5 MB SRAM of the CXD5602 were filled with the char type "U" (0x55, 0b01010101) in the unused memory area, and checked every 10000 ms (±1%) to monitor SEL, and electric current was logged every 500 ms.

Table 1 summarizes the experimental results: for the first irradiation of STM32F401 (when the number of Cl was 1463 particles/sec), no SEE was observed based on the electric current. However, during the next irradiation of 2138 particles/sec, about 500~700mA electric current was observed, whereas the usual current is 60~70 mA. After cutting off the irradiation by the shutter and restarted the semiconductors, normal current values were observed, and once the shutter was raised, the overcurrent was observed again. We checked the log of the contents of SRAM memory with reducing the number of particles, we could not confirm the occurrence of SEU as long as the system operated even when the current value was increased.

In CMWX1ZZABZ, a SEL of about 30 mA was generated each time after the second irradiation. After the second irradiation, the device switched to the reception mode from the initial transmission mode, also switched to the transmission mode from the initial reception mode. From these observations alone, it is not clear at this point whether this is caused by SEU or not. In order to clarify the cause of this phenomena, it is necessary to monitor this behavior by periodically dumping the registers of this module, for example.

No SEL was observed for CXD5602 at any particle number. The SEU has not been tested because of unexpected serial communication device trouble other than SPRESENSE.

In conclusion, STM32F401 cannot withstand cosmic radiation at the level of LET 17.3 MeV/(mg/cm^2), and the lower limit of the radiation resistance is unknown. The CMWX1ZZABZ showed SELs and operation problems such as mode switching, hence further investigation is necessary for quantitative evaluation toward space use. The CXD5602 seems to have sufficient radiation tolerance since no SELs were observed. We would like to verify SEU in the next test by resolving equipment problems.

Table 1. Irradiation results.

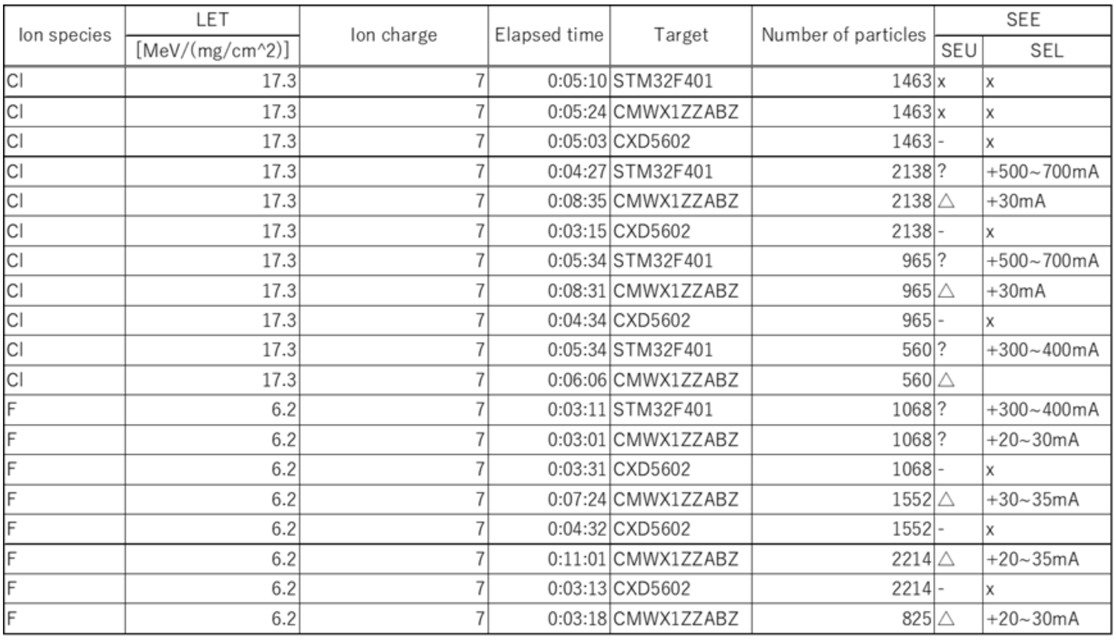

Ion species	LET	Ion charge	Elapsed time	Target	Number of particles	SEE	
	[MeV/(mg/cm^2)]					SEU	SEL
Cl	17.3	7	0:05:10	STM32F401	1463	x	x
Cl	17.3	7	0:05:24	CMWX1ZZABZ	1463	x	x
Cl	17.3	7	0:05:03	CXD5602	1463	-	x
Cl	17.3	7	0:04:27	STM32F401	2138	?	+500~700mA
Cl	17.3	7	0:08:35	CMWX1ZZABZ	2138	△	+30mA
Cl	17.3	7	0:03:15	CXD5602	2138	-	x
Cl	17.3	7	0:05:34	STM32F401	965	?	+500~700mA
Cl	17.3	7	0:08:31	CMWX1ZZABZ	965	△	+30mA
Cl	17.3	7	0:04:34	CXD5602	965	-	x
Cl	17.3	7	0:05:34	STM32F401	560	?	+300~400mA
Cl	17.3	7	0:06:06	CMWX1ZZABZ	560	△	
F	6.2	7	0:03:11	STM32F401	1068	?	+300~400mA
F	6.2	7	0:03:01	CMWX1ZZABZ	1068	?	+20~30mA
F	6.2	7	0:03:31	CXD5602	1068	-	x
F	6.2	7	0:07:24	CMWX1ZZABZ	1552	△	+30~35mA
F	6.2	7	0:04:32	CXD5602	1552	-	x
F	6.2	7	0:11:01	CMWX1ZZABZ	2214	△	+20~35mA
F	6.2	7	0:03:13	CXD5602	2214	-	x
F	6.2	7	0:03:18	CMWX1ZZABZ	825	△	+20~30mA

References

[1] T. Kameda et al., Aerospace 9(6) (2022) 280.

[2] Y. Chiba et al., JAEA-Review 2013-057 (2013) 73.

5.2 Evaluation of COTS electronic devices for space applications

H. Kukita[1], E. Miyazaki[2], T. Shiobara[1], T. Kimura[1]

The Japan Aerospace Exploration Agency (JAXA) and Nihon Dempa Kogyo Co., Ltd. (NDK) developed a compact, power-saving, Twin-QCM outgas sensor system for general-industry application. This system was commercialized by NDK for evaluation of materials used in space [1, 2]. We are now jointly researching and developing a system suitable for embedded use, which is also expected to be used in the space environment. In order to judge whether COTS (Commercial Off-The-Shelf) grade electronic components selected in the development process can be used for space applications, we evaluated the performance of radiation-resistance of BBM (Bread Board Model), using the 6MV tandem accelerator at UTTAC. A COTS grade SoC-FPGA (System on a Chip Field-Programmable Gate Array) mounted on a circuit board was irradiated with proton and heavy ion (oxygen) beams to test the single event effect.

Test results (February 2023)

Beam irradiation tests with 12 MeV H^+ and 54 MeV O^{8+} were conducted.

(1) Proton (12 MeV H^+) irradiation test results

Part type	Components	Material	Thickness [μm]	Energy after passing matter [MeV]	LET in Si [MeV/(mg/cm^2)]	Range in Si [μm]	Result
SoC-FPGA	Initial	-	-	12.00	-	-	SEL:none SEU:none
	material for derangement	Au	0.2	11.99	-	-	
	package	Epoxy	The package and passivation material were removed by decap for irradiation test.				
	passivation	Kapton					
	wiring layer	Al	*	*	-	-	
	wiring layer	Cu	*	*	-	-	
	sensitive layer	Si	*	11.76	0.031	941.16	
	substrate	Si	*	*	*	*	

*: non-disclosure

(2) Heavy ion (54 MeV O^{8+}) irradiation test results

Part type	Components	Material	Thickness [μm]	Energy after passing matter [MeV]	LET in Si [MeV/(mg/cm^2)]	Range in Si [μm]	Result
SoC-FPGA	Initial	-	-	54.00	-	-	SEL:none SEU: occurrence
	material for derangement	Au	0.2	53.25	-	-	
	package	Epoxy	The package and passivation material were removed by decap for irradiation test.				
	passivation	Kapton					
	wiring layer	Al	*	*	-	-	
	wiring layer	Cu	*	*	-	-	
	sensitive layer	Si	*	17.23	6.392	11.91	
	substrate	Si	*	0.00	0.000	0.00	

*: non-disclosure

---

[1] NIHON DEMPA KOGYO CO., LTD.

[2] Japan Aerospace Exploration Agency

In the irradiation tests with H^+ and O^{8+}, SEL (Single Event Latch-up) did not occur. On the other hand, in the O^{8+} irradiation of SoC-FPGA , which was equipped with an ECC (Error-Correcting Code) function, SEU (Single Event Upset) phenomenon occurred and resulted in a system freeze despite the enabled ECC function.

We concluded that implementation of ECC function is not enough for SoC-FPGA that is used in space environment, and radiation countermeasures such as implementation of SEM (Soft Error mitigation) function and TMR (Triple Modular Redundancy) are necessary. In the future, a radiation countermeasure function will be installed and its effectiveness will be investigated. Such tests will be conducted with varying irradiation conditions such as ion energies to evaluate error rates on the actual operation orbit, thereby a final judgment will be made.

References

[1] Outgas Analysis System (NDK)
https://www.ndk.com/en/products/outgas/
[2] Y. Tsuchiya et al., IEEE Sensors Journal 21 (2021) 10530.
https://ieeexplore.ieee.org/document/9351992

5.3 Observation of nonreciprocal critical current in $YBa_2Cu_3O_7$ films irradiated with 75-MeV Au ions directed off-normal to the film surface

H. Matsui[1], G. Nishijima[2], A. Matsumoto[2], I. Yamaguchi[1], T. Manabe[1], M. Sohma[1]

Asymmetry of critical current (I_c) in a superconductor with respect to the current direction (forward/backward) is called superconducting diode effect (SDE), and has attracted great interest for its potential application to superconducting electronics. To date, various SDEs have been reported for both low- and high-temperature superconductors (HTSCs) [1, 2]. However, only a few examples possess both of the following technological benefits that can be applied to produce a practical SDE: (1) HTSC and (2) out-of-plane magnetic fields (parallel to the c-axis in HTSCs, **B**//c). Two advantages of the latter benefit are easy alignment between a superconducting film and magnetic-fields and reduction of the device size including magnet(s).

In this work [3], we observed an SDE in YBCO films irradiated with 75-MeV-Au ions at 30°-off normal to the film surface. Up to 3% asymmetry of dc-transport I_c between opposite current directions was detected remarkably in **B**//c. The I_c asymmetry was observed only below 0.3 T, suggesting that it is a low-magnetic-field phenomenon. Moreover, the I_c asymmetry abruptly changed sign when the magnetic-field angle (θ) was rotated across the ion-incident angle (ϕ_i), clearly indicating a central role of the irradiation defects in the anomalous current property. Our results suggest that introduction of tilted 1D defects produces an unconventional SDE in YBCO films that functions in industrially advantageous **B**//c.

We deposited 1.0-μm-thick YBCO epitaxial films ($T_c = 90.8$ K) on CeO_2-buffered $SrTiO_3$ substrates by fluorine-free metal-organic deposition. The 75-MeV Au-ion irradiation was performed in a vacuum of 1×10^{-6} Torr at room temperature with a 6-MV tandem accelerator at University of Tsukuba. The specimens were fixed to a sample holder by electrically conductive adhesive tape to avoid electric charging by the irradiation. The incident angle of ions was set 30°-off normal to the film surface. Irradiation dose was set to 3×10^{10} cm^{-2} by controlling beam current and exposure time. In-magnetic-field I_c was measured at 77 K using a four-probe transport method in a temperature-controlled helium continuous-flow cryostat in the maximum Lorentz-force configuration. A 2 mm × 0.05 mm bridge normal to the tilting plane of the ion irradiation was fabricated by laser abrasion through a stencil mask.

Figure 1 shows a schematic that explains the geometry of ion irradiation and dc-transport measurements. The two angle parameters θ and ϕ_i are defined. Figure 2 shows the current-voltage characteristics of a 75-MeV-Au-irradiated YBCO film measured at 77 K and $\theta = 0°$ for different magnitudes of magnetic field (B). We observe a noticeable difference in I_c between the opposite current directions, i.e., larger I_c for positive current (black) than negative current (red, asterisk) in 0.1, 0.2, and 0.3 T. But this difference suddenly disappears at 0.4 T. By measuring the current-voltage characteristics at various θ (not shown), we observed that the sign of this I_c asymmetry, i.e., the polarity of SDE, was reversed by rotating θ across $\theta = \phi_i$. As we discussed in Ref. 3, these SDE properties are explained by nonreciprocal dynamic pinning of vortices

---

[1] National Institute of Advanced Industrial Science and Technology (AIST)

[2] National Institute for Materials Science (NIMS)

achieved in the coexistence of tilted 1D vortex-pinning-centers and significantly different vortex-pinning strengths between the film surface and film-substrate interface.

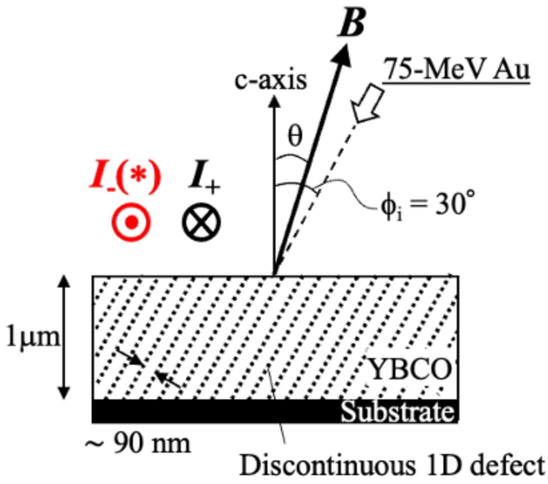

Fig. 1. Schematic explaining the geometry of ion irradiation and in-magnetic-field dc-transport measurements.

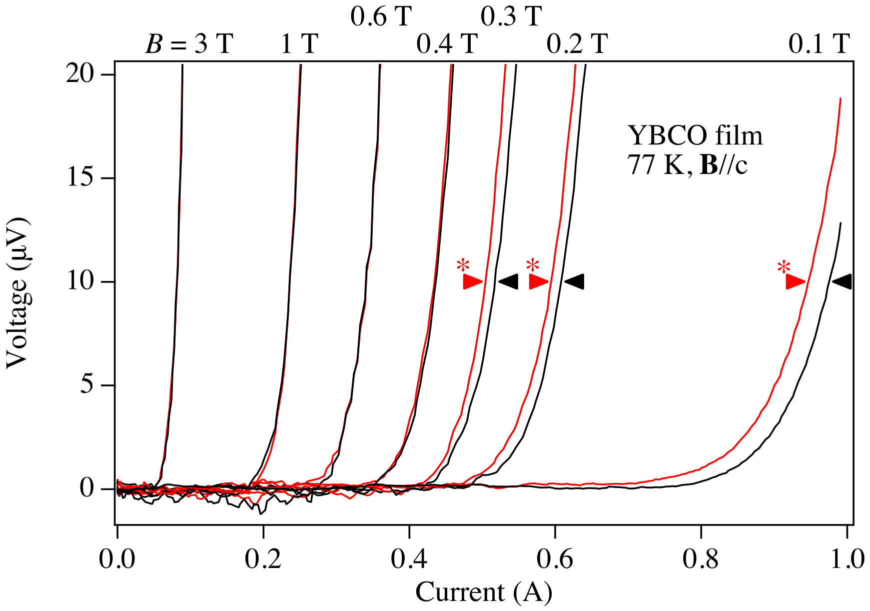

Fig. 2. Magnetic-field dependence of the current–voltage characteristics in a YBCO film irradiated with 75 MeV Au ions directed 30-off normal to the film surface. The measurements were performed at 77 K and **B**//c (θ = 0°) with positive current (black) and negative current (red, asterisk).

References

[1] A. Daido et al., Phys. Rev. Lett. 128 (2022) 037001.

[2] S. A. Harrington et al., Appl. Phys. Lett. 95 (2009) 022518.

[3] H. Matsui et al., Appl. Phys. Lett. 122 (2023) 172601.

5.4 Study on mutagenesis with ^{15}N-resonant nuclear reaction and radiation effects

I. Suzuki, T. Yang, T. Ikeda, S. Kubo, Y. Maeda, K. Sasa, S. Ishii, K. Tomita[1], H. Matsui, Y. Iwata[1]

Ionizing radiation is a typical exogenous source of the direct topological lesion of DNA molecules as well as the indirect influence arising from endogenous sources such as reactive oxygen species. Double-strand breaks or clustered DNA lesions have been one of the leading subjects of mutagenesis or carcinomatous genomic variation [1, 2]. An enormous number of studies on the DNA damage have elucidated the damage sensing, repairing, and tolerance pathways necessary for cells to survive [3]. However, since the direct topological DNA lesion induced by ionizing radiation has been commonly addressed as a single event independent of the response biofunction, it has been established to formularize the radiation effects of any kind of ionizing radiations with linear energy transfer, LET. In the report, the authors present DNA damages induced by the proton-capture nuclear reaction $^{15}\mathrm{N}(^{1}\mathrm{H}, \alpha_1\gamma)^{12}\mathrm{C}$ of the stable nitrogen isotope ^{15}N nuclei, which are inherent in DNA [4, 5]. The ^{15}N-DNA suffers both the radiation effects of the incident proton beam and the nuclear reaction products of $^{12}\mathrm{C}^{6+}$ and $^{4}\mathrm{He}^{2+}$ ions. Since both radiation effects spatiotemporally take place in a microscopically finite space of the DNA molecules, a possibility of nonlinearity can be expected in DNA damage.

Figure 1 shows pUC4-KIXX plasmid DNA possessing two kinds of resistance genes to the anti-biotics of kanamycin (R-kanamycin) and ampicillin (R-ampicillin). The genetic structure of the R-kanamycin and R-ampicillin resistance genes consists of 318 and 512 adenine-thymine base pairs (A-T bps) and the 477 and 454 guanine-cytosine base pairs (G-C bps), respectively. The *Escherichia coli* cells transformed with

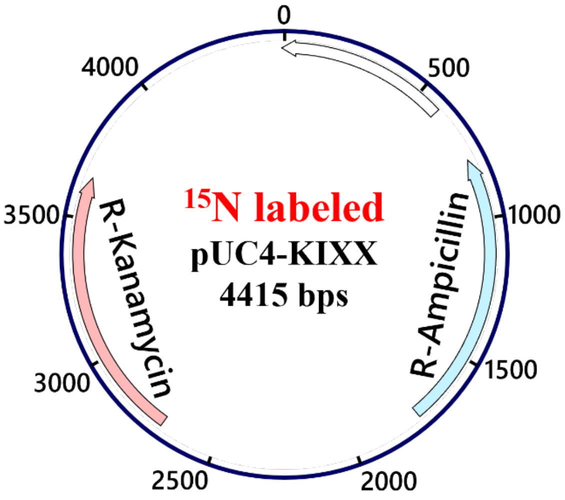

Fig. 1. Genetic structure of the ^{15}N labeled pUC4-KIXX plasmid possessing resistance genes of R-kanamycin and R-ampicillin to the anti-biotics. The isotope abundance of ^{15}N varied from the natural abundance ratio of 0.364 % to the maximum ratio higher than 98%.

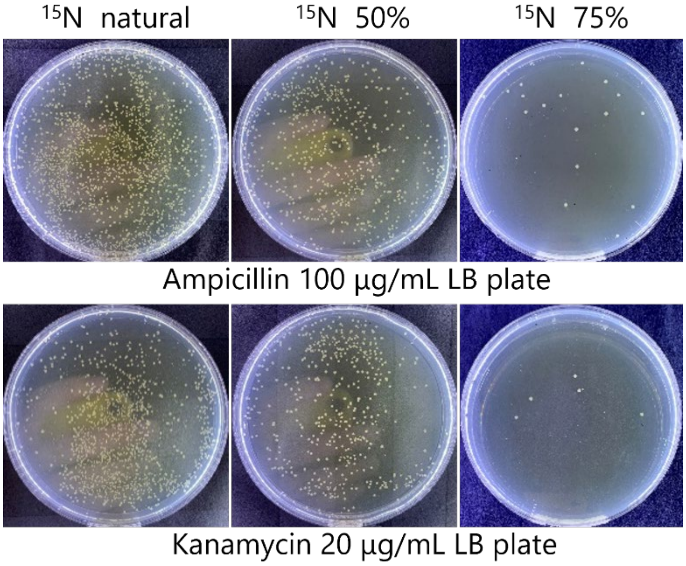

Fig. 2. Colony images of *Escherichia coli* transformed with the proton-irradiated ^{15}N-pUC4-KIXX plasmids, which suffered the radiation effects of the $^{15}\mathrm{N}(^{1}\mathrm{H}, \alpha_1\gamma)^{12}\mathrm{C}$ nuclear reaction depending on the isotope abundance of ^{15}N.

---

[1] National Institute of Advanced Industrial Science and Technology (AIST).

the pUC4-KIXX plasmid can be resistant to the anti-biotics of kanamycin and ampicillin.

^{15}N-pUC4-KIXX plasmids were prepared by substitution of constituent nitrogen atoms with the stable isotope of ^{15}N with the isotope abundance ratios [^{15}N] / [^{15}N + ^{14}N] from the natural abundance ratio of 0.364% to the maximum ratio higher than 98%. Proton beam irradiation to the ^{15}N-pUC4-KIXX plasmids was performed with the 1MV Tandetron accelerator at UTTAC. The proton energy was set at the resonance energy of the $^{15}N(^{1}H, \alpha_{1}\gamma)^{12}C$ nuclear reaction, and each plasmid target was irradiated with the proton dose of 0.2 μC. The *E. coli* cells transformed with the proton-irradiated ^{15}N-pUC4-KIXX plasmids grew in the two kinds of culture media, including kanamycin or ampicillin. If the resistance genes of R-kanamycin or R-ampicillin in the *E. coli* cells have not been damaged by proton beam irradiation, the *E. coli* cells can live in the culture media including anti-biotics of kanamycin or ampicillin to form a colony. The number of colonies obtained in both the culture media strongly depends on the isotope abundance ratios of ^{15}N as shown in Fig. 2. The ^{15}N-pUC4-KIXX plasmids with the natural abundance ratios of ^{15}N suffered the radiation effects of a proton beam dominantly. As the isotope abundance ratio of ^{15}N increases, the radiation effects of the $^{15}N(^{1}H, \alpha_{1}\gamma)^{12}C$ nuclear reaction, which follows proton beam irradiation, become evident. In the higher abundance ratios of ^{15}N than 75%, the number of colonies reduces to less than one-thousandth of the number of colonies in the natural abundance ratio.

In summary, the authors demonstrate in the report that the radiation effect of the $^{15}N(^{1}H, \alpha_{1}\gamma)^{12}C$ nuclear reaction is an efficacious mutagen to mutate DNA which contains the stable isotope of ^{15}N with a specific isotope abundance varied from the natural abundance ratio of 0.364 % to the maximum ratio higher than 98%. The radiation effects of the $^{15}N(^{1}H, \alpha_{1}\gamma)^{12}C$ nuclear reaction may also give rise to genomic damage of malignant tumor. The present results elucidate a possibility that disparity in the isotope abundance ratio of ^{15}N between normal cells and cancerous tumor cells leads to a new proton therapy to target the genomes of malignant tumor.

References

[1] B. Pilzecker, et al., Nucleic Acids Research 47 (2019) 7163.
[2] I. Suzuki, et al., UTTAC Annual Report 2021, UTTAC-91 (2022) 50.
[3] L. M. Korsholm, et al., Nucleic Acids Research 48 (2020) 9449.
[4] I. Suzuki, et al., UTTAC Annual Report 2020, UTTAC-90 (2021) 44.
[5] Y. Iwata et al., European Advanced Materials Congress (EAMC2019), Stockholm during 11–14 August (2019), Invited paper.

6.

TECHNICAL REPORT

Technology exchange between KEK and University of Tsukuba. The engineers of KEK are visiting the tandem accelerator facility of UTTAC.

6.1 Development of the terminal vacuum gauge system

Y. Yamato, T. Yoshida, S. Ishii

NEC's 6MV tandem accelerator (18SDH-2) is originally equipped with a thermocouple to monitor the internal low vacuum of the high-voltage terminal. However, monitor of high vacuum is needed not only to accelerate polarized beams, but also to confirm the fully closed state of the needle valve of the gas stripper. Hence, a new vacuum gauge system has been developed and installed in the high-voltage terminal of the 6MV tandem accelerator.

Fig. 1. Offline tests of the vacuum gauge.

We started with several offline tests using a test chamber which reproduces the vacuum and high pressure environment of the accelerator tank, shown in Fig. 1. A Mirapro Cold Cathode Tough Gauge (CCTG200C) attached to the chamber withstood mechanically at least 5 atmospheres outside the vacuum gauge. To operate this gauge, a new nipple with feedthroughs into the accelerator tank was designed and fabricated. The feedthroughs consist of BNC hermetically sealed connectors for power supply and LAN (RJ45) hermetically sealed connectors for communication. As a result, the vacuum gauge operated without problems in the environment of 6×10^{-6} Torr inside and 5.5 kg/cm^2 of N_2 gas outside the vacuum gauge.

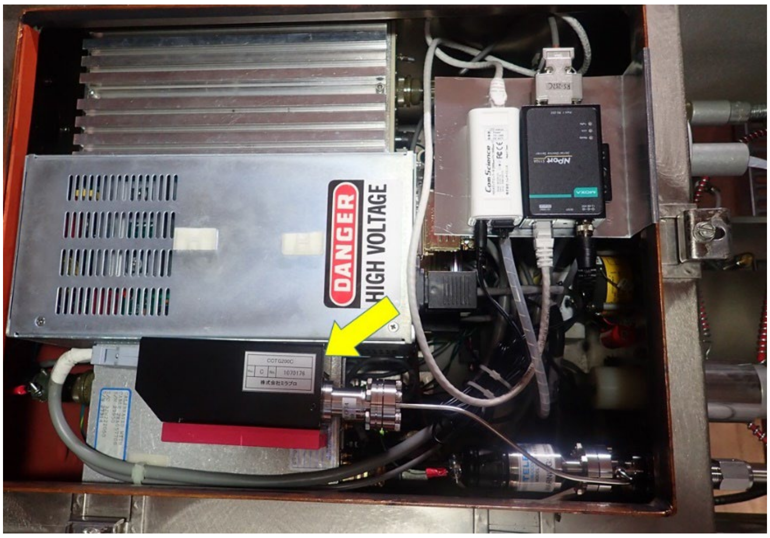

Fig. 2. Inside the shielded terminal box with the connected new vacuum gauge (indicated by the yellow arrow).

After the successful offline tests, the device was attached to the high-voltage terminal of the 18SDH-2, shown in Fig. 2. The communication of CCTG200C by RS-232C can be converted to LAN using a serial device server (NPort). To use LAN at the high-voltage terminal, two plastic optical fibers (POF) were stretched from the high-voltage terminal to the grounded accelerator tank along the beam direction. The fibers were fixed to all columns with newly designed original fixtures, see Fig. 3.

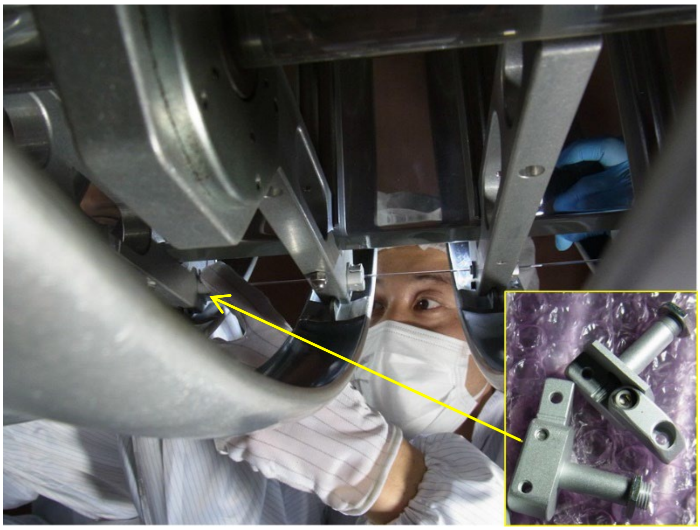

Fig. 3. Work of fixing POF to the column, using the newly designed fixtures.

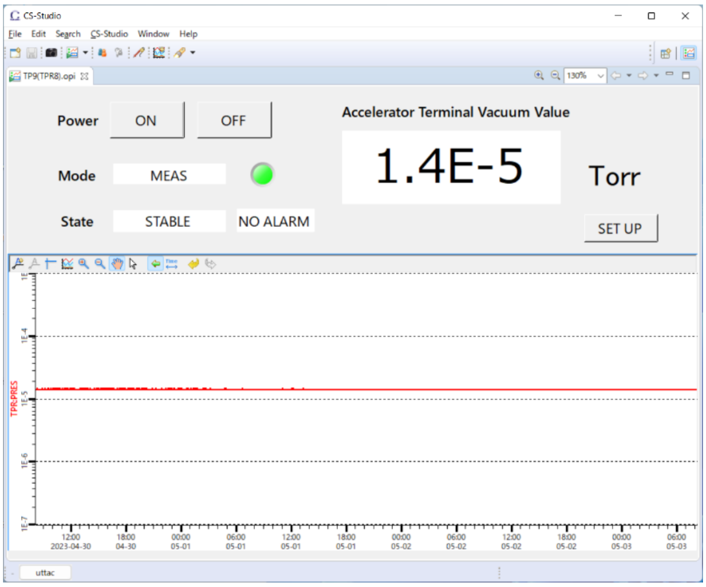

Accelerator Terminal Vacuum Value

1.4E-5 Torr

Mode MEAS

State STABLE NO ALARM

Fig. 4. Real-time display for the terminal vacuum gauge.

A software was developed to remotely monitor CCTG200C-NPort communications using Experimental Physics and Industrial Control System (EPICS) Asyn and StreamDevice. The user interface employs Control System Studio (CSS) for real-time display and trend graphs, shown in Fig. 4.

It should be noted that troubles occurred with the new terminal vacuum gauge system during conditioning of the accelerator. When the tank sparked, CCTG200C, NPort, LAN-POF converter, and other devices froze frequently. To reset the system, it was necessary to turn off the terminal generator (RS), wait a few tens of seconds, and turn it back on, or unplug the power supply to the LAN-POF converter outside the tank.

Table 1 shows the terminal vacuum gauge data when Ar stripper gas was supplied. Since CCTG200C is not applicable above 4×10^{-3} Torr, it is better to use the original thermocouple for further supply of the Ar gas. Also, with the new terminal vacuum gauge, it was found for the first time that the terminal vacuum improves from 1×10^{-5} to 4×10^{-7} Torr when the turbomolecular pump at the terminal is stopped.

Table 1. Ar gas valve rotation and terminal vacuum value data.

Terminal (Torr)	GS PR (mpsi)	GS DC (Trn)	IGC 02-2 PR(Torr)	IGC 03-1 PR(Torr)
9.6E-05	7.0	4.0	8.7E-08	5.9E-08
1.4E-04	7.1	4.5	8.6E-08	5.9E-08
2.8E-04	7.2	4.8	8.6E-08	6.0E-08
7.7E-04	7.6	5.0	9.4E-08	6.5E-08
1.3E-03	8.0	5.1	1.0E-07	7.1E-08
1.8E-03	8.5	5.2	1.1E-07	7.7E-08
4.1E-03	8.9	5.3	1.2E-07	8.6E-08
4.9E-03	9.9	5.4	1.3E-07	9.6E-08
5.6E-03	13.6	5.5	1.5E-07	1.1E-07

6.2 VR-techniques for electrostatic tandem accelerator

T. Yoshida, Y. Yamato, K. Sasa, K. Hirota[1], M. Furusaka[1]

University of Tsukuba Tandem Accelerator Complex (UTTAC) owns the 6MV Pelletron tandem accelerator and the 1MV Tandetron accelerator, which are used in research and educational activities. The purpose of developing Virtual Reality (VR) exhibition is to use it for undergraduate student's experimental practice in accelerator science, high school student's facility tours, and education for human resource development. The present work was supported by International and Inter-institution Network for Accelerator Science to Next Generation (IINAS-NX).

The tank of the 6MV Pelletron tandem accelerator is always filled with insulating SF_6 gas at 5 atmospheres to prevent electrical discharge and, for this reason, the tank is opened only once a year for regular maintenance. Almost all visitors cannot have a chance to look inside the accelerator tank during the tour, but instead, they can see the inside using VR goggles. Using VR goggles to see 360-degree photo inside the accelerator tank, visitors can look around inside the tank as if they were actually in the tank. Through such experience, we hope to get undergraduate and high school students interested in accelerators. As an example of actual use of VR, an educational accelerator KETA at KEK is presented in VR which is used for open to the public [1]. The Hiroshima Synchrotron Radiation Center (HiSOR) has a web page showing the facilities in VR [2]. We hope to release many types of accelerator VR for public, cooperating with other facilities.

For the development environment for VR, we have chosen Unity, the game engine developed and provided from Unity Technologies [3]. Unity allows to build data for many platforms such as Android, iOS, Windows, and webGL. We made the VR data by Unity and, after these data were built for the Andoroid format, the data were sent to the Oculus Quest 2 of the VR goggles to see the accelerators in the VR.

The VR created was divided into two parts: the 6MV Pelletron tandem accelerator and the 1MV Tandetron accelerator. The former VR was set up so that a total of five contents could be switched by pressing a button on the controller attached to the VR goggles: two 360-degree photos of the inside of the tank, two overhead shots of the entire accelerator room, and the Computer Graphics (CG) of the 6MV Pelletron tandem accelerator. The latter VR was set up for a total of two contents; overhead shot of the entire accelerator room, and the CG of the 1MV Tandetron accelerator. It can be switched by pressing a different button on the controller. For the 1MV Tandetron accelerator, only the photo of the accelerator room can be viewed since the tank normally remains closed.

Fig. 1. VR view inside the tank of the 6MV Pelletron tandem accelerator.

The front view inside the tank of the 6MV Pelletron tandem accelerator is shown in Fig. 1. Using VR

---

[1] High Energy Accelerator Research Organization (KEK)

goggles, one can see the 360-degree view inside the accelerator tank, including the wall behind and the ladder at the feet. By tilting the controller stick, one can get closer to the photo and observe the pellet chain that carries the electric charge and the accelerator tube at the center of the tank.

Not only the 360-degree photo, but also the CG of the accelerator was created by importing CAD data (Figs. 2 and 3). The position of the view changes as one walks around, allowing to look into the inside of the accelerator. As shown in Fig. 4, the inside of the accelerator tube can also be viewed to follow the passing beam. The beam is shown schematically by a spherical object that pops out sequentially.

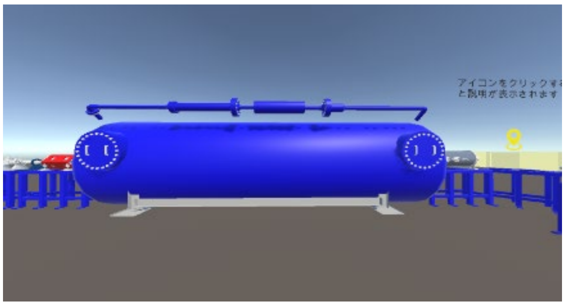

Fig. 2. CG image of the 6MV Pelletron tandem accelerator.

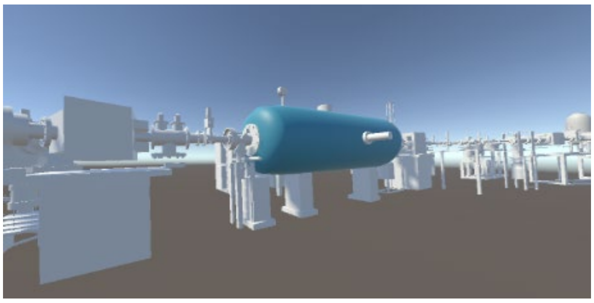

Fig. 3. CG image of the 1MV Tandetron accelerator.

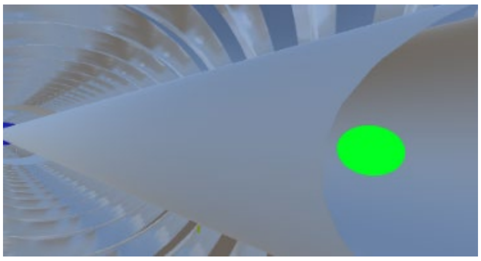

Fig. 4. Image of the beam passing through the accelerator tube.

We have five VR goggles now for five people at the same time. In FY2022, the VR goggles were used by a total of 258 visitors (217 high school students, 25 university students, and 16 participants in the technical workshop). In Fig. 5, the visitors with the VR goggles in front of the accelerator tank are looking at the VR view with amazement. However, it is difficult for them to communicate with the guide who explains the VR view, since each of them is looking at a different view at the same time. In the future, we need to develop such a function that can display explanations about the tandem accelerator, thereby the visitors understand the mechanism of the acceleration of ion beams. Furthermore, the VR view with explanations will be used as a teaching material for students. To compensate the limited number of VR goggles, we are considering to introduce Augmented Reality (AR) technology using smartphone.

Fig. 5. Visitors with the VR goggles in front of the accelerator tank.

References

[1] M. Furusaka et al., PASJ2022 FRP030. 2022, 984-988.

[2] HiSOR VR (Hiroshima Synchrotron Radiation Center VR) https://www.kasokuki-dx.jp/vr/

[3] Unity Technologies https://unity.com/

7.

LIST OF PUBLICATIONS AND PRESENTATIONS

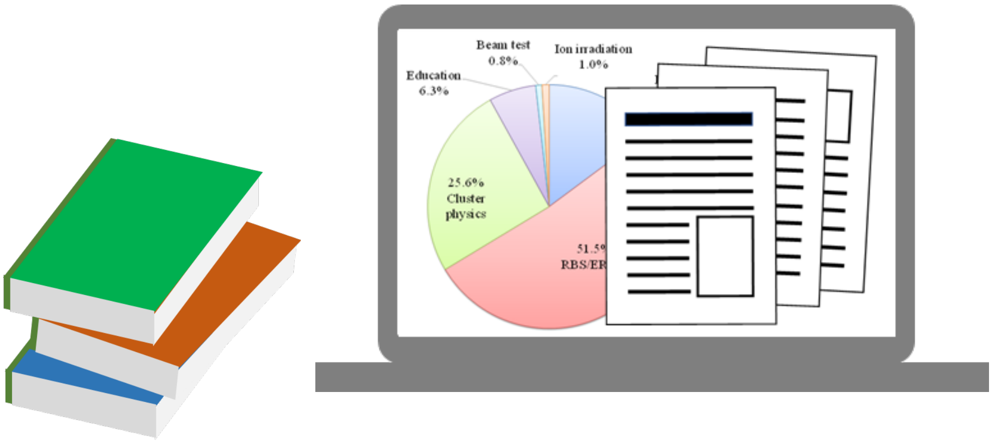

7.1 Peer-reviewed and proceedings papers

ACCELERATOR AND RERATED FACILITIES

1. T. Moriguchi, A. Ozawa, Y. Yamato, M. Hayashi, R. Kagesawa, N. Kaname, M. Mukai, K. Tomita, A. Yano, "Status of Lamb-shift polarized ion source at 6MV tandem accelerator in UTTAC and its application to nuclear physics", Proceedings of the 24th International Spin Symposium (SPIN2021), JPS Conf. Proc. 37 (2022) 021201. [DOI: 10.7566/JPSCP.37.021201]

NUCLEAR AND ATOMIC PHYSICS

1. Y. Ishibashi, A. Gladkov, Y. Ichikawa, A. Takamine, H. Nishibata, T. Sato, H. Yamazaki, T. Abe, J. M. Daugas, T. Egami, T. Fujita, G. Georgiev, K. Imamura, T. Kawaguchi, W. Kobayashi, Y. Nakamura, A. Ozawa, M. Sanjo, N. Shimizu, D. Tominaga, L. C. Tao, K. Asahi, H. Ueno, "Nuclear magnetic moment of the neutron-rich nucleus ^{21}O", Phys. Rev. C 107 (2023) 024306. [DOI: 10.1103/PhysRevC.107.024306]

2. M. Tanaka, M. Takechi, A. Homma, A. Prochazka, M. Fukuda, D. Nishimura, T. Suzuki, T. Moriguchi, D. S. Ahn, A. Aimaganbetov, M. Amano, H. Arakawa, S. Bagchi, K.-H. Behr, N. Burtebayev, K. Chikaato, H. Du, T. Fujii, N. Fukuda, H. Geissel, T. Hori, S. Hoshino, R. Igosawa, A. Ikeda, N. Inabe, K. Inomata, K. Itahashi, T. Izumikawa, D. Kamioka, N. Kanda, I. Kato, I. Kenzhina, Z. Korkulu, Y. Kuk, K. Kusaka, K. Matsuta, M. Mihara, E. Miyata, D. Nagae, S. Nakamura, M. Nassurlla, K. Nishimuro, K. Nishizuka, K. Ohnishi, M. Ohtake, T. Ohtsubo, S. Omika, H. J. Ong, A. Ozawa, H. Sakurai, Scheidenberger, Y. Shimizu, T. Sugihara, T. Sumikama, H. Suzuki, S. Suzuki, H. Takeda, Y. Tanaka, Y. K. Tanaka, I. Tanihata, T. Wada, K. Wakayama, S. Yagi, T. Yamaguchi, R. Yanagihara, Y. Yanagisawa, K. Yoshida, T. K. Zholdybayev, "Charge-changing cross sections for $^{42\text{-}51}$Ca and effect of charged-particle evaporation induced by neutron-removal reactions", Phys. Rev. C 106 (2022) 014617. [DOI: 10.1103/PhysRevC.106.014617]

3. H. F. Li, S. Naimi, T. M. Sprouse, M. R. Mumpower, Y. Abe, Y. Yamaguchi, D. Nagae, F. Suzaki, M. Wakasugi, H. Arakawa, W. B. Dou, D. Hamakawa, S. Hosoi, Y. Inada, D. Kajiki, T. Kobayashi, M. Sakaue, Y. Yokoda, T. Yamaguchi, R. Kagesawa, D. Kamioka, T. Moriguchi, M. Mukai, A. Ozawa, S. Ota, N. Kitamura, S. Masuoka, S. Michimasa, H. Baba, N. Fukuda, Y. Shimizu, H. Suzuki, H. Takeda, D. S. Ahn, M. Wang, C. Y. Fu, Q. Wang, S. Suzuki, Z. Ge, Yu. A. Litvinov, G. Lorusso, P. M. Walker, Zs. Podolyak, T. Uesaka, "First application of mass measurements with the Rare-RI Ring reveals the solar r-process abundance trend at $A = 122$ and $A = 123$", Phys. Rev. Lett. 128 (2022) 152701. [DOI: 10.1103/PhysRevLett.128.152701]

ACCELERATOR MASS SPECTROMETRY

1. H. Shen, G. Zhang, J. Tang, S. Shi, L. Wang, D. Chen, L. Qi, Y. Ouyang, X. Han, K. Wu, X. Sun, H. Yun, Y. Bao, M. He, K. Sasa, S. Jiang, "A single-stage accelerator mass spectrometer and its applications at Guangxi Normal University", Nucl. Instrum. Methods Phys. Res. B 532 (2022) 68. [DOI: 10.1016/j.nimb.2022.10.004]

2. H. Shen, S. Shi, J. Tang, M. Qi, S. Wei, K. Sasa, M. Liu, L. Wang, G. Zhang, L. Qi, D. Chen, S. Gong, G. Song, J. Dong, M. Wei, Y. He, "^{14}C-AMS technology and its applications to an oil field tracer experiment", Radiocarbon 64 (2022) 1159. [DOI: 10.1017/RDC.2022.28]

3. H. Shen, J. Tang, L. Wang, M. Qi, Z. Li, S. Wei, K. Sasa, S. Shi, G. Zhang, D. Chen, L. Qi, N. Wang, H. Zhou, M. He, Q. Zhao, Y. He, "New sample preparation line for radiocarbon measurements at the GXNU laboratory", Radiocarbon 64 (2022) 15011. [DOI:10.1017/RDC.2022.36]

4. K. Sasa, Y. Ochiai, Y. Tosaki, T. Matsunaka, T. Takahashi, M. Matsumura K. Sueki, "Chlorine-36 deposition at Tsukuba, Japan, after the Fukushima Daiichi Nuclear Power Plant accident", Nucl. Instrum. Methods Phys. Res. B 532 (2022) 73. [DOI: 10.1016/j.nimb.2022.10.003]

5. M. Kuwae, B. P. Finney, Z. Shi, A. Sakaguchi, N. Tsugeki, T. Omori, T. Agusa, Y. Suzuki, Y. Yokoyama, H. Hinata, Y. Hatada, J. Inoue, K. Matsuoka, M. Shimada, H. Takahara, S. Takahashi, D. Ueno, A. Amano, J. Tsutsumi, M. Yamamoto, K. Takemura, K. Yamada, K. Ikehara, T. Haraguchi, S. Tims, M. Froehlich, L. K. Fifield, T. Aze, K. Sasa, T. Takahashi, M. Matsumura, Y. Tani, P. R. Leavitt, H. Doi, T. Irino, K. Moriya, A. Hayashida, K. Hirose, H. Suzuki, Y. Saito, "Beppu Bay, Japan, as a candidate Global Boundaries Stratotype Section and Point for the Anthropocene series", The Anthropocene Review 10 (2023) 49. [DOI: 10.1177/20530196221135077]

6. J. Tang, H. Shen, L. Wang, G. Z. Hang, L. Qi, D. Chen, Z. Li, S. Shi, M. Qi, He Ouyang, X. Han, K. Wu, Y. Wang, B. Wu, Y. Xie, N. Wang, Y. He, K. Sasa, "A simple preparation system for Tritium and Radiocarbon at the GXNU laboratory", Nucl. Instrum. Methods Phys. Res. B 535 (2023) 261. [DOI: 10.1016/j.nimb.2022.11.026]

BEAM AND ISOTOPE APPLICATIONS

1. H. Kudo, M. Kurosawa, H. Naramoto, M. Sataka, S. Ishii, K. Sasa S. Tomita, "Determination of hydrogen concentration in solids by transmission ERDA under nuclear-elastically enhanced recoiling of H by 8 and 9 MeV He", J. Phys.: Condens. Matter 34 (2022) 435902. [DOI: 10.1088/1361-648X/ac8b4e]

2. H. Matsui and I. Yamaguchi, “Enhancement of self-field critical current density by several-tens-MeV ion irradiation in $YBa_2Cu_3O_7$ films prepared by fluorine-free metal-organic deposition”, Jpn. J. Appl. Phys. 61 (2022) 043001. [DOI: 10.35848/1347-4065/ac5265]

3. T. Kameda, A. Nagata, Y. Kimura, R. Imai, P. Shrestha, K. Kimura, A. Yasuda, H. Watanabe, “Space environment evaluation and low-earth-orbit demonstration of a communication component with a commercial transceiver integrated circuit”, Aerospace 9 (2022) 280. [DOI: 10.3390/aerospace9060280]

4. N. Oishi, Y. Murao, N. Nitta, H. Tsuchida, S. Tomita, K. Sasa, K. Hirata, H. Shibata, Y. Hirano, K. Yamada, A. Chiba, Y. Saitoh, K. Narumi, Y. Hoshino, “Morphological changes of nanostructures on silicon induced by C_{60}-ion irradiation”, J. Vac. Sci. Technol. A 40 (2022) 063103. [DOI: 10.1116/6.0002073]

5. R. Murase, H. Tsuchida, S. Nakagawa, S. Tomita, A. Chiba, K. Nakajima, T. Majima, M. Saito, “Incident Energy Dependence of the Molecular Orientation Effect of MeV C_2^+ Projectiles in Secondary-Ion Emission Processes”, J. Phys. Soc. Jpn. 91 (2022) 024302. [DOI: 10.7566/JPSJ.91.024302]

6. T. Hamada, S. Takase, A. Tanaka, K. Okada, S. Mineoi, A. Uedono, J. Ohshita, “Double-decker silsesquioxane-grafted polysilsesquioxane hybrid films as thermal insulation materials”, ACS Appl. Polym. Mat. 5 (2022) 743. [DOI: 10.1021/acsapm.2c01743]

7. T. Umeda, K. Watanabe, H. Hara, H. Sumiya, S. Onoda, A. Uedono, I. Chuprina, P. Siyushev, F. Jelezko, J. Wrachtrup, J. Isoya, “Negatively charged boron vacancy center in diamond”, Phys. Rev. B 105 (2022) 165201. [DOI: 10.1103/PhysRevB.105.165201]

8. A. Uedono, N. Takahashi, R. Hasunuma, Y. Harashima, Y. Shigeta, Z. Ni, H. Matsui, A. Notake, A. Kubo, T. Moriya, K. Michishio, N. Oshima, S. Ishibashi, “Vacancy-type defects in $TiN/ZrO_2/TiN$ capacitors probed by monoenergetic positron beams”, Thin Solid Films 762 (2022) 139557. [DOI: 10.1016/j.tsf.2022.139557]

9. S. Takase, T. Hamada, K. Okada, S. Mineoi, A. Uedono, J. Ohshita, “Organic-inorganic hybrid thermal insulation materials prepared via hydrosilylation of polysilsesquioxane having hydrosilyl groups and triallylisocyanurate”, ACS Appl. Poly. Mat. 4 (2022) 372673. [DOI: 10.1021/acsapm.2c00241]

10. T. Narita, A. Uedono, T. Kachi, “Effects of hydrogen incorporation on Mg diffusion in GaN-doped with Mg ions via ultra-high-pressure annealing”, Phys. Status Solidi B 259 (2022) 2200235.

[DOI: 10.1002/pssb.202200235]

11. L. Y. Li, K. Shima, M. Yamanaka, T. Egawa, T. Takeuchi, M. Miyoshi, S. Ishibashi, A. Uedono, S. F. Chichibu, “Room-temperature nonradiative recombination lifetimes in c-plane $Al_{1-x}In_xN$ epilayers nearly and modestly lattice-matched to GaN ($0.11 \leq x \leq 0.21$)”, J. Appl. Phys. 132 (2022) 163102. [DOI: 10.1063/5.0106540]

12. E. Kano, K. Kataoka, J. Uzuhashi, K. Chokawa, H. Sakurai, A. Uedono, T. Narita, K. Sierakowski, M. Bockowski, R. Otsuki, K. Kobayashi, Y. Itoh, M. Nagao, T. Ohkubo, K. Hono, J. Suda, T. Kachi, N. Ikarashi, “Atomic resolution analysis of extended defects and Mg agglomeration in Mg-ion-implanted GaN and their impacts on acceptor formation”, J. Appl. Phys. 132 (2022) 065703. [DOI: 10.1063/5.0097866]

13. N. Shoji, K. Sasaki, A. Uedono, Y. Taniguchi, K. Hayashi, N. Matsubara, T. Kobayashi, T. Yamashita, “Effect of conversion on epoxy resin properties: Combined molecular dynamics simulation and experimental study”, Polymer 254 (2022) 125041. [DOI: 10.1016/j.polymer.2022.125041]

14. Z. H. Li, T. T. Sasaki, A. Uedono, K. Hono, “Role of Zn on the rapid age-hardening in Mg-Ca-Zn alloys”, Scr. Mater. 216 (2022) 114735. [DOI: 10.1016/j.scriptamat.2022.114735]

15. A. Uedono, H. Sakurai, J. Uzuhashi, T. Narita, K. Sierakowski, S. Ishibashi, S. F. Chichibu, M. Bockowski, J. Suda, T. Ohkubo, N. Ikarashi, K. Hono, T. Kachi, “Effect of ultra-high-pressure annealing on defect reactions in ion-implanted GaN studied by positron annihilation”, Phys. Stat. Sol. B 259 (2022) 2200183. [DOI: 10.1002/pssb.202200183]

16. S. F. Chichibu, H. Miyake, A. Uedono, “Impacts of Si-doping on vacancy complex formation and their influences on deep ultraviolet luminescence dynamics in $Al_xGa_{1-x}N$ films and multiple quantum wells grown by metalorganic vapor phase epitaxy”, Jpn. J. Appl. Phys. 61 (2022) 050501. [DOI: 10.35848/1347-4065/ac46b1]

17. T. Hamada, T. Goto, S. Takase, K. Okada, A. Uedono, J. Ohshita, “Structure-thermal property relationships of polysilsesquioxanes for thermal insulation materials”, Appl. Polym. Mat. 4 (2022) 2851. [DOI: 10.1021/acsapm.1c01812]

18. H. Okumura, Y. Watanabe, T. Shibata, K. Yoshizawa, A. Uedono, H. Tokunaga, S. Koseki, T. Arimura, S. Sihkonen, T. Palacios, “Impurity diffusion in ion implanted AlN layers on sapphire substrates by thermal annealing”, Jpn. J. Appl. Phys. 61 (2022) 026501. [DOI: 10.35848/1347-4065/ac47aa]

19. C. Kodaka, M. Kishimoto, E. Kita, H. Yanagihara, “Crystal structure and magnetic properties of hexagonal FeCo nitrides prepared using ammonia gas nitrification”, IEEE Magn. Lett. 14 (2023) 2500105. [DOI: 10.1109/LMAG.2023.3262452]

7.2 Reviews and books

1. A. Ozawa, “Matter Radii and Density Distributions”, In: Handbook of Nuclear Physics, Springer, Singapore, 2022. [DOI: 10.1007/978-981-15-8818-1 40-1]

2. 矢野朝陽, “反応断面積測定のための固体水素・重水素標的の開発”, 原子核研究 67 (2023) 15.

7.3 Poster and oral presentations

1. 矢野朝陽，小沢 顕，森口哲朗，福田光順，福留美樹，高山 元，田口 諒，渡辺 薫，田中聖臣，鈴木 健，山口貴之，大久保研吾，古泉 紫，佐々木健太，西村太樹，網谷芽衣，富山琢史，中村佑生，平山 瞳，福嶋知隼，大坪 隆，野口法秀，高津和哉，小林侑希哉，進藤楠月，田澤有紀，泉川卓司，佐藤眞二，福田茂一，北川敦志，“He ガスセルを用いた固体水素標的の厚さの均一化”，日本物理学会 2023 年春季大会，オンライン開催（2023 年 3 月 22-25 日).

2. 矢野朝陽，小沢 顕，森口哲朗，福田光順，三原基嗣，福留美樹，高山 元，木村容子，田口 諒，本多裕也，林 双葉，田中聖臣，鈴木 健，山口貴之，神田真矩，関 響咲，大久保研吾，古泉 紫，佐々木健太，西村太樹，高橋弘幸，菅原奏来，宇根千晶，大坪 隆，野口法秀，泉川卓司，佐藤眞二，福田茂一，北川敦志，“不安定核の反応断面積測定に向けた固体重水素標的の開発”，第 2 回日本量子医科学会学術大会，つくば国際会議場（2022 年 12 月 9-10 日).

3. 森口哲朗，“非対称核物質の理解に向けた不安定核の反応断面積測定”，筑波大学宇宙史研究センター2022 年度第 2 回構成員会議・成果報告&交流会，筑波大学（2022 年 11 月 28 日).
(招待講演)

4. 森口哲朗，“固体水素，固体重水素標的を用いた反応断面積測定”，反応断面積研究の新しい展望 WS，理化学研究所和光キャンパス（2022 年 11 月 9-10 日).（招待講演）

5. T. Moriguchi, “Development solid Hydrogen/Deuterium Target for reaction cross section measurements”, Online seminar invited by Beihang University (Oct. 13, 2022). (Invited Talk)

6. 森口哲朗，“RI ビーム飛行時間検出器の開発 –理研稀少RI リングのための検出器– ”，2021 年度 HIMAC 共同利用研究成果発表会，オンライン開催（2022 年 5 月 30 日-6 月 1 日).

7. 松村 宏，吉田 剛，豊田晃弘，中村 一，桝本和義，三浦太一，別所光太郎，松村万寿美，森口哲朗，笹 公和，“ガンマカメラ GeGI5 による加速器放射化の可視化の可能性の検討”，第 4 回日本保健物理学会・日本放射線安全管理学会合同大会，九州大学伊都キャンパス（ 2022 年 11 月 24-26 日).

8. 吉田 剛，松村 宏，豊田晃弘，中村 一，桝本和義，別所光太郎，三浦太一，松村万寿美，森口哲朗，笹 公和，“ガンマカメラ GeGI5 による加速器放射化の可視化実験”，第 4 回日本保健物理学会・日本放射線安全管理学会合同大会，九州大学伊都キャンパス（2022 年 11 月 24-26 日）.

9. 吉田 剛，松村 宏，松村万寿美，豊田晃弘，中村 一，桝本和義，三浦太一，笹 公和，森口哲朗，“可搬型 γ 線イメージング装置 GeGI5 による筑波大タンデムの加速器放射化イメージング -加速器の放射化イメージングへの挑戦- ”，第 34 回タンデム加速器及びその周辺技術の研究会，日本原子力研究開発機構 原子力科学研究所，オンライン開催（2022 年 7 月 21-22 日）.

10. 笹 公和，“筑波大学タンデム加速器施設の東日本大震災からの復旧，復興，その後の発展”，日本原子力学会 2022 年秋の大会，加速器・ビーム科学部会企画セッション，茨城大学日立キャンパス（2022 年 9 月 8 日）.（招待講演）

11. 笹 公和，“加速器質量分析法による宇宙線生成核種の検出と地球化学への応用”，日本地球化学会第 69 回年会，高知大学（2022 年 9 月 7 日）.（招待講演）

12. 笹 公和，“加速器質量分析法における環境中の難測定核種の検出技術に関する進展”，日本放射化学会第 66 回討論会，東京大学（ 2022 年 9 月 15 日）.（招待講演）

13. 笹 公和，石井 聰，高橋 努，大和良広，田島義一，松村万寿美，森口哲朗，上殿明良，“筑波大学タンデム加速器施設の現状報告”，日本加速器学会第 19 回年会，オンライン開催（ 2022 年 10 月 18-21 日）.

14. 笹 公和，椎根大輔，高橋 努，松村万寿美，坂口 綾，“6MV タンデム加速器を用いた長半減期放射性セシウム 135 の加速器質量分析法の開発”，日本加速器学会第 19 回年会，オンライン開催（2022 年 10 月 18-21 日）.

15. 笹 公和，石井 聰，高橋 努，大和良広，田島義一，松村万寿美，森口哲朗，上殿明良，“筑波大学タンデム加速器施設 UTTAC の現状”，第 34 回タンデム加速器及びその周辺技術の研究会，日本原子力研究開発機構 原子力科学研究所，オンライン開催（2022 年 7 月 21-22 日）.

16. 松中哲也，長尾誠也，井上睦夫，田中さき，熊本雄一郎，谷内由貴子，葛西広海，森田貴己，三木志津帆，高橋 努，松村万寿美，末木啓介，笹 公和，“北極海とオホーツク海におけるヨウ素 129 の水平分布解析”，日本海洋学会 2022 年度秋季大会，名古屋大学東山キャンパス，ハイブリッド開催（2022 年 9 月 3-7 日及び 12 日）.

17. 松中哲也，落合伸也，松村万寿美，高橋 努，末木啓介，笹 公和，“能登半島における 1950 年以降の I-129 と Cs-137 の沈着量変動”，日本放射化学会第 66 回討論会，東京大学

(2022 年 9 月 15 日～17 日).

18. 冨田成夫，平賀真瑠古，畑田颯太，椎名陽子，高橋　努，石井　聡，笹　公和，“高速分子イオン入射によるコンボイ電子生成におけるイオン種依存性”，第 23 回「イオンビームによる表面・界面の解析と改質」特別研究会，若狭湾エネルギー研究センター（2022 年 12 月 2-3 日).

19. 冨田成夫，平賀真瑠古，畑田颯太，椎名陽子，高橋　努，石井　聡，笹　公和，“コンボイ電子収量におけるクラスター効果の入射粒子依存性 III”，日本物理学会　2002 年秋季大会，
東京工業大学大岡山キャンパス（2022 年 9 月 12-15 日).

20. 冨田成夫，平賀真瑠古，畑田颯太，椎名陽子，高橋　努，石井　聡，笹　公和，“コンボイ電子収量におけるクラスター効果の消失膜厚”，日本物理学会 2023 年春季大会，オンライン開催
(2023 年 3 月 22-25 日).

21. 松村万寿美，笹　公和，松中哲也，高橋　努，坂口　綾，末木啓介，“加速器質量分析に携わる実験室のヨウ素 129 降下量調査（2022 年夏季)”，第 23 回 AMS シンポジウム，山形大学
(2022 年 12 月 1-2 日).

22. 笹　公和，高橋　努，松村万寿美，松中哲也，坂口　綾，末木啓介，“筑波大学 6 MV タンデム加速器質量分析装置における多核種 AMS と応用研究の現状”，第 23 回 AMS シンポジウム，山形大学
(2022 年 12 月 1-2 日).

23. 三宅芙沙，箱崎真隆，R. Hantemirov，早川尚志，S. Helama，堀内一穂，A. J. T. Jul，木村勝彦，前原裕之，宮原ひろ子，森谷　透，M. Oinonen，I. P. Panyushkina，笹　公和，武山美麗，門叶冬樹，“過去 1 万年間の極端太陽高エネルギー粒子現象の調査”，第 23 回 AMS シンポジウム，
山形大学（2022 年 12 月 1-2 日).

24. 冨田成夫，平賀真瑠古，畑田颯太，尾関海太，椎名陽子，高橋　努，石井　聡，笹　公和，
“コンボイ電子収量におけるクラスター効果の消失膜厚”，日本物理学会　2023 年春季大会，オンライン開催（2023 年 3 月 22-25 日).

25. 笹　公和，椎根大輔，高橋　努，松村万寿美，坂口　綾，“加速器質量分析法による長半減期放射性セシウム 135 の高感度検出試験”，2023 年第 70 回応用物理学会春季学術講演会，上智大学
(2023 年 3 月 15-18 日).

26. 松井浩明，山口　巖，“イオン照射による Y 系高温超伝導膜の自己磁場中臨界電流密度制御”，応用物理学会秋季学術講演会，東北大学（2022 年 9 月 19-23 日).

27. C. Kodaka, M. Kishimoto, E. Kita, H. Yanagihara, “Crystal structure and magnetic properties of FeCo

nitrides prepared by ammonia gas nitrification", The 11th International Conference on Fine Particles Magnetism (ICFPM 2022), Yokohama, Japan (Oct. 16-21, 2022).

28. E. Kita, R. Onodera, M. Kishimoto, H. Yanagihara, "Magnetic relaxation of superparamagnetic Fe oxide particles studied with Mössbauer spectroscopy", The 11th International Conference on Fine Particles Magnetism (ICFPM 2022), Yokohama, Japan (Oct. 16-21, 2022).

7.4 UTTAC seminars

2023.1.10	Measurement of azimuthal anisotropy of jets and electrons from heavy quarks in Pb-Pb collisions at $\sqrt{s_{NN}}$ = 5.02 TeV with LHC-ALICE, *Ryotaro Nagata* (*University of Tsukuba*)
2023.1.10	Particle number fluctuations of protons, kaons and pions in $\sqrt{s_{NN}}$ = 19.6 GeV Au+Au collisions at RHIC-STAR experiment, *Kazuki Iwanaga* (*University of Tsukuba*)
2023.1.10	Measurements of the first to third order azimuthal anisotropies from the Beam Energy Scan in Au+Au collisions at RHIC-STAR experiment, *Shun Oike* (*University of Tsukuba*)
2023.1.10	Developments of solid hydrogen and solid deuterium targets for reaction cross section measurements of unstable nuclei, *Asahi Yano* (*University of Tsukuba*)

8.

THESES

(*From a free-use drawing on web*)

Doctor thesis

Tianjing Yang	Study on strain improvement of *Aurantiochytrium* by genetic engineering and random mutagenesis

Master theses

Asahi Yano	Developments of solid hydrogen and solid deuterium targets for reaction cross section measurements of unstable nuclei（不安定核の反応断面積測定に用いる固体水素標的と固体重水素標的の開発）
Souta Hatada	Development of radiation measurement system using FPGA（FPGA を用いた放射線計測システムの開発）
Shingo Oshida	Characterization of vacancy-type defects in NiAl using positron annihilation spectroscopy（陽電子消滅法を用いた NiAl の空孔型欠陥評価）
Naomichi Takahashi	Characterization of vacancy-type defects in a TiN/ZrO_2/TiN capacitor using positron annihilation spectroscopy（陽電子消滅法を用いた TiN/ZrO_2/TiN キャパシタの空孔型欠陥の評価）
Saki Tanaka (Kanazawa University)	Variation factor of polycyclic aromatic hydrocarbons in surface seawater of the Sea of Japan and Arctic Ocean（日本海および北極海表層における多環芳香族炭化水素類の変動要因解析）

Undergraduate theses

Uta Ozeki	Calibration of 1MV Tandetron generating voltage meter with energy measurement of covoy electrons（コンボイ電子を用いた 1MV タンデトロン加速器の GVM 較正）
Koudai Tanabe	Trajectory calculation for transport of charged particles by a 90-degree magnet（90度マグネットによる荷電粒子輸送軌道の計算）
Kazuki Yamamoto	Hydrogen analysis of a neutron-reflecting material using ERDA（ERDA による中性子反射材料の水素分析）
Kento Sato (Hirosaki University)	Variation of nuclear test produced ^{36}Cl in the H15 ice core at the East Antarctic coastal region（東南極沿岸域 H15 アイスコアに刻まれた核実験起源の ^{36}Cl 変動）

9.

LIST OF PERSONNEL

Three students are watching hydrogen signals in the T-ERDA experiment using the 6MV tandem accelerator.

—–– *Report 4.4*

Tandem Accelerator Complex

A. Uedono	Director, Professor
K. Sasa	Associate Professor
D. Sekiba	Lecturer
T. Moriguchi	Assistant Professor
S. Ishii	Mechanical Engineer
T. Takahashi	Electrical Engineer
Y. Yamato	Electrical Engineer
T. Yoshida	Electrical Engineer
M. Matsumura	Technical Staff
S. Kuramochi	Administrative Staff
N. Shimada	Administrative Staff
H. Muromachi	Administrative Staff
M. Watanabe	Administrative Staff

Research Members[1]

Department of Physics, Institute of Pure and Applied Sciences

A. Ozawa   T. Moriguchi   K. Sasa
T. Yamaguchi (Saitama University [Cross appointment])

Department of Applied Physics, Institute of Pure and Applied Sciences

E. Kita   D. Sekiba   S. Sharmin   S. Tomita
A. Uedono   H. Yanagihara   H. Tanimoto

Department of Chemistry, Institute of Pure and Applied Sciences

K. Sueki   A. Sakaguchi   S. Yamasaki

Department of Geosciences, Institute of Life and Environmental Sciences

M. Kurosawa

Department of Biology, Institute of Life and Environmental Sciences

I. Suzuki

Department of Intelligent Interaction Technologies, Institute of Systems and Information Engineering

T. Kameda

---

[1] The “research members” include the authors and coauthors within 5 years back from this fiscal year, as well as the members of research projects running at UTTAC.

Staff of Open Advanced Facilities Initiative

H. Kudo
H. Naramoto
M. Sataka
K. Awazu (National Institute of Advanced Industrial Science and Technology [AIST])
S. Aoki (Comprehensive Research Organization for Science and Society [CROSS])

Graduate students

Graduate School of Science and Technology

T. Amagai
N. Kishi
T. Yang
Z. Shi

A. Yano
M. Hiraga
N. Takahashi
T. Kanazawa
S. Hatada
S. Kubo
R. Hioki
C. Kodaka
T. Okamoto
T. Nakamura
K. Torii
S. Jung
Y. Yu
S. Oshida
K. Honma

Undergraduates

R. Takatsuki
U. Ozeki
Y. Abe
R. Tanaka
Y. Seki
T. Takahashi
Y. Kurihara
Y. Tanabe
H. Tanaka
H. Yoshikado
K. Yamamoto
R. Minami

External users and collaborators

Y. Iwata	National Institute of Advanced Industrial Science and Technology (AIST)
K. Tomita	National Institute of Advanced Industrial Science and Technology (AIST)
T. Ishizuka	National Institute of Advanced Industrial Science and Technology (AIST)
S. Shiki	National Institute of Advanced Industrial Science and Technology (AIST)
H. Matsui	National Institute of Advanced Industrial Science and Technology (AIST)
T. Matsunaka	Kanazawa University
M.Rodorigo	Kanazawa University
S. Tanaka	Kanazawa University
M. Ozawa	Kanazawa University
G. Yoshida	High Energy Accelerator Research Organization (KEK)
H. Matsumura	High Energy Accelerator Research Organization (KEK)
A. Toyoda	High Energy Accelerator Research Organization (KEK)
K. Mishima	High Energy Accelerator Research Organization (KEK)
S. Kawasaki	High Energy Accelerator Research Organization (KEK)
K. Horiuchi	Hirosaki University

K. Sato	Hirosaki University
R. Shimizu	Tokyo Institute of Technology
Y. Komatsu	Tokyo Institute of Technology
M. Honda	Japan Atomic Energy Agency (JAEA)
A. Ishiyama	Saitama University
Y. Nagami	Saitama University
K. Takiura	Saitama University
S. Otsuka	Saitama University
T. Suzuki	Saitama University